

Spatial Atomic Layer Deposition for Energy and Electronic Devices

Robert L.Z. Hoye^{1,*§}, David Muñoz-Rojas^{2,†§}, Zhuotong Sun³, Hayri Okcu^{2,4}, Hatameh Asgarimoghaddam^{5,6}, Judith L. MacManus-Driscoll³, and Kevin P. Musselman^{5,6,‡}

¹ Inorganic Chemistry Laboratory, Department of Chemistry, University of Oxford, South Parks Road, Oxford OX1 3QR, United Kingdom

² Université Grenoble Alpes, CNRS, Grenoble INP, Laboratory in Materials Science and Physical Engineering (LMGP), 38000 Grenoble, France

³ Department of Materials Science and Metallurgy, University of Cambridge, 27 Charles Babbage Road, Cambridge CB3 0FS, United Kingdom

⁴ Université Grenoble Alpes, Univ. Savoie Mont Blanc, CNRS, Grenoble INP, CROMA, F-38000 Grenoble, France

⁵ Waterloo Institute for Nanotechnology, University of Waterloo, Waterloo, Ontario N2L 3G1, Canada

⁶ Department of Mechanical and Mechatronics Engineering, University of Waterloo, Waterloo, Ontario N2L 3G1, Canada

(Received 28 August 2024; revised 17 January 2025; accepted 24 January 2025; published 19 February 2025)

Functional thin films play a critical role in efforts toward efficient devices for energy conversion and storage, as well as low-loss electronics. These films need to be manufactured at scale, cost-effectively, and with precision. Atmospheric pressure spatial atomic layer deposition (AP-SALD) has emerged as a promising technique for fulfilling these requirements. AP-SALD replicates the subnanometer control of thickness, uniformity, crystallinity, and conformality to the substrate featured in conventional atomic-layer-deposited films, but has the important advantage of depositing these films with growth rates that are orders of magnitude higher. This review discusses the opportunities and advantages that AP-SALD opens up in energy-conversion and storage devices, as well as low-loss electronics. In particular, the review features recent work on using AP-SALD-grown films for photovoltaics, light-emitting diodes, self-powered sensors, and photoelectrochemical cells and batteries, as well as in transparent conductive materials and the epitaxial growth of thin films. Perspectives on future unexplored opportunities for AP-SALD in energy and low-loss electronics are also discussed.

DOI: 10.1103/PRXEnergy.4.017002

I. INTRODUCTION

The urgent need for more efficient and cost-effective energy-conversion devices [such as photovoltaics (PVs), batteries, and photoelectrochemical cells] [1–7], as well as power electronics and computing [8], necessitates nanomanufacturing tools that can produce high-quality thin films with scale and high precision, and which can

be used to explore new materials to achieve improved performance. Atomic layer deposition (ALD) is one such technique and has become the most cost-effective option for producing thin films at the single-nanometer level in complex three-dimensional (3D) architectures [9,10]. Historically, a significant limiting factor of ALD is its inherently slow deposition [9,11–13]. Recently, this limitation has been addressed commercially by making large ALD batch reactors and ALD has now become the dominant approach for front-surface passivation in the silicon-PV industry [14,15]. At the same time, this approach leads to little flexibility in how manufacturing is carried out, since large batches of wafers need to be deposited onto simultaneously, and there are challenges with gas diffusion over long path lengths in large reactors, as well as precursor wastage due to fouling onto the inside of reactor walls. Spatial atomic layer deposition (SALD) could offer a route to overcome these challenges and has been gaining attention for the development of thin-film semiconductors for next-generation devices.

*Contact author: robert.hoye@chem.ox.ac.uk

†Contact author: david.munoz-rojas@grenoble-in.fr

‡Contact author: kevin.musselman@uwaterloo.ca

§These authors contributed equally to this work.

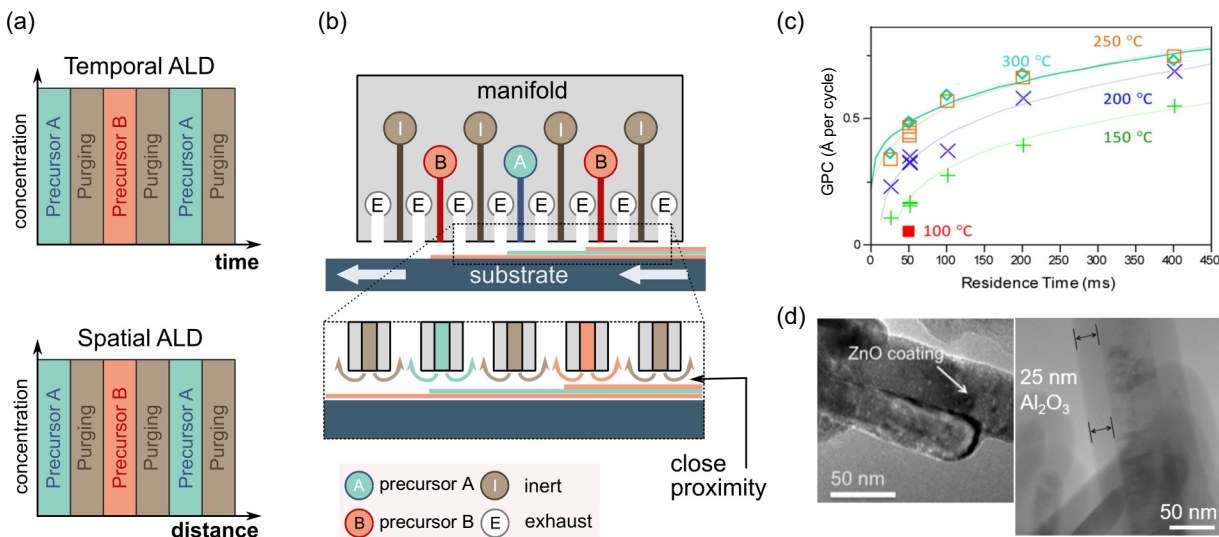


FIG. 1. An illustration of how spatial ALD works. (a) Cycling of the gas that the substrate is exposed to, alternating from precursor A to precursor B, which are separated with a purge step. In conventional ALD (or temporal ALD), precursors A and B are separated in time with a vacuum purge step to remove these precursors from the reaction chamber. By contrast, in spatial ALD, these two precursors are separated with an inert gas curtain (e.g., N₂ or Ar gas) [17]. (b) A schematic of a typical spatial ALD reactor operating based on the close proximity design, in which the gas manifold is brought close (tens to hundreds of microns) to the substrate. This can be achieved either by floating the manifold over the substrate (or vice versa) and is referred to as the gas-bearing design. Alternatively, the manifold could be mechanically maintained over the substrate and the manifold-substrate spacing is a controllable parameter [18]. (c) The growth per cycle as a function of the precursor exposure time, showing the saturation reached with ALD (in this case for Al₂O₃ growth at different deposition temperatures). Reproduced with permission from Ref. [19]. Copyright 2014, American Chemical Society. (d) An example of the conformal growth of Al₂O₃ (left) and ZnO (right) onto ZnO nanorods by atmospheric pressure spatial ALD. Reproduced with permission from Ref. [20]. Copyright 2016, Royal Society of Chemistry.

SALD carries out the same two half reactions as ALD, but separates the precursors in space (e.g., via a gas manifold with channels to guide the gas flows) rather than in time (as in ALD, which uses long purge steps between pulses of the two precursors) [16], as shown in Fig. 1(a). This allows films to be deposited orders of magnitude faster under atmospheric conditions, obviating the need for a vacuum chamber. For example, Al₂O₃ grown by ALD and SALD both have a growth per cycle (GPC) of approximately 0.1 nm per cycle, but the growth rate in SALD is higher, at 1.2 nm s⁻¹ compared to 0.05–0.3 nm s⁻¹ for conventional ALD (Table I) [21]. This opens up many possibilities, e.g., the growth of oxides onto thermally sensitive active-layer materials, such as lead-halide perovskites and organic semiconductors, by substantially reducing the deposition time at elevated temperatures. SALD is also highly customizable, with many different reactor-head designs possible for applications in depositing custom film patterns, wide reactor heads for roll-to-roll and sheet-to-sheet deposition, or even cylindrical reactors intended for coating tubular membranes [63]. A particularly common design is the “close-proximity” design, in which the reactor head and flat substrate are parallel to each other and brought close together (tens of micrometers), as shown in Fig. 1(b). Past reviews have

covered the history and development of SALD, along with the reactors that have been created, and some of the basic applications of using SALD to grow binary and multicomponent oxides (mostly based on ZnO and TiO₂) [9,11–13,64,65]. This review will discuss in detail the recent applications of SALD for energy devices and electronics, focusing on energy conversion (light to electricity and vice versa, as well as light to fuels), energy storage (batteries and fuel cells), transparent electrodes, and epitaxial films for low-loss electronics. The more complex materials recently developed (e.g., nonoxide materials and epitaxial films), the opportunities opened up by SALD over conventional ALD, as well as current challenges, will be discussed, along with future perspectives on the energy-materials challenges that SALD could address and how this may be carried out.

II. WORKING PRINCIPLES OF SPATIAL ALD

Detailed descriptions of how spatial ALD is carried out and the types of reactors used are covered elsewhere [9,11–13,64,65]. Here, a concise description will be given to provide context for the discussion later in this review. In both conventional (or temporal) and spatial ALD, the two precursors (A and B) need to be separated to ensure that

TABLE I. A comparison of the growth rate and growth per cycle of conventional temporal ALD (t-ALD) with spatial ALD (SALD) for common binary oxides. Representative deposition rates are selected. More detailed comparisons between different reactor types can be found in Ref. [21]. T_{dep} is the deposition temperature.

Material	Method	T_{dep} (°C)	Growth rate (nm s ⁻¹)	Growth rate (nm per cycle)	Sample size	Ref.
Al ₂ O ₃	t-ALD (Ultratech)	150–300	0.05–0.3	0.1	n.r.	[22]
Al ₂ O ₃	SALD (TNO)	200	1.2	0.12	3-cm-wide ring	[23]
Al ₂ O ₃	SALD (Levitech)	150–300	n.r.	0.12	15.6 × 15.6 cm ²	[24]
Al ₂ O ₃	SALD (SoLayTec)	200	0.5–1.2	n.r.	15.6 × 15.6 cm ²	[25]
Al ₂ O ₃	SALD	200	n.r.	0.17	n.r.	[26]
Al ₂ O ₃	PE SALD (O ₂ + N ₂ plasma)	160	n.r.	n.r.	n.r.	[27]
Al ₂ O ₃	SALD (Nexusbe; O ₃ oxidant)	200	n.r.	1.33	6 × 6 cm ²	[28]
Al ₂ O ₃	SALD	200	>1	0.13–0.10	n.r.	[29]
Al ₂ O ₃	SALD	150	n.r.	0.13	n.r.	[30]
Al ₂ O ₃	PE AP t-ALD (Ar + O ₂ plasma)	80	n.r.	0.18–0.19	Various	[31]
Al ₂ O ₃	PE SALD (Ar + O ₂ plasma)	75	n.r.	0.16–0.17	Various	[32]
Al ₂ O ₃	t-ALD (Beneq)	75–150	n.r.	0.18–0.15	n.r.	[32]
Al ₂ O ₃	AP t-ALD	50–120	>0.05	0.105	Various	[33]
Al ₂ O ₃	SALD	200	n.r.	0.12	n.r.	[34]
Al ₂ O ₃	SALD (Al precursor: DMAI) ^a	150–300	>0.07	0.09–0.13	6.25 × 6.25 cm ²	[19]
AlZnO	SALD (DEZ + DMAI)	100–300	n.r.	0.10–0.19	6.25 × 6.25 cm ²	[19]
ZnO	t-ALD (Microchemistry F-120)	105–180	0.13–0.18	0.15–0.21	n.r.	[35]
ZnO	SALD	100–300	0.02–0.2	0.11–0.22	6.25 × 6.25 cm ²	[19]
ZnO	SALD (TNO)	75–250	0.3–0.9	0.18	3-cm-wide ring	[36]
ZnO	SALD (V-CUCP)	150	1.1	0.95	3.5 × 5.5 cm ²	[37]
ZnO	SALD (SoLayTec)	100–260	0.29–0.61	0.09–0.19	15.6 × 15.6 cm ²	[38]
ZnO	SALD (oxide mixture; H ₂ O ₂ , H ₂ O, O ₂)	<200	n.r.	0.12	n.r.	[16]
ZnO	SALD	200	n.r.	0.12	n.r.	[26]
ZnO	SALD	200	n.r.	0.155	n.r.	[39]
ZnO	SALD	120	n.r.	0.18	n.r.	[30]
Zn(O, S)	SALD (oxide mixture; H ₂ O, H ₂ S)	120	n.r.	0.15	n.r.	[40]
ZnO	SALD	95	0.17	0.1	n.r.	[41]
ZnO/ZnS	SALD (oxide mixture; H ₂ O, H ₂ S)	100–200	n.r.	0.13 (ZnO), 0.15 (ZnS)	n.r.	[42]
ZnO	SALD	200	n.r.	0.20	n.r.	[34]
ZnO	SALD	200	0.3	0.18	15 × 15 cm ²	[43]
In:ZnO	PE-SALD	160	n.r.	0.14	Ø15 cm	[44]
In:ZnO	SALD	200	>0.1	n.r.	15 × 15 cm ²	[43]
In ₂ O ₃	SALD	200	n.r.	0.004	15 × 15 cm ²	[43]
TiO ₂	t-ALD (Microchemistry F-120)	150	<0.01	0.04	n.r.	[45]
TiO ₂	SALD (V-CUCP)	150	0.26	0.15	3.5 × 5.5 cm ²	[21]
TiO ₂	SALD (Beneq TFS-200)	80–120	n.r.	0.015–0.045	n.r.	[46]
TiO ₂	PE-SALD (O ₂ + N ₂ plasma)	65	n.r.	0.15	0.33 × 1.2 cm ²	[47]
TiO ₂	SALD Pen	150	n.r.	0.075	Various	[48]
TiO ₂	SALD (Atlant3D)	120–300	n.r.	0.035	n.r.	[49]
MgO	t-ALD (viscous-flow ALD reactor)	150	0.09	0.14	5 × 5 cm ²	[50]
MgO	SALD (LMGP)	220	n.r.	0.25	2.5 × 2.5 cm ²	[51]

Continued.

TABLE I. (Continued.)

Material	Method	T_{dep} (°C)	Growth rate (nm s ⁻¹)	Growth rate (nm per cycle)	Sample size	Ref.
SiO ₂ (etching)	PE-SALD (O ₂ plasma)	<200	0.32	n.r.	Ø15 cm	[52]
SiO ₂	PE-SALD (Beneq)	Up to 200 °C	0.55	n.r.	Ø20 cm	[53]
SnO ₂	t-ALD (different setups)	75–400	n.r.	0.01–1	Various	[54]
SnO ₂	SALD (LMGP)	140–200	n.r.	0.85	5 × 2.5 cm ²	[54]
SnO	t-ALD (different setups)	100–200	n.r.	0.13–0.20	Various	[55]
SnO	SALD (TNO)	100–210	n.r.	0.09–0.55	3-cm-wide ring	[56]
SnO _x	SALD	80–150	n.r.	0.07–0.15	7 × 7 cm ²	[57]
SnO _x	PE SALD (O ₂ + Ar plasma)	80–150	n.r.	0.11–0.16	Various	[58]
Cu ₂ O	t-ALD (different setups)	110–220	0.001–0.003	0.006–0.012	Various	[59]
Cu ₂ O	SALD (V-CUCP)	100–225	1.3	n.r.	6 × 2 cm ²	[60,61]
Cu ₂ O	SALD (LMGP)	180–260	0.018–0.059	0.016–0.052	5 × 2.5 cm ²	[59]
ZrO ₂	SALD pen reactor	150	n.r.	0.21	Various	[48]
ZrO ₂	PE-SALD (O ₂ plasma)	150–250	n.r.	< 0.14	15 × 15 cm ²	[62]

^aDMAI = dimethylaluminum isopropoxide; n.r. = not reported.

half reactions take place on the substrate. For example, precursor A may be water vapor, which chemisorbs onto the substrate to form a layer of hydroxyl groups covering the entire surface. Precursor B could be an organometallic compound (e.g., diethylzinc), which reacts with the hydroxyl groups to form a monolayer of the oxide. Having all reactions take place at the surface enables ALD films to be highly conformal to high-aspect-ratio nanostructured substrates and ensuring that chemisorption reactions take place over the entire surface results in pinhole-free films. However, it is then essential to ensure that precursors A and B do not react in the gas phase to avoid chemical vapor deposition (CVD) and oxide particles forming in the gas phase. In conventional ALD, this requires a sufficiently long purge step between each precursor pulse, such that a vacuum chamber is typically required, and these purge steps can take up to 50% of the total deposition time [9]. In spatial ALD, most commercial designs so far operate under low vacuum; however, newer designs—particularly those targeting the energy and electronics applications discussed in this review—can be operated under atmospheric conditions (i.e., atmospheric pressure, or AP-SALD). In almost all AP-SALD reactors, a wide curtain of inert gas (usually N₂ or Ar) is used between the precursor gas channels [Figs. 1(a) and 1(b)]. By having this reactor gas manifold brought close to the substrate (manifold-substrate gap on the order of 10–20 μm), there is a sufficiently high pressure gradient to direct gases from inlet to exhaust, which helps to avoid precursor mixing in the gas phase. This small manifold-substrate spacing can be achieved by either floating the manifold over the substrate or vice versa and the substrate-manifold spacing is naturally adjusted until a high pressure gradient exists between inlet and exhaust. In this case, the inert gas curtains are also acting as gas bearings to ensure that the substrate or manifold is floating [Fig. 1(b), top].

Another approach is to mechanically hold the manifold over the substrate [Fig. 1(b), bottom]. This allows the manifold-substrate spacing to become a free parameter that can be adjusted. The advantage is that increasing this spacing allows some mixing between precursors A and B to take place in the gas phase, enabling either mixed ALD-CVD growth, or pure CVD growth, which leads to a higher growth rate. Whether this mechanical-close-proximity reactor is operating in ALD or CVD mode can be determined by measuring the growth per cycle as a function of the exposure time, which can be adjusted by the speed at which the substrate is oscillated underneath the gas manifold. In ALD growth, saturation is reached for long exposure times, resulting in the growth per cycle leveling off as the exposure time is increased further [Fig. 1(c)]. By contrast, in CVD growth, the growth per cycle will monotonically increase with further increases in exposure time.

We have found in many instances that operating AP-SALD in CVD mode maintains the advantages of ALD-grown films, including pinhole-free films, having the same crystallinity at the same deposition temperature, and conformality to nanostructured substrates [20,60,66]. An example of Al₂O₃ films grown using an SALD with the mechanical-close-proximity design in ALD mode on ZnO nanorods is shown in Fig. 1(d) (right), where it can be seen that the Al₂O₃ layer is uniformly 25 nm thick. In CVD mode, ZnO has also been successfully grown to conformally cover ZnO nanorods [Fig. 1(d), left]. On the other hand, when operating in pure ALD mode (i.e., no CVD component), the maximum deposition rate that can be achieved with SALD depends on the kinetics of each particular process and the nature of the sample to be coated, in which slow growth occurs on high-aspect-ratio features or porous substrates (see Sec. IV).

III. ENERGY-CONVERSION-DEVICE APPLICATIONS

A. Silicon photovoltaics

Early efforts to commercialize spatial ALD have focused particularly on the silicon-PV industry, which dominates the global PV market [67,68]. Work by Hoex and co-workers over a decade ago has shown that ALD-grown Al_2O_3 effectively passivates the surface of c-Si, leading to low surface-recombination velocities of 2 cm s^{-1} [Fig. 2(a)] [69,78,79]. The passivation from ALD-grown Al_2O_3 comes about because (1) deposition onto silicon results in the formation of a thin layer of SiO_x , which provides chemical passivation, (2) Al_2O_3 is doped with H, which diffuses into the c-Si bulk, passivating dangling bonds, and (3) Al_2O_3 has a negative fixed charge, which leads to field-effect passivation. The last point occurs because the negative fixed charge in Al_2O_3 (typically on the order of 10^{13} cm^{-2} [69]) causes upward band bending at the Si- Al_2O_3 interface through an accumulation of holes (for *p*-type c-Si bulk), or depletion of electrons (for *n*-type c-Si bulk). This space-charge region separates electrons

and holes [Fig. 2(b)], reducing the probability of electron-hole annihilation through nonradiative recombination via defects at the surface of c-Si. Dingemans and Kessels have illustrated the effects of chemical and field-effect passivation on the effective surface-recombination velocity (S_{eff}) of c-Si through numerical simulations [Fig. 2(c)]. Reducing the interface defect density (N_{it}) from 10^{12} to 10^{10} cm^{-2} through chemical passivation results in S_{eff} reducing by 2 orders of magnitude. Increasing the negative fixed interface charge (Q_f) to above 10^{11} cm^{-2} also leads to a substantial reduction in S_{eff} . Postannealing Al_2O_3 films grown by a variety of ALD-based methods is important to increase the Q_f to 10^{12} – 10^{13} cm^{-2} [Fig. 2(d)], which, as shown in Fig. 2(c), enables low S_{eff} . Detailed investigations into Al_2O_3 grown by conventional ALD have found the optimal postannealing temperature range to be 350–450 °C, with a duration of only 1–2 min being adequate [76,80]. Further improvements in passivation through increases in Q_f could be achieved through plasma-assisted growth of Al_2O_3 [Fig. 2(d)]. However, these plasma-ALD Al_2O_3 films have required postannealing in order to reduce the interface defect density (D_{it}), which

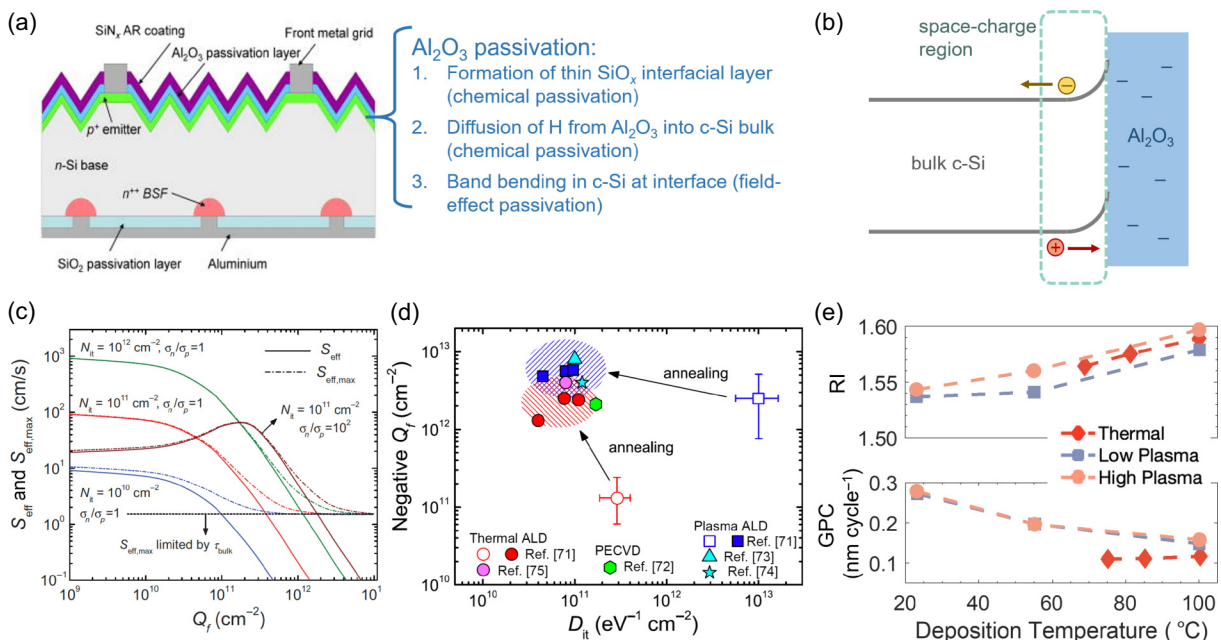


FIG. 2. The use of ALD for silicon-interface passivation for PVs. (a) A sketch of a common industrial silicon-PV device (in this case, Al back-surface field), illustrating the use of Al_2O_3 for front passivation. Adapted with permission from Ref. [69]. Copyright 2008, American Institute of Physics. (b) An illustration of the band bending in c-Si interfaced with Al_2O_3 that has a negative fixed charge. Adapted with permission from Ref. [70]. Copyright 2021, Springer Nature. (c) The calculated effective surface-recombination velocity (S_{eff}) for silicon for different negative fixed charges (Q_f) at one interface, depending on the interface defect density (N_{it}) and the ratio of the electron and hole capture cross sections (σ_n/σ_p). The upper bound to the surface-recombination velocity assuming only recombination at wafer surfaces ($S_{\text{eff},\text{max}}$) is also provided. (d) The Q_f value of Al_2O_3 thin films versus the midgap interface defect density (D_{it}), showing the effect of annealing. Data obtained from Refs. [71–75]. Parts (c) and (d) reproduced with permission from Ref. [76]. Copyright 2012, American Institute of Physics. (e) A comparison of the refractive index (RI) and growth per cycle (GPC) of Al_2O_3 deposited by SALD without plasma (thermal) and with low- and high-voltage plasma (N_2 and O_2). Data from Ref. [77].

would have otherwise led to high S_{eff} [76]. More detailed reviews delving into the engineering of ALD Al_2O_3 films for passivating c-Si for PVs can be found in Refs. [76,81–83].

For SALD Al_2O_3 , improvements in film density have also been obtained through plasma-assisted growth [77]. Roozeboom and co-workers have used a dielectric-barrier-discharge plasma source and directly introduced the plasma (20% O_2 , 80% N_2) to the growing film. As shown in Fig. 2(e), Al_2O_3 films deposited with a high-power plasma (5 W cm^{-2}) had a higher refractive index than thermally grown SALD films (using water vapor as the oxidant), indicating a higher film density. Plasma-SALD films also had a higher growth per cycle than thermal SALD, especially at low deposition temperatures [Fig. 2(e)] [77,84]. Beyond directly depositing Al_2O_3 onto c-Si, the use of ZnO or Al-doped ZnO , grown by AP-SALD, between c-Si and Al_2O_3 has been found to be effective in enhancing field-effect passivation by increasing the band bending of Si [85]. SALD MoO_x has also been found to be effective as a hole-selective contact for c-Si and could replace *p*-type H-passivated amorphous silicon for PVs made in the heterojunction cell architecture [86]. A more detailed discussion of how MoO_x , as a high-work-function *n*-type oxide, could transport holes is given in Ref. [87].

In early work, temporal ALD (t-ALD) was considered to be too slow for c-Si PV manufacturing [23,88,89]. On the other hand, it can be seen from Table I that while the growth per cycle of SALD is comparable to that of t-ALD for Al_2O_3 deposition, SALD has a growth rate that is orders of magnitude higher. This has been considered to be advantageous for reaching the required manufacturing throughput of c-Si PVs, which in 2010 was approximately 2000–3000 wafers per hour [23]. As a result, commercial SALD systems have been particularly designed for c-Si PVs, especially from LeviTech and SoLayTec [17,21], which could achieve throughputs of 3600 wafers per hour (LeviTech) and 4500 wafers per hour (SoLayTec) [17,21]. However, the assumed throughput advantage of SALD has recently been displaced by making t-ALD reactors larger. That is, while the total deposition time of ALD remains long, each reactor contains a large batch of silicon wafers. LeadMicro have adopted this design and have achieved throughputs well above 10 000 wafers per hour for Al_2O_3 passivation layers [90]. As a result, LeadMicro has largely displaced SALD from the mainstream PV sector. However, the use of large ALD reactors is disadvantageous in (1) having a long path length for precursor gases to diffuse to, (2) offering little flexibility in the manufacture of c-Si PVs, which needs to proceed on a batch basis, and (3) leading to significant wastage of precursor gases in the interior of the reactor. Opportunities therefore remain for SALD to offer semicontinuous production of passivation layers on c-Si PVs, with potentially small precursor

wastage and improved control of the uniformity of the thin films deposited.

B. Emerging photovoltaics

In thin-film PVs, AP-SALD has been used to deposit a wide range of binary and multicomponent oxides. The advantage of the short deposition time of SALD is that it can not only deposit oxides onto the thermally stable conducting-glass substrate (i.e., beneath the photoactive layer) but also on top of the photoactive layer, either directly or with the photoactive layer protected with a charge-transport layer. This opens up the range of applications for these functional oxides, not just as charge-transport layers but also as layers to mechanically and environmentally protect the photoactive layer. In this section, we discuss the materials developed by AP-SALD for use in thin-film PVs as the oxide underlayer [Fig. 3(a)], overlayer [Fig. 3(c); i.e., where there is at least one charge transport layer between the absorber and the SALD oxide] or the buffer layer [Fig. 3(e); i.e., with the SALD oxide directly grown on the absorber layer], as well as for the encapsulation of devices.

1. Oxide underlayers

The simplest way to integrate AP-SALD oxides into a PV device is to deposit the oxide film onto the transparent-conducting-oxide (TCO)-coated glass substrate, followed by depositing the rest of the device stack on top [Fig. 3(a)]. This is because commercial TCOs (typically indium tin oxide and fluorine-doped tin oxide) are thermally stable over the entire deposition-temperature window usually used for AP-SALD oxides (from room temperature up to 350 °C) [93]. As such, there are no severe restrictions on the temperature, oxidant, or duration of the deposition used, enabling a wide range of materials and processing parameters to be explored.

In an early effort, TiO_2 thin films have been used as the electron-transport layer (ETL) in organic-bulk-heterojunction (BHJ) solar cells [94]. In BHJ solar cells, the electron donor [e.g., poly(3-hexylthiophene-2,5-diyl), or P3HT] and the electron acceptor (e.g., [6,6]-phenyl-C₆₁-butyric acid methyl ester, PC₆₁BM) are mixed together, ensuring that photogenerated excitons only need to diffuse a short distance before they are separated into free electrons and holes at the donor-acceptor interface [95,96]. Therefore, between the BHJ and the electrodes, there need to be charge-selective layers that only extract one charge carrier, while blocking the other. The AP-SALD ETL has been deposited at 100 °C (amorphous) and compared to films deposited at 350 °C, and by spray pyrolysis at 450 °C. Due to the pinhole-free nature of the AP-SALD films, ultrathin films (12 nm) of amorphous TiO_2 have performed equally to thicker films (80 nm) deposited at higher temperature [94], which represents a saving in both

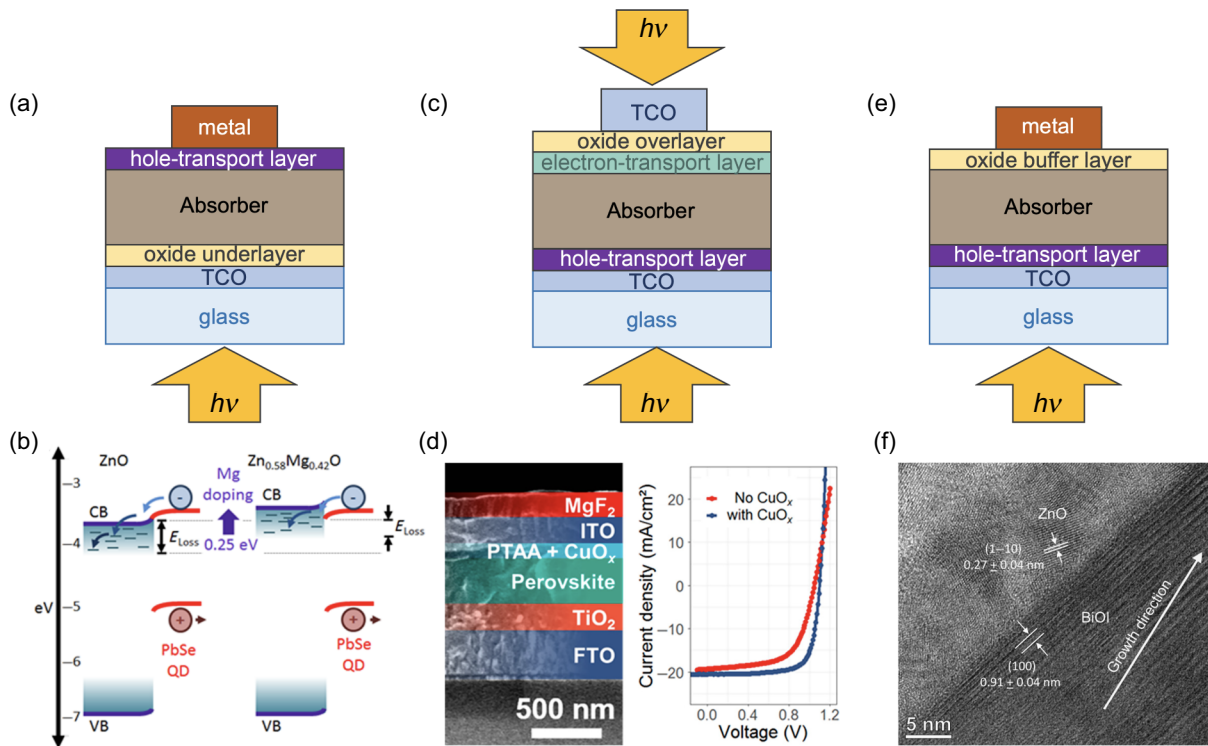


FIG. 3. Applications of AP-SALD oxides in PVs. An illustration of the use of oxides as the (a),(b) underlayer, (c),(d) overlayer, and (e),(f) buffer layer. When used as the overlayer, the oxide is deposited over the absorber, which is already protected by a charge-transport layer (typically an organic material), whereas when used as the buffer layer, the oxide is directly deposited onto the absorber. (b) An illustration of electron-affinity tuning through the Mg content in Mg:ZnO and how this could reduce the thermalization loss of the injected electron in ZnO, leading to improvements in the open-circuit voltage. Reproduced under the terms of the CC-BY license from Ref. [91]. Copyright 2014, The Authors. (d) A cross-section scanning-electron-microscopy (SEM) image of a semitransparent perovskite device, showing the layers used, including the Cu_2O overlayer (left), and the current density-voltage curves of semitransparent devices without and with the Cu_2O overlayer. Reproduced with permission from Ref. [60]. Copyright 2020, American Chemical Society. (f) A transmission-electron-microscopy (TEM) image of the ZnO-BiOI interface in BiOI PVs. Reproduced with permission from Ref. [92]. Copyright 2022, The Authors.

the processing time and the use of materials. Similarly, in the same year, Thierich *et al.* prepared TiO_x thin films by atmospheric pressure plasma ALD (APP-ALD) as ETLs for P3HT:PC₆₁BM BHJ devices and obtained the same power-conversion efficiency (PCE) as for devices using conventional ALD blocking layers [97]. AP-SALD could therefore prepare TiO_2 films that perform similarly to these batch-based techniques.

Another early effort has involved the demonstration of AP-SALD ZnO as the ETL in BHJ solar cells [98]. ZnO is a highly effective and commonly used ETL because its electron affinity is well aligned with the lowest occupied molecular orbital (LUMO) of common electron acceptors, while simultaneously having a high ionization potential, enabling effective hole blocking. The authors have shown that AP-SALD can grow dense and compact thin films of ZnO with similar crystallinity and electronic properties as ALD-grown films, with good wettability for the P3HT:PC₆₁BM blend, leading to BHJ devices with PCEs

reaching up to 3.6% (Table II). Importantly, 40-nm-thick ZnO films have been sufficient for forming a complete layer between the indium tin oxide TCO and BHJ blend to prevent shunting, and these ZnO films could be deposited in only 1.5 min (without vacuum), significantly shorter than the total processing time for similar ALD films. Furthermore, the as-deposited ZnO films were crystalline, with a mobility of $3.4 \pm 0.1 \text{ cm}^2 \text{ V}^{-1} \text{ s}^{-1}$, 2 orders of magnitude higher than the mobility of spin-coated ZnO nanoparticles, and also had high transmittance >90% in the visible wavelength range. As a result, these rapidly grown AP-SALD films effectively transport electrons, with minimal contributions to the series resistance or parasitic optical losses in the device [98].

The properties of these AP-SALD films could be tuned through postprocessing or compositional tuning. For example, the electron carrier concentration could be lowered through postannealing in air or doping with N [115]. For example, doping ZnO with $0.22 \pm 0.04 \text{ at.\% N}$ [by

TABLE II. A comparison of the performance achieved in thin-film PVs using spatial ALD (SALD) versus conventional t-ALD. The t-ALD examples are selected to serve as points of comparison for the PVs making use of spatial ALD oxides. A comprehensive review specially discussing ALD oxides for PVs is provided in Ref. [99].

Material	Method	Cell structure	V_{OC} (V)	J_{SC} (mA cm $^{-2}$)	FF (%)	PCE (%)	Ref.
Oxide underlayers							
ZnO	t-ALD	ITO/ZnO/PbS/Au	0.54 ± 0.02 (0.55)	34.5 ± 0.6 (35.2)	39 ± 1 (40) (7.6)	7.2 ± 0.5 (7.6)	[100]
ZnO	t-ALD	ITO/ZnO/perovskite/spiro-OMeTAD/MoO _x /Ag	0.97 ± 0.02	14.2 ± 0.7	48 ± 4	6.6 ± 0.4	[101]
ZnO	SALD	ITO/ZnO/P3HT:PC ₆₁ BM/ MoO _x /Ag	0.60 ± 0.01	9.7 ± 0.3	54 ± 3	3.3 ± 0.3	[98]
ZnO:N	SALD	ITO/ZnO:N/PbS/ MoO _x /Au	0.46	10	32.6	1.5	[102]
ZnO:N	SALD	ITO/ZnO:N/PbSe/ MoO _x /Au	0.4	17.5	~ 42	~ 3	[102]
ZnO	SALD	ITO/ZnO/P3HT/ MoO _x /Ag	0.22	0.17	37	0.014	[103]
ZnO:N	SALD	ITO/ZnO:N/P3HT/ MoO _x /Ag	0.11	0.50	36	0.020	[103]
ZnO/ZnO:N	SALD	ITO/ZnO/ZnO:N/P3HT/ MoO _x /Ag	0.20	0.68	43	0.058	[103]
Mg:ZnO	SALD	ITO/Mg:ZnO/PbSe/ MoO _x /Au	0.51 ± 0.02 (0.53)	18 ± 2 (21)	32 ± 4 (35) (3.7)	3.2 ± 0.8 (3.7)	[91]
SnO ₂	t-ALD	ITO/SnO ₂ /perovskite/spiro-OMeTAD/Au	1.09 ± 0.03	21.4 ± 0.6	70 ± 2	16.2 ± 0.7	[104]
TiO ₂	t-ALD	ITO/TiO ₂ /perovskite/spiro-OMeTAD/Au	1.03	20.3	76	15.8	[105]
TiO _x	APP-ALD	ITO/TiO _x /P3HT:PC ₆₁ BM/ MoO _x /Ag	0.52	11.1	56	3.2	[97]
TiO ₂	t-ALD	ITO/TiO ₂ /P3HT:PC ₆₁ BM/ PEDOT:PSS/Ag	0.53	7.17	51	1.99	[94]
TiO ₂	SALD	ITO/TiO ₂ /PbSe/ MoO _x /Au	0.49 ± 0.01 (0.51)	11 ± 1 (15)	28 ± 2 (37) (2.8)	1.7 ± 0.3 (2.8)	[106]
TiO ₂ /Nb ₂ O ₅	SALD	ITO/TiO ₂ /Nb ₂ O ₅ /PbSe/ MoO _x /Au	0.53 ± 0.01 (0.54)	13.9 ± 0.2 (15.5)	30 ± 4 (32) (2.68)	2.25 ± 0.05 (2.68)	[106]
NiO _x	t-ALD	FTO/NiO _x /perovskite/ PC ₆₁ BM/BCP/Ag	1.03 ± 0.01	20.8 ± 0.6	75.0 ± 0.6	16.7 ± 0.3	[107]
NiO _x	SALD	ITO/NiO _x /perovskite/ PC ₆₁ BM/Al	1.02 (1.08)	22.1 (23.0)	76 (81)	15.7 (17.1)	[93]
Oxide overlayers							
ZnO	SALD	ITO/NiO/perovskite/ PC ₆₁ BM/ZnO NPs/SALD ZnO/ITO (bottom illumination)	1.01 ± 0.01 (1.00)	19.7 ± 0.3 (19.8)	67 ± 6 (73)	13 ± 1 (15)	[41]
ZnO	SALD	ITO/NiO/perovskite/ PC ₆₁ BM/ZnO NPs/SALD ZnO/ITO (top illumination)	0.99 ± 0.01 (1.00)	20.4 ± 0.3 (20.4)	69 ± 8 (70)	13 ± 1 (14)	[41]
TiO _x	SALD	ITO/NiO _x /perovskite/ PC ₆₁ BM/TiO _x /BCP/Al	0.99 ± 0.01	21.5 ± 0.5	76.4 ± 0.3	16.2 ± 0.4	[66]
SnO ₂	t-ALD	ITO/PEDOT:PSS/MAPbI ₃ / PC ₆₁ BM/AZO NP/SnO _x /Ag	0.85 ± 0.02	19.1 ± 0.5	73 ± 2	12.0 ± 0.5	[57]
SnO _x	SALD	ITO/PEDOT:PSS/MAPbI ₃ / PC ₆₁ BM/AZO NP/SnO _x /Ag	0.89 ± 0.04	18.5 ± 0.5	76 ± 2	12.5 ± 0.7	[57]
SnO _x	SALD	TO/NiO _x /perovskite/ PC ₆₁ BM/SnO _x BCP/Ag			82 ± 2	18 ± 1 (19.7)	[66]

Continued.

TABLE II. (Continued.)

Material	Method	Cell structure	V_{OC} (V)	J_{SC} (mA cm $^{-2}$)	FF (%)	PCE (%)	Ref.
Cu ₂ O	SALD	FTO/TiO _x /perovskite/ PTAA/Cu ₂ O/Au	1.07 ± 0.03 (1.11)	22 ± 1 (24)	72 ± 3 (76)	18 ± 2 (20)	[60]
Cu ₂ O	SALD	Ag/ITO/Cu ₂ O/ α -Si:H(i)/c- Si(n)/ α -Si:H(i)/ α -Si: H(n)/ITO/Ag	0.584	36.8	63.8	13.7	[108]
Buffer layers							
Mg:ZnO	t-ALD	Glass/Cr/ITO/Cu ₂ O/ Mg:ZnO/Al:ZnO	0.55	~7	~43	1.67	[109]
Ga ₂ O ₃	t-ALD	Au/Cu ₂ O/Ga ₂ O ₃ /Al:ZnO	1.20	7.37	44.7	3.97	[110]
Mg:ZnO	SALD	Au/Cu ₂ O/Mg:ZnO/ITO	0.65	6.9	49.2	2.2	[111]
Mg:ZnO	SALD	ITO/Cu ₂ O/Mg:ZnO/ITO	0.42 ± 0.01 (0.43)	5.8 ± 0.1 (5.9)	49 ± 2 (52)	1.2 ± 0.1 (1.4)	[112]
ZnO	SALD	ITO/NiO _x /BiOI/ZnO/Al	0.75 ± 0.01 (0.75)	6.3 ± 0.5 (7.0)	39 ± 3 (43)	1.79 ± 0.03 (1.82)	[113]
Cu ₂ O	SALD	ITO/ZnO/ECD Cu ₂ O/SALD Cu ₂ O/Au	0.32	5.8	43	0.77	[114]

using NH₃ (aq) as the oxidant rather than water] lowers the carrier concentration from approximately 10¹⁹ cm⁻³ (undoped ZnO) to approximately 10¹⁷ cm⁻³ (ZnO:N). This leads to a reduction in interface recombination in PbS colloidal quantum dot solar cells, improving the PCE from 0.8% (ZnO) to 1.5% (ZnO:N) [102].

Beyond the carrier concentration, the band positions of ZnO can also be tuned, e.g., through Mg incorporation, which lowers the electron affinity because of mixing between Mg 3s orbitals and empty Zn 4s orbitals in the lower conduction band [Fig. 3(b)]. Oxides with two metal components or more can be achieved in AP-SALD through co-doping, in which the metal precursors are mixed together in the gas phase before being introduced to the gas manifold [Fig. 1(b)]. Lowering the electron affinity of ZnO through Mg incorporation has resulted in reduced energy losses for the electrons extracted in PbSe colloidal quantum dot solar cells [91], as well as hybrid solar cells (in which exciton separation is achieved at the ZnO-P3HT interface) [37], leading to improvements in PCE [Fig. 3(b); Table II].

Importantly, AP-SALD films maintain the high conformality of ALD films to high-aspect-ratio surfaces, such as nanorods [Fig. 1(d)]. This occurs despite the AP-SALD reactor depositing films in “CVD mode.” For example, the authors have shown that ZnO nanorods could be conformally coated with ZnO:N and Mg:ZnO films grown by AP-SALD in CVD mode and this has led to improvements in PCE in both hybrid and PbSe colloidal quantum dot solar cells through improvements in the open-circuit voltage [20].

Apart from doping, AP-SALD can also be used to deposit bilayers of functional thin films. For example, the authors have shown that using a layer of ZnO:N between ZnO and P3HT leads to a doubling in the short-circuit

current density. This has been attributed to an enhancement in the detrapping of electrons at the surface of ZnO by photogenerated holes when the ZnO was N doped, thus enabling more facile exciton dissociation [103]. Similarly, adding a layer of Nb₂O₅ in between TiO₂ and P3HT enhances the dissociation of excitons and reduces the nongeminate recombination of excitons by passivating the deep traps present in TiO₂, improving both the open-circuit voltage and short-circuit current density [106]. While the PCEs of these hybrid devices were low, similar effects have been observed using PbSe colloidal quantum dots instead of P3HT and devices with TiO₂/Nb₂O₅ have reached up to 2.68% PCE (Table II) [106]. These improvements are attributed to the cascade in energy levels obtained by introducing the Nb₂O₅ interlayer, which helps to separate electrons and holes [106].

Note that in these discussions, it is reasonable to compare efficiencies within individual studies but making comparisons between works is difficult, even if the same AP-SALD reactor is being used. This is because the PCE is primarily determined by the properties of the absorber layer being used. For example, while compositional tuning of ZnO improves the performance of PbS colloidal quantum dot solar cells, the highest PCEs reported in Table II are with ALD-grown ZnO, because of the higher quality of the quantum dots prepared in this particular study [100].

Finally, AP-SALD has also been used to prepare *p*-type metal-oxide hole-transport layers for lead-halide perovskite solar cells (Table II). Here, MacManus-Driscoll and co-workers have used bis(methylcyclopentadienyl) nickel as the Ni precursor and O₂ gas as the oxidant. Owing to the low reactivity of the Ni precursor, the substrate needed to be heated to 350 °C, and the substrate-manifold spacing was increased to 100 μm [Fig. 1(b)], such that the reactor proceeded in CVD mode. This

was necessary in order to obtain an appreciable growth rate, such that 10-nm-thick films were obtained after 20 scans of the substrate underneath the gas manifold. These films led to improved PCEs (of up to 17.1%) compared to poly(3,4-ethylenedioxythiophene) polystyrene sulfonate (PEDOT:PSS) (up to only 13.0%) [93] and comparable to the performance of perovskite solar cells with ALD NiO_x (Table II) [116].

2. Oxide overlayers

From Table II, it can be seen that there are few works on the use of *n*-type oxides as ETLs for *n-i-p*-structured lead-halide perovskite solar cells. Thus far, the few demonstrations of perovskite PVs with the three most common *n*-type oxides used in thin-film PVs (ZnO , TiO_2 , and SnO_2) have delivered PCEs well below those reached using conventional spray-pyrolyzed TiO_2 or chemical-bath-deposited SnO_2 (>25% PCE) [117]. However, a critical advantage of ALD and AP-SALD is the capability to deposit compact thin films on top of lead-halide perovskite device stacks, which cannot be realized with spray pyrolysis or chemical bath deposition because of thermally or chemically induced degradation of the halide perovskite or organic charge transport layers. Indeed, early work on monolithic perovskite-silicon tandem PVs has made use of ALD to grow a layer of SnO_2 and zinc tin oxide on top of the perovskite top cell [Fig. 3(c)], to mechanically protect it against damage when sputter depositing the indium tin oxide TCO on top. At the same time, the limiting factor of ALD is that it is inherently a slow deposition method. There is therefore a limit to the maximum temperatures (up to 80–110 °C) and times that could be used to deposit oxide thin films, which restricts the range of electronic properties and crystallinity achievable [66,107,118,119].

Riedl and co-workers have used AP-SALD to deposit SnO_2 onto methylammonium lead iodide (MAPbI_3) perovskite devices that were first protected by a layer of $\text{Al}:\text{ZnO}$ nanoparticles [57]. Despite this protective layer, they found that the SnO_2 films could not be grown at above 80 °C without causing a decrease in the PCE, which was similar to what they found when using conventional ALD to grow the SnO_2 layer [57]. Using the close-proximity AP-SALD system in the MacManus-Driscoll group, operating in CVD mode, Hoye and colleagues found that SnO_2 could be grown at 150 °C using water vapor as the oxidant to obtain devices that were similar in performance to the control devices made without any AP-SALD oxide layer [66]. The lower damage was attributed to the short deposition time, which was completed within a couple of minutes (as opposed to >30 min to obtain comparable films by conventional ALD). Nevertheless, improved performance was still obtained by using milder growth conditions (100 °C, and with O_2 as the oxidant instead). By optimizing the thickness of this SnO_2 layer to 60 nm, the

PCE of triple-cation perovskite solar cells was improved from 16.5% (no oxide buffer layer) to 19.4% (with a 60-nm SnO_2 buffer layer). This came about because the dense SnO_2 layer blocked the shunt pathways present in the spin-coated PC_{61}BM layer deposited over the perovskite film, leading to improvements in the fill factor to $82 \pm 2\%$. Similarly, TiO_2 overlayers could be deposited onto either thermally sensitive MAPbI_3 device stacks or more stable triple-cation device stacks at up to 180 °C without degrading the performance. This was because these TiO_2 films could be deposited well within 1 min [66].

At the same time, such results could not be obtained with ZnO . This is because diethylzinc degrades the perovskite film [41,120]. Furthermore, ZnO has a high isoelectric point and is known to degrade iodide-based perovskites [121].

The majority of works on oxide overlayers for perovskite solar cells have focused on the growth of *n*-type oxides on *p-i-n*-structured devices, because *n*-type oxides are more established in the field. However, the record PCEs for single-junction halide perovskite PVs have typically come from *n-i-p*-structured devices [122,123]. Hoye and colleagues selected Cu_2O as a *p*-type buffer layer to investigate, because this is a well-known *p*-type oxide, like NiO_x . But, unlike NiO_x , Cu_2O can be grown by AP-SALD at lower temperatures, down to 100 °C, when using allyloxytrimethylsilyl hexafluoroacetylacetone copper(I) (Cupraselect®) as the metal precursor and water vapor as the oxidant [60,61]. These films have $4.3 \pm 2 \text{ cm}^2 \text{ V}^{-1} \text{ s}^{-1}$ mobility, which is orders of magnitude higher than that of the poly[bis(4-phenyl)(2,4,6-trimethylphenyl)amine (PTAA) hole-transport layer onto which it was deposited in the perovskite device stack. Furthermore, the valence-band maximum (VBM) of the Cu_2O deposited, $5.3 \pm 0.2 \text{ eV}$, is well aligned with the VBM of the perovskite absorber and the highest occupied molecular orbital level of the PTAA (5.25 eV), making the buffer layer well suited for hole extraction. Although Cu_2O absorbs in the visible wavelength range, Hoye and colleagues could obtain compact films that were only 3–5 nm thick, such that the transmittance was >95% across the entire visible and near-infrared wavelength ranges. These thin Cu_2O films could be deposited within a couple of minutes, thus avoiding thermal degradation of the perovskite device stack, but were sufficient to mechanically protect the perovskite device from damage when sputter depositing the TCO top electrode [Fig. 3(d)]. As a result, semi-transparent *n-i-p*-structured perovskite devices with 20% PCE (Au top electrode) or 16.7% PCE (indium tin oxide top electrode) were obtained, and the latter allowed us to successfully demonstrate >24%-efficient four-terminal perovskite-silicon tandems [Fig. 3(d)] [60].

Given that it has been shown to be possible to deposit oxide buffer layers by AP-SALD onto perovskite thin films without bulk structural damage, an important question is

whether it is possible to directly deposit onto the halide perovskite itself, thus obviating the need for organic charge transport layers. Hoye and colleagues have found, however, that the direct deposition of the oxides onto perovskite films leads to a severe deterioration in performance [66].

Schulz and co-workers have directly deposited SnO_2 by ALD at 100 °C onto halide perovskite films and used hard x-ray photoelectron spectroscopy (HAXPES) to analyze the buried interface between SnO_2 and the halide perovskite [124]. They have concluded that the deterioration in performance comes about from the formation of chemical defects on the surface of the perovskite when exposed to the tin precursor [tetrakis(dimethylamino)tin] [124]. Hultqvist *et al.* have also believed that species form at the perovskite- SnO_2 interface when the SnO_2 is deposited by ALD, reducing device performance [125]. Hoye and colleagues have used this same precursor in AP-SALD. However, it was found that the direct deposition of SnO_2 at 100 °C onto either MAPbI_3 or triple-cation perovskites led to no bulk degradation products that could be found from x-ray-diffraction measurements [66], which was not the case in the work by Schulz and co-workers, using t-ALD [124]. Nevertheless, this does not preclude the possibility of the tin precursor chemically damaging the surface of the perovskite even when grown by AP-SALD. On the other hand, Hoye and colleagues have found that TiO_x grown by AP-SALD at either 100 °C or 150 °C in <1 min does not lead to any changes in the core-level peaks of Pb or I in MAPbI_3 incompletely covered with PC_{61}BM , although there was a narrowing in the N 1s peak [66]. Further work is needed to understand why degradation of the perovskite surface occurs when depositing oxides onto the perovskite by AP-SALD and to develop strategies to suppress this without requiring protective organic layers.

The limited degradation associated with the high deposition rates with AP-SALD has also been exploited to replace the *p*-doped amorphous silicon layer [*a*-Si:H(p)] with Cu_2O in silicon-heterojunction solar cells [108]. The interest in using *p*-type Cu_2O is that it is more transparent than *a*-Si. Muñoz-Rojas and co-workers have shown that shorter deposition times of Cu_2O at higher temperatures are more beneficial than longer depositions at lower temperatures. Conformal and uniform 10-nm-thick Cu_2O films have been deposited at a low thermal budget without reducing the passivation effect of the intrinsic hydrogenated amorphous silicon (*a*-Si:H(i)) layer, yielding high efficiencies for Si-based cells incorporating Cu_2O , with device areas of $3 \times 3 \text{ cm}^2$ [108].

3. Oxide buffer layers

While it has not been possible thus far to use AP-SALD to deposit oxides directly onto lead-halide perovskite films and achieve efficient performance, oxides

have successfully been directly incorporated onto Cu_2O and BiOI thin-film light absorbers by both t-ALD and AP-SALD [Fig. 3(e); Table II]. The advantage of directly depositing the oxide films onto the absorber layer (forming a buffer layer) instead of having an organic transport layer in between include being able to (1) form a *p*-*n* junction with the absorber layer to drive charge separation and (2) tune nonradiative recombination at the interface through the carrier concentration of the buffer layer and the band offset with the absorber layer [126]. Furthermore, AP-SALD, like ALD, is advantageous in growing pinhole-free thin films that are conformal to textured surfaces, which occurs in both BiOI and Cu_2O thin films [110,113]. Being able to achieve a continuous covering over textured absorber layer surfaces with a thin buffer layer (on the order of tens of nanometers) is advantageous in maximizing the illumination level to the heterojunction in a device illuminated from a transparent top electrode. The fine control over the thickness of films by AP-SALD also allows the optimal buffer layer thickness to be achieved that allows the full depletion region to be formed.

In Cu_2O solar cells, the conduction-band offset with *n*-type buffer layers (commonly ZnO) is a critical parameter that needs to be minimized to reduce interface recombination. Buffer layers with lower electron affinities, such as Mg:ZnO [109,112] or Ga_2O_3 [110], have been shown to improve performance through higher open-circuit voltages. However, the challenge with Cu_2O is that it is not the most thermodynamically stable phase of the Cu-O system under ambient conditions and there is a strong tendency for the lower-band-gap CuO to form, which acts as a nonradiative loss channel in Cu_2O solar cells [127,128]. In vacuum-based conventional ALD, the formation of the CuO layer during the deposition of the buffer layer could be suppressed by using a pulse of diethylzinc to reduce Cu(II) to Cu(I) during the deposition of amorphous zinc tin oxide [128]. However, it is difficult to adopt a similar strategy with AP-SALD operating in an open ambient environment, given the high chemical potential of O_2 present. Potentially, this could be addressed if the AP-SALD reactor were built within an isolated inert gas environment.

BiOI , on the other hand, is more stable against reacting with the oxidant, since Bi^{3+} is already in its most stable oxidation state. Hoye and colleagues have found BiOI to remain phase pure at processing temperatures up to beyond 400 °C [129]. Therefore, depositing ZnO thin films by AP-SALD at 150 °C or lower onto BiOI [Fig. 3(f)] did not lead to any observable phase impurities [113], although BiOI at the buried interface is I deficient due to the low formation energy of I vacancies [113]. However, BiOI is able to tolerate I vacancies and these do not affect the optoelectronic properties of the films [113,130].

Another application of AP-SALD is to create back-surface field PVs. Cu_2O grown by AP-SALD has a carrier concentration that is orders of magnitude higher

(approximately $10^{16} \text{ cm}^2 \text{ V}^{-1} \text{ s}^{-1}$) than that of electrochemically deposited Cu_2O (approximately $10^{14} \text{ cm}^2 \text{ V}^{-1} \text{ s}^{-1}$) [114]. Thus, depositing a thin (approximately 200-nm) layer of AP-SALD Cu_2O over the electrochemically deposited Cu_2O increases the built-in field gradient, which reduces the total thickness of the Cu_2O layer required to achieve full depletion from 3 to 1 μm . This reduces the required transport length of charge carriers, leading to increases in short-circuit current density, while still maintaining a high open-circuit voltage, thus leading to overall improvements in PCE [114].

There is clearly a wide range of applications of oxide overlayers prepared by SALD onto the PV device stack. NanoPrint Innovations Ltd. have recently commercialized a range of SALD reactors, spanning from the laboratory scale (for 30 mm \times 30 to 50 mm \times 50 mm substrates) to wafer-scale (12-in.-diameter substrates). These systems have been demonstrated to be capable of growing a wide range of oxides, from electrically insulating to conductive, including Al_2O_3 , ZnO , SnO_2 , and In_2O_3 .

4. Encapsulation

The highly compact nature of oxide films prepared by AP-SALD also gives them the advantage of having low

permeability for moisture or gas, with a water-vapor transmission rate (WVTR) as low as $10^{-5} \text{ g m}^{-2} \text{ day}^{-1}$ for SnO_2 and Al_2O_3 [32,57,131]. These WVTRs are similar to those of ALD-prepared films [132–136], such that these thin films can protect moisture-sensitive semiconductors from degradation in ambient air. Originally employed for encapsulation of organic light-emitting diodes (OLEDs) [137,138], AP-SALD films have more recently been used to protect lead-halide perovskite solar cells. For example, Musselman and co-workers have demonstrated the deposition of Al_2O_3 gas-diffusion barriers onto complete perovskite device stacks (i.e., that have the metal electrode deposited already), as shown in Fig. 4(a). N-doping and the incorporation of Zn have both been found to reduce the concentration of oxygen-related defects on the Al_2O_3 surface and produce more compact films, which has reduced the WVTR [131,140]. When used to encapsulate *n-i-p*- or *p-i-n*-structured perovskite devices, coating with 60-nm $\text{N:Al}_2\text{O}_3$ or Zn:AlO_x has led to greater than sixfold improvements in stability at both room temperature (with 55% relative humidity) and 65 °C (with 85% relative humidity). Importantly, the short processing time by AP-SALD allows higher processing temperatures (e.g., 130 °C) to be used without thermally

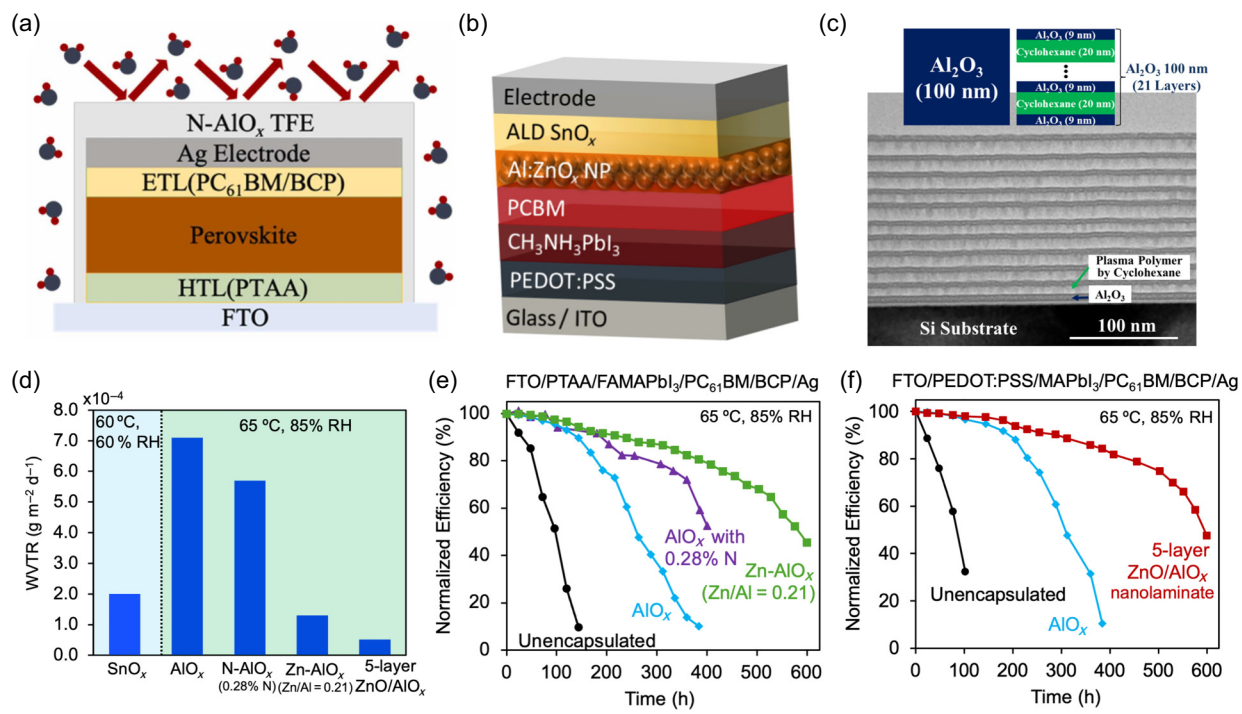


FIG. 4. Gas-diffusion barriers deposited by AP-SALD (a) on a complete device stack and (b) as electron-transporting SnO_x in the device stack. Adapted with permission from (a) Ref. [131], Copyright 2024, Elsevier and (b) Ref. [57], Copyright 2018, American Chemical Society. (c) A cross-section SEM image of a 21-layer Al_2O_3 /polymer nanolaminate gas-diffusion barrier. The nanolaminate structure disrupts water-vapor permeation pathways and the polymer improves bending resistance. Reprinted with permission from Ref. [139]. Copyright 2020, American Vacuum Society. (d) The WVTRs of some SALD gas-diffusion barriers and (e),(f) reported normalized PCEs of *p-i-n* perovskite solar cells encapsulated with different AP-SALD barriers under accelerated testing conditions (Musselman group). Adapted with permission from Ref. [57], Copyright 2018, American Chemical Society, Ref. [131], Copyright 2024, Elsevier, Ref. [140], Copyright 2023, John Wiley and Sons, and Ref. [141], Copyright 2024, John Wiley and Sons.

degrading the perovskite device [131,140]. This is important, especially because the WVTR of Al_2O_3 tends to improve at higher deposition temperatures [137]. A small reduction in device performance has only been noted if ozone has been used as the oxidant for AP-SALD; no degradation has been seen when H_2O or H_2O_2 have been used [142].

Riedl and co-workers have demonstrated the use of SnO_2 as a barrier coating to improve the stability of perovskite devices and that it could also be integrated into the perovskite device stack by being able to conduct charge carriers (unlike Al_2O_3) [57,143]. The WVTR of AP-SALD SnO_2 grown at 80 °C has been found to be approximately $10^{-4} \text{ g m}^{-2} \text{ day}^{-1}$ when measured in a 60 °C, 60%-relative-humidity environment. Better WVTR values of approximately $10^{-6} \text{ g m}^{-2} \text{ day}^{-1}$ have been achieved in SnO_2 films grown by ALD at 200 °C [132]. Nevertheless, the low-temperature-grown AP-SALD SnO_2 has been sufficient for enabling MAPbI_3 perovskite devices to be stable at 60 °C for over 3000 h by using a combination of Al:ZnO nanoparticles and AP-SALD SnO_2 to encapsulate the perovskite device stack [Fig. 4(b)]. The metal electrode was deposited over the SnO_2 layer [57].

AP-SALD facilitates rapid switching between precursor gas flows to produce nanolaminates. Nanolaminates with Al_2O_3 layers of different densities [144] and carbon contents [145] have been deposited by SALD and provide better barriers by decoupling the defect-induced permeation pathways in the individual layers. SALD has also been used to produce Al_2O_3 -polymer nanolaminates [Fig. 4(c)], which have the added benefit of improved bending resistance [139]. Recently, AP-SALD has been used to deposit a five-layer 60-nm-thick ZnO/AlO_x nanolaminate gas-diffusion barrier onto complete perovskite solar cell stacks. It has provided a WVTR of $5.1 \times 10^{-5} \text{ g m}^{-2} \text{ day}^{-1}$ and an order-of-magnitude improvement in the device lifetime under accelerated testing conditions (65 °C and 85% relative humidity) [141]. The WVTRs and device-stability improvements from several of these reports are summarized in Figs. 4(d)–4(f).

Nfinite Nanotechnology Inc., a startup from the University of Waterloo, is commercializing roll-to-roll AP-SALD systems for encapsulation. While their focus is on vapor-barrier coatings for sustainable packaging, these encapsulation layers have broad applicability for the PV, LED, and electronic applications discussed here.

C. Energy harvesting and self-powered devices

1. Energy harvesters

The Internet of Things (IoT) constitutes billions of interconnected devices and is forecast to grow to trillions soon [146]. This will necessitate distributed power generation

to meet the associated energy demand. A range of energy-harvesting devices are being developed, including piezoelectric, triboelectric, thermoelectric, electromagnetic, and indoor PV energy harvesters. In a recently published roadmap, low cost and manufacturability at scale were two of the important criteria identified for energy harvesters [146] and AP-SALD is advantageous in both respects. Furthermore, the roll-to-roll compatibility of AP-SALD is advantageous for flexible devices and integration into wearables.

To date, AP-SALD has not been extensively used in the field of energy harvesting; however, there are clear opportunities. Following from Sec. III B, there is the potential for AP-SALD films to be used for indoor photovoltaics (IPVs) and, indeed, AP-SALD has been used to deposit ZnO onto BiOI for a recent demonstration of 4%-efficient IPVs [147]. The thickness control, potential for doping, and modest deposition temperatures of AP-SALD are promising for the deposition of piezoelectric materials such as ZnO , ZrO_2 , and HfO_2 for piezoelectric nanogenerators [148]. Conventional ALD has been used to infiltrate inorganic compounds into polymers (sequential infiltration synthesis) to modify their dielectric and electrical properties for triboelectric nanogenerators [149,150] and to coat metal-oxide films, particularly ZnO , onto a variety of substrates, including plastics and textiles, for flexible and wearable thermoelectric energy harvesters [151,152]. Some of the reported thermoelectric films have been several hundred nanometers thick; the rapid nature of AP-SALD would facilitate manufacturing of these thicker layers and is beneficial for thermally sensitive polymer and textile substrates.

Electromagnetic energy can be wirelessly transmitted to IoT devices and harvested from the surrounding environment to provide power for periodic operation of IoT devices. Radio-frequency (rf) energy can be harvested using a “rectenna,” which includes an antenna and a rectifier circuit that converts the ac signal to dc power. The integration of AP-SALD films into rectifying Schottky diodes and transistors has received little attention to date; however, recent work on AP-SALD of quantum tunneling metal-insulator-metal (MIM) diodes is promising in this regard. MIM diodes consist of a thin insulator layer sandwiched between metal contacts with different work functions to produce an asymmetric tunneling barrier, which results in preferential conduction in one direction, i.e., rectification. Notably, the quantum tunneling mechanism can operate at zero bias for low power consumption and rapid tunneling rates make these diodes promising for rectification of high-frequency signals, which could extend wireless energy transmission or harvesting beyond the rf into the terahertz regime (IR and optical). Alshehri *et al.* first demonstrated the use of an AP-SALD system to make MIM diodes with a 6-nm-thick Al_2O_3 insulating layer in 2019 [153]. Then, in 2021, the same authors leveraged

the ability of an AP-SALD system to operate in a spatially varying CVD mode, whereby the deposition rate varies across the substrate, to deposit Al_2O_3 films with nanoscale-thickness gradients for combinatorial study of a Pt/ Al_2O_3 /Al MIM diode. Diodes with 18 different Al_2O_3 thicknesses have been studied and approximately 7.0 nm has been identified as optimum [154].

More recently, Alshehri *et al.* have used this combinatorial approach to study dual-insulator metal-insulator-insulator-metal (MIIM) diodes [155]. The use of two insulators allows the introduction of greater asymmetry. By depositing ZnO and Al_2O_3 films with orthogonal thickness gradients using an AP-SALD system, they have constructed diodes with 414 different ZnO/ Al_2O_3 film-thickness combinations on a single substrate [Figs. 5(a) and 5(b)] and demonstrated optimized diode performance when a trap-assisted tunneling mechanism has been dominant for insulator thicknesses of 3.4–4.4 nm (ZnO) and 7.4 nm (Al_2O_3). The use of AP-SALD in MIIM diodes is promising for implementation in large-area and flexible energy-harvesting surfaces. The process reliability has also

been encouraging; the conformal pinhole-free nature of the AP-SALD films has resulted in functioning diodes over several square inches, despite the very thin nature of the oxide films. These energy-harvesting technologies can be combined with energy-storage devices, where AP-SALD again has the potential to play an important role, as will be discussed in Sec. IV.

2. Self-powered devices

AP-SALD also has the potential to enable self-powered devices. Self-powered photodetectors [157] and gas sensors [158] have used conventional ALD films. The speed and scalability of AP-SALD could be advantageous in these applications. In one example, Mistry *et al.* have fabricated self-actuating frequency-shift cantilever gas sensors using AP-SALD [156]. They made a microcantilever from an AP-SALD ZnO film, which served as both the structural and gas-sensing receptor layer [Fig. 5(c)]. The 200-nm-thick ZnO cantilever layer was an order of magnitude thinner than conventional microcantilever sensors, which

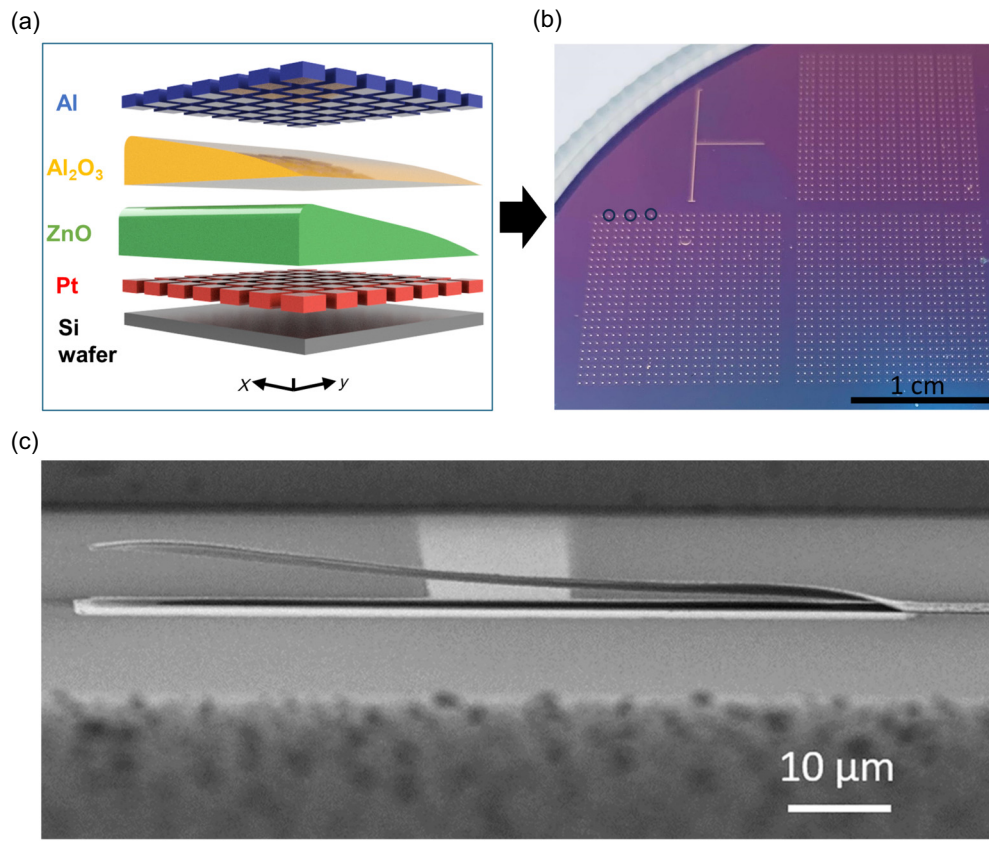


FIG. 5. Applications of AP-SALD for energy harvesting and gas sensing. (a),(b) The combinatorial MIIM device architecture produced using thickness-gradient Al_2O_3 and ZnO films deposited using an AP-SALD system. A schematic (a) and photograph (b) showing a portion of the 414 devices on a wafer, each with a different combination of insulator layer thicknesses. Each device (black circles in left) had an active area of $10 \mu\text{m} \times 10 \mu\text{m}$. Reproduced under the terms of the CC-BY license from Ref. [155]. Copyright 2024, The Authors. (c) A SEM image of a 200-nm-thick self-actuating ZnO cantilever gas sensor fabricated by AP-SALD. Reprinted with permission from Ref. [156]. Copyright 2022, American Chemical Society.

reduced the mass of the cantilever and made it more sensitive to gas-adsorption mass changes. Because of its reduced size, the ZnO cantilever was also self-actuated at its resonance frequency by mechanical-thermal noise from the surrounding gas, i.e., unlike traditional cantilevers, it did not need piezoelectric or electrostatic actuation. While an external power input would still be needed for signal readout, this is a promising step toward self-powered gas sensors. Notably, the AP-SALD process provided conformal pinhole-free ZnO that enabled structurally robust cantilevers. AP-SALD was also fast: deposition of the 200-nm ZnO layer may be prohibitively long using conventional ALD, whereas only 15 min was required to deposit the ZnO on photoresist using AP-SALD.

More recently, ZnO SALD thin films on top of Si cantilevers have been used as sacrificial layers to form cantilevers sensitized with ZIF-8 (a type of metal-organic framework) by reacting the ZnO films with vapors of the ligand. The resulting sensors showed 2 orders of magnitude more sensitivity than the cantilevers sensitized with ZnO [159]. In this case, in addition to a high deposition rate, SALD is appealing as different cantilevers could be coated with different oxide sacrificial layers due to the possibility of performing localized deposition with SALD [160].

D. Other energy applications

1. Solar fuels

Photoelectrochemical cells are devices that harvest sunlight to carry out redox reactions, such as reducing H⁺ (aq) to produce green hydrogen [161]. Recently, the photoelectrochemical field has been incorporating the learnings from the PV field, such as utilizing multilayer device stacks to improve charge separation and protecting the light harvester in a photoelectrode from degradation by the electrolyte [6,92,162]. Hoye and colleagues have recently demonstrated this with BiOI photocathodes, which used the oxide-based device architecture developed for PVs, including the use of AP-SALD to deposit ZnO to completely cover the textured surface of BiOI [92,113]. The combination of using oxide charge-transport layers, along with a graphite epoxy encapsulant, led to photoelectrodes with improved stability from a couple of minutes (BiOI directly in the electrolyte) to a couple of months [92]. ALD has attracted growing interest in the solar-fuel field, not just for photoelectrochemical cells but also in photocatalysis and PV electrolysis [163]. More effort should be made to utilize the advantages of SALD in the solar-fuels area.

2. Light-emitting diodes (LEDs)

LEDs are the inverse of PVs and involve charge injection at forward bias leading to radiative recombination and electroluminescence. While inorganic III-V materials

are now mainstream for the white-LED market, emerging thin-film emitters (e.g., organic materials and quantum dots) are gaining commercial importance for the next generation of displays, especially flexible displays. These include polymer LEDs, two-dimensional (2D) materials, and halide perovskite LEDs, the latter of which provide some of the sharpest electroluminescence peaks, which is important for realizing displays with a wider color gamut [164,165]. AP-SALD can play a role by depositing oxide charge-transport layers or charge injectors with tunable charge-injection levels, encapsulation of the LED device stack, or depositing materials that can reduce interface recombination. For example, the authors have used Mg:ZnO to raise the electron-injection level, which lowered the turn-on voltage for blue-polymer LEDs [166]. As another example, the authors have used AP-SALD to grow Mg:ZnO directly onto perovskite emitters. The Mg:ZnO also presents a larger barrier to holes injected into the perovskite emitter than fluorenes, thus avoiding parasitic emission from the charge-transport layer, leading to an early demonstration of color-pure emission from halide perovskite emitters [166]. Recently, the application of AP-SALD films has been extended to LEDs based on 2D transition-metal dichalcogenides. A ZnO electron-transport layer has been deposited directly on top of a WS₂ emissive layer at temperatures ranging from 75 to 150 °C [167]. Thus, the advantages discussed in the Sec. III B for AP-SALD also apply to LEDs and further work should be implemented to explore these opportunities.

IV. ELECTROCHEMICAL ENERGY-STORAGE-DEVICE APPLICATIONS

The most common electrochemical storage devices are batteries and supercapacitors. In both cases, ALD has been extensively explored, given its ability to conformally coat complex and porous surfaces with sub-nanometer-level precision. ALD coatings are particularly appealing for batteries, since they can act as an artificial solid-electrolyte interface (SEI) to minimize electrode degradation, suppress dendrite formation, or allow operation at high voltages [168].

While there is already abundant literature on the use of ALD for batteries and supercapacitors, there are only a few works so far exploring the use of SALD for electrochemical energy-storage devices, all of them dealing with batteries. One of the main areas of study has been to assess the capability of SALD to conformally coat porous materials and the impact on the deposition rate and conformality, given that rapid film deposition is a key advantage of AP-SALD. In the first report on the use of SALD for batteries, Sharma *et al.* have explored the deposition of thin Al₂O₃ coatings on Li_{0.20}Mn_{0.54}Ni_{0.13}Co_{0.13}O₂ electrodes, resulting in enhanced capacity retention as compared with uncoated electrodes [169]. In a second work from the same

team, Yersack *et al.* have optimized their reactor to achieve higher deposition rates by adding spacers between the precursor modules and the adjacent extraction modules. The uniformity of the coatings improved for longer exposure times but became worse for increasing aspect-ratio substrates [170].

Since these initial empirical demonstrations that SALD can effectively coat complex porous battery substrates, Moitzheim *et al.* have taken a more analytical approach, in which they have developed a model for the diffusion of precursors through micropillar substrates to calculate the minimal exposure time required to achieve conformal deposition [171]. The model shows that for extreme aspect ratios (i.e., the height-to-diameter ratio of the micropillars) of 200 and reaction probabilities, β , of $\beta = 1$ down to $\beta = 0.001$, it would take up to approximately 40 min to

deposit a 100-nm-thick coating, which is a feasible time frame. This model has been reasonably accurate, with the actual exposure time required to conformally deposit Cl-doped TiO_2 onto TiN-coated Si micropillars being only 5 times larger than the minimum theoretical value (Fig. 6). Reducing the precursor exposure time (i.e., faster deposition) closer to the theoretical value has resulted in non-conformal films but this has had a negligible effect on the performance in batteries. This is a promising step forward in the development of nanostructured thin-film batteries, which could have capacities exceeding state-of-the-art coin-cell batteries [171].

In a more recent work, Li *et al.* have used computational-fluid-dynamics (CFD) simulations with multilevel pore-scale diffusion to study the potential of SALD to coat porous battery electrodes [172]. The results

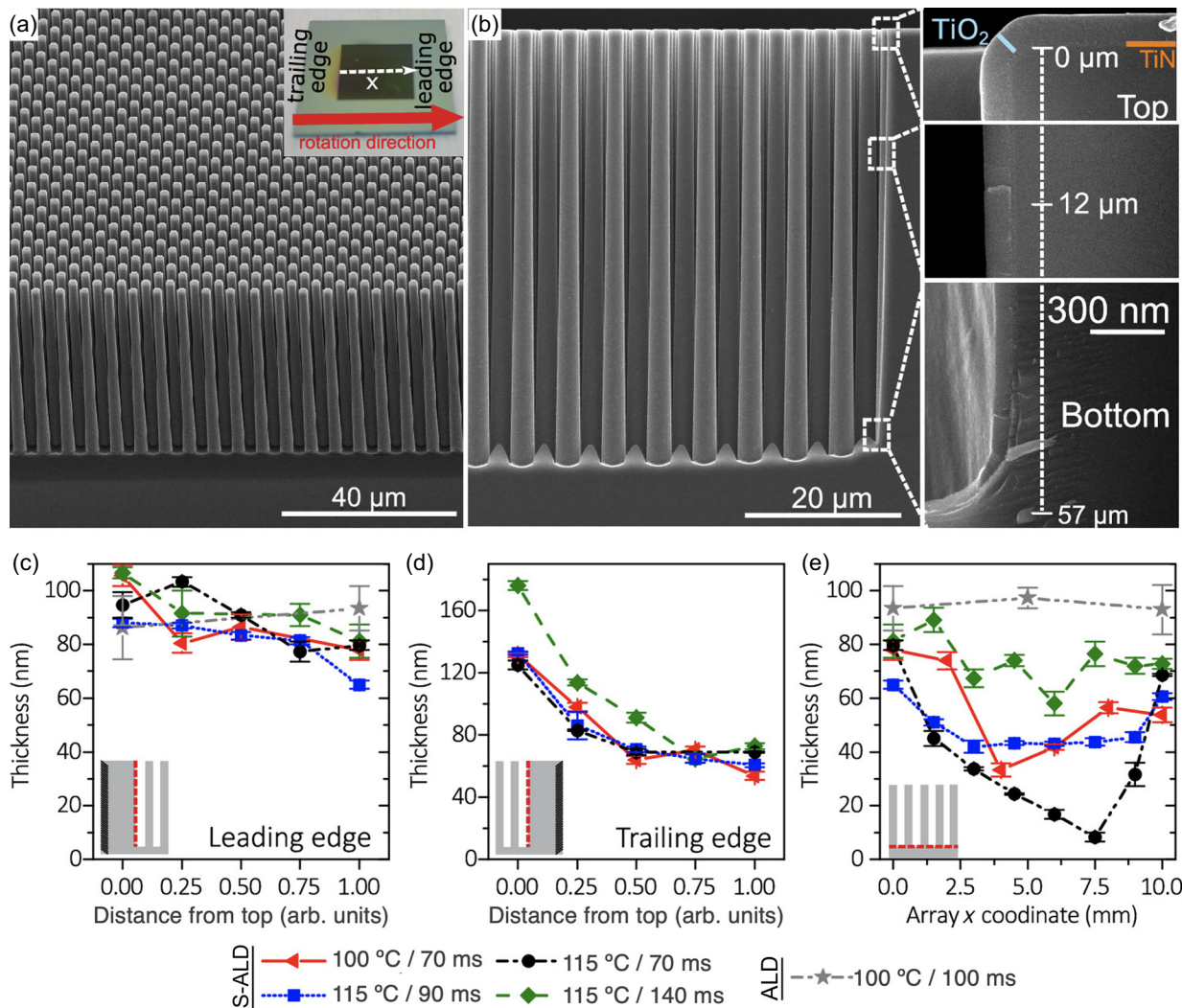


FIG. 6. (a),(b) Optical and SEM images of TiN-coated Si micropillar arrays used to study the conformality of SALD Cl-doped amorphous TiO_2 films, which have been grown over these arrays. A photograph of the sample in inset in (a). (c)–(e) The thicknesses obtained from SEM images of different points of the arrays as a function of the deposition parameters (temperature and exposure time). Reprinted with permission from Ref. [171]. Copyright 2019, American Chemical Society.

show that slightly reduced operating pressures (0.1 versus 0.01 or 1 atm) are optimum for maximizing the deposition rate, and that the pore size, precursor concentration and flow rate, and temperature also play key roles [172].

The effectiveness of SALD coatings on the stability of batteries under high-temperature operation has been the focus of several works. Hsieh *et al.* have explored the deposition of TiO₂ coatings on Ni-rich electrode materials for high-temperature operation [173]. The parameters evaluated were the deposition temperature (120–180 °C) and the substrate speed (2–40 mm s⁻¹) [173]. The coated substrates showed improved stability due to the reduction of parasitic reactions between the electrode and the electrolyte, as demonstrated by electrochemical impedance spectroscopy (EIS). The EIS results also showed that the SALD coatings reduced charge-transfer resistance. Protected electrodes fabricated at substrate speeds up to 2.4 m min⁻¹ sustained operation at 55 °C under a high-voltage window (3.0–4.35 V), showing improved specific capacity, superior rate capability, excellent cyclability, and ultrahigh Coulombic efficiency retention of up to 99.7% [173]. In another study, Panda *et al.* have demonstrated that Li-rich electrodes coated with TiO₂ can be cycled under an aggressive voltage window (2.0–4.8 V) at 60 °C, showing a high stability and a decrease in overpotential [174]. The coating again prevented side reactions between the electrode and the electrolyte and facilitated charge transfer. The coating was deposited at rates above 1.2 m min⁻¹ [174]. Similar results have been obtained by the same group on cells in which both electrodes and the separator were protected with a SALD TiO₂ layer [175]. The fabricated cells did not show any appreciable volume expansion when operated at 55 °C [175]. Lee *et al.* have shown that a 5-nm-thick SALD Al₂O₃ coating on commercial battery separators (Celgar) improves the mechanical properties and thermal stability. After 100 cycles at 1 °C and 80 °C, the batteries incorporating the coated separator showed a capacity retention of 79.5% versus 70% for an uncoated separator [176].

Finally, the chemistry of the ALD process can have an important impact on battery performance. Moitzheim *et al.* have shown that the amount of Cl doping present in amorphous TiO₂ films deposited using TiCl₄ and water vapor in a rotary SALD reactor had a direct impact on the battery efficiency, and this will need further study [177].

The appealing prospects of using SALD to improve the reliability and performance of solid-state batteries has led to this application area being a core priority for several companies commercializing SALD systems. These include SparkNano [178], SALD B.V. [179,180], and Beneq [53,180], who have publicly indicated that they see value in the use of their systems to develop coatings for the components in batteries (e.g., powders used for cathodes and anodes, as well as the SEI) to improve energy density, reliability, and safety [178–180]. Furthermore, all three companies have developed roll-to-roll SALD

systems [179–181] that could contribute to faster and more cost-effective manufacturing of next-generation battery materials. Forge Nano have also developed a spatial ALD reactor for coating particles for battery cathodes and these systems have been used for high-volume cathode production [182].

V. APPLICATIONS IN ELECTRONICS

A. Transparent conducting materials

A wide range of devices, from touch screens to PVs, require transparent conducting materials (TCMs). TCMs include oxides (i.e., TCOs, as well as nonoxide and metallic materials). In general, TCMs should have high transmittance in the operational wavelength range, along with a low sheet resistance, but the precise figures of merit depend on the target application [183]. Other important factors for TCMs are the haze factor, flexibility, processability by low-cost scalable approaches, the use of nontoxic noncritical materials, and chemical stability against other materials in the device with which the TCM is in contact, the processing conditions used, and the ambient environment. ITO (tin-doped indium oxide) and FTO (fluorine-doped tin oxide) are currently the most industrially used TCMs, due to their low sheet resistance, high transmittance, and maturity. However, these TCMs have important limitations, including the scarcity and high cost of In, as well as the high deposition temperatures required for fabricating FTOs (limiting their use for flexible polymer substrates), thus motivating the search for alternative TCMs.

SALD has been explored for depositing TCMs rapidly with low cost. Indeed, early work on SALD TCMs has focused on undoped ZnO [184]. Illiberi *et al.* have shown that AP-SALD ZnO films can be conductive (*n*-type, 4 mΩ cm resistivity for 250-nm thickness) or insulating, depending on the partial pressure of diethylzinc (DEZ) used. In their study, the films were deposited at temperatures between 75 and 250 °C and had good crystallinity, with high transmittance (~85%) in the visible range [185].

In a later work from the same group, it has been demonstrated that Al-doped ZnO (AZO) thin films can be deposited at rates of 0.2 nm s⁻¹ with controlled stoichiometry by co-injecting DEZ and trimethyl aluminum (TMA) in the same deposition region of their rotary SALD system and controlling the TMA flow rate to the reactor or the TMA exposure time to the substrate [34]. AZO with a transmittance of 85% and a low resistivity of 2 mΩ cm could be achieved for films with approximately 200 nm thickness, deposited at 200 °C with around an 8 at.% Al. The carrier concentration reached 10²⁰ cm⁻³ and the mobility 5 cm² V⁻¹ s⁻¹. The *c*-axis preferred orientation of ZnO was accentuated upon Al doping until 40 at.% Al content, beyond which the films became amorphous. Nguyen *et al.* have used a close-proximity AP-SALD system to

deposit ZnO and AZO films, using DEZ and TMA as precursors [186]. The ZnO films had a high transmittance of 80–90% in the visible wavelength range, with a band gap between 3.30 and 3.55 eV, for increasing deposition temperatures (100–220 °C). For AZO, the optimal Al content was only 1.19 at.% and this was difficult to reproducibly control through co-doping. Therefore, instead of continuously mixing the TMA precursor with the DEZ vapors, TMA was mixed into the metal-precursor gas stream as pulses. The films were again grown at 200 °C, and the minimum resistivity was 5.57 mΩ cm (4.25×10^{20} cm⁻³ carrier concentration, 2.6 cm² V⁻¹ s⁻¹ mobility). The texture of the films evolved from (002) for ZnO to (100) for AZO.

However, these AP-SALD AZO films have mobilities that are much lower than AZO films deposited using high-vacuum techniques, such as pulsed laser deposition (PLD) or sputtering. A parameter that strongly affects the mobility of ZnO thin films is the oxygen partial pressure. Nguyen *et al.* have reasoned that the low mobility of SALD AZO films is due to oxygen being trapped at grain boundaries when the films are grown under ambient conditions, requiring charge-carrier tunneling between grains [187]. These trapped oxygen species can be partially eliminated through illumination with UV light with mild heating at 200 °C. If the films are exposed to air at high temperature, oxygen is again absorbed [184]. Absorption of oxygen can be prevented by covering the AZO with an Al₂O₃ layer (the same approach has been used by Illiberi *et al.* for ZnO films deposited by CVD) [185].

Interestingly, a work by Hsu *et al.* has reported high mobilities in the range of 20–50 cm² V⁻¹ s⁻¹ from AP-SALD AZO, obtaining a resistivity of 0.35 mΩ cm for an Al-doping level of approximately 1 at.% [188]. While this seems to deviate from the observations made above about ambient-processed AZO, it is noted that the undoped ZnO films have a surprisingly high reported mobility of 48 cm² V⁻¹ s⁻¹, despite the grain size being only <25 nm and the film thickness only being 60 nm. The same DEZ and TMA precursors have been used in this work as in other works on AZO [188].

It is emphasized that while several works [187–190] have reported AP-SALD AZO, there is inconsistency in the optimal doping level of Al, texture evolution, and resistivity values. Conductivity values comparable to those of ITO have been reported in these works but a systematic investigation is necessary to assess the parameters having the most impact on the TCM figure of merit and reproducibility [e.g., dimethylaluminumisopropoxide (DMAI) seems to be more efficient for doping than TMA]. Finally, the deposition of indium-doped ZnO has been evaluated by Illiberi *et al.* and the resistivity obtained (3 mΩ cm) was similar to that of optimized ZnO and AZO films [43].

Tin oxides, SnO₂ (*n*-type) and SnO (*p*-type), have also been deposited by SALD (see Table I). Nguyen *et al.* have

used tin acetylacetone [Sn(acac)₂] and water to deposit 321.5-nm-thick amorphous SnO_x films at 270 °C, with a surprisingly low resistivity of 7 mΩ cm (8×10^{19} cm⁻³ carrier concentration and 11.2 cm² V⁻¹ s⁻¹ mobility) [54]. While Sn(acac)₂ does not react with H₂O in t-ALD, the presence of oxygen in the ambient for AP-SALD allows the formation of SnO_x films. The deposition of *p*-type SnO has been reported by Mameli *et al.*, using a new liquid precursor, tin(II)-bis(tert-amyloxide) [Sn(TAA)₂] and H₂O [56]. The deposition rates were 5–19 times higher than those of previously reported ALD processes for SnO. Mobility values up to 0.4 cm² V⁻¹ s⁻¹ were obtained when the films were implemented in TFTs.

Another interesting semitransparent *p*-type oxide is Cu₂O. Muñoz-Rojas *et al.* have reported AP-SALD Cu₂O with 100 Ω cm resistivity (150-nm-thick films; approximately 10¹⁶ cm⁻³ carrier concentration, 5.3 cm² V⁻¹ s⁻¹ mobility), using Cu(hfac)(tmvs) and H₂O as the precursors and a deposition temperature of 225 °C [61]. By changing the metal precursor to copper(I) hexafluoro-2,4-pentanedionate cyclooctadiene complex [Cu(hfac)(cod)], Sekkat *et al.* have improved the mobility to 92 cm² V⁻¹ s⁻¹ (close to the values reported for Cu₂O single crystals) but have obtained similar resistivity values (64–160 Ω cm; 70-nm-thick films) [59]. The key to the increased mobility is a low defect concentration, as deduced from Raman spectroscopy. By adding oxygen during the deposition, the same team has obtained Cu₂O with very low resistivity values of 0.4 Ω cm [191]. By combining Raman spectroscopy, photoluminescence, and positron-annihilation spectroscopy, it has been shown that increasing the oxygen concentration results in a decrease in oxygen vacancies, yielding increased carrier concentration with still very high mobility values. In addition, the carrier concentration and mobility of the films can be tuned by varying the concentration of oxygen used (Fig. 7) [191].

Finally, metallic nanowire networks are being widely explored as alternative TCMs to ITO, due to their high transmittance (both visible and IR), conductivity, and flexibility. In addition, metallic nanowires can be fabricated by scalable low-cost-solution approaches [191]. Given the high electronic conductivity of Ag and Cu, these have been the most used for nanowires so far. Despite their advantages, metallic nanowires present thermal, electrical, and chemical instabilities. These can be prevented by depositing a thin transparent oxide layer that blocks atomic diffusion and prevents reaction of the nanowires with the environment [192].

ALD, with its intrinsic low-temperature operation, high deposition rate, and conformality, has been proposed as a suitable technique to protect Ag nanowires (NWs) with a thin conformal coating of Al:ZnO [193]. Given that SALD produces films with properties similar to those of ALD, Muñoz-Rojas's and Bellet's teams at LMGP have conducted several studies evaluating the use of SALD to

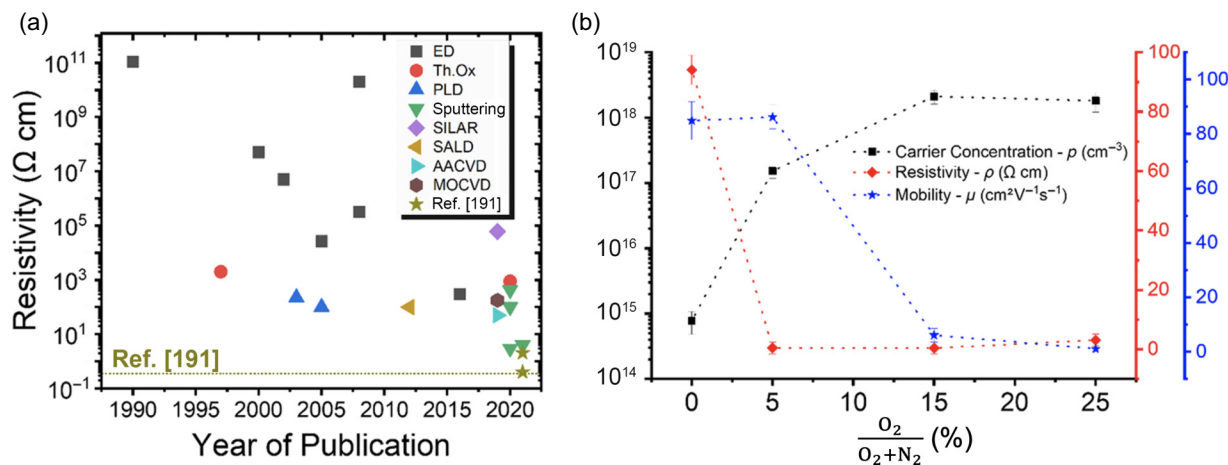


FIG. 7. (a) The resistivity values of Cu_2O thin films deposited at different temperatures and by different techniques. Th.Ox. = thermally oxidized. (b) The impact of the O content during Cu_2O SALD deposition on film transport properties. Reproduced under the terms of the CC-BY license from Ref. [191]. Copyright 2022, The Authors.

coat metallic nanowire networks with oxide films, focusing especially on the stability and the optical and electronic properties. So far, Ag nanowire networks have been combined with ZnO [194], Al_2O_3 [195,196], AZO [197], TiO_2 [198], SnO_2 [199], $\text{ZnO}/\text{Al}_2\text{O}_3$ bilayers [200], and MgO [51]. In all cases apart from TiO_2 (deposited from TiCl_4 and H_2O), the composites have been more stable than the bare networks. The evolution of the stability with the oxide thickness is oxide dependent and needs to be optimized. For example, composite electrodes of silver nanowires and SnO_2 have been used as electrodes for electrochromic devices, while electrodes made with ZnO have degraded during the fabrication of the devices [51]. Al_2O_3 coatings have also proved to be very efficient to obtain robust composite electrodes with Cu nanowires [201].

B. Low-loss electronics

1. Recent developments

Devices for digital processing, memory storage, and computing critically underpin modern society and industry but, equally, need to be developed with greater capacity, functionality, and reduced energy consumption and loss [202]. High-performance electronics benefit from epitaxial growth, which give rise to improved charge-carrier mobilities, and reduced defect density in the bulk and at interfaces. But epitaxial oxides are typically grown at high temperatures $>500^\circ\text{C}$, with high vacuum ($\ll 1 \text{ mbar}$ pressure) [203].

High temperature and vacuum are necessary to achieve a high surface diffusivity, a high mean free path, and sufficient energy for high-crystallinity films. These restrictions severely limit the throughput of manufacturing and how low the capital intensity could be. Given these limitations, there is substantial work in the field to develop routes

to achieve epitaxial oxides at lower temperatures (with a lower CO_2eq footprint) and lower capital intensity.

In situ epitaxy, where epitaxial growth is achieved without postannealing, has been achieved using conventional ALD. However, this has only been reported thus far mainly for binary oxides (e.g., ZnO , Co_3O_4 , and CeO_2) at deposition temperatures exceeding 200°C [204–206]. Very recently, Sønsteby *et al.* have extended this to ternary oxides (LaNiO_3) at deposition temperatures as low as 225°C , achieving resistivities as low as $100 \mu\Omega \text{ cm}$ [207]. However, these systems are still limited by the need for vacuum batch-based processing.

Sun *et al.* have recently shown that AP-SALD can produce epitaxial oxide perovskites (WO_3), grown under ambient conditions [208]. Furthermore, epitaxial films have been grown at deposition temperatures as low as 350°C on single crystals of SrTiO_3 (STO), LaAlO_3 (LAO), and yttrium aluminium oxide (YAO) substrates. The growth rate at 350°C was 5 nm min^{-1} on all substrates, and the films were uniform and epitaxial over a cm^2 area. Lowering the substrate temperature to 300°C did not result in film growth, while depositing at 375°C resulted in similar films to those deposited at 350°C . The $2\theta-\omega$ scan of 20-nm-thick WO_3 films on STO is shown in Fig. 8(a), along with cross-section transmission electron micrographs in Fig. 8(b). These show a clear epitaxial relationship between the film and substrate, along with the high crystallinity and low defect density of the WO_3 films. The films have reached thicknesses as high as 80 nm before epitaxy has been lost [208].

Other vacuum techniques, such as PLD and sputter deposition, have used temperatures as high as 750°C to obtain epitaxial WO_3 on STO, LAO, and YAO [209,210]. The mechanism for low-temperature epitaxy has been consistent with the highly exothermic reaction between the

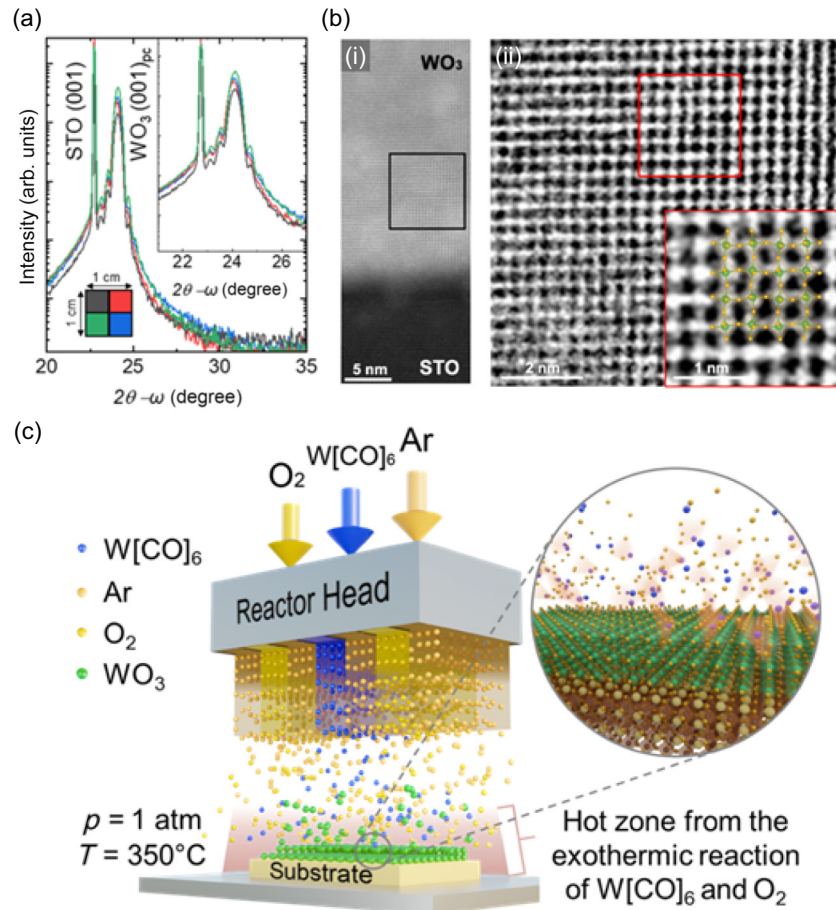


FIG. 8. The growth of epitaxial oxides. (a) A $2\theta - \omega$ scan of four samples of 20-nm-thick WO₃ films prepared on a $1 \times 1 \text{ cm}^2$ single crystal (001) SrTiO₃ (STO) substrate. The inset shows an enlarged region around the WO₃ (001)_{pc} peak for x-ray scans across the four differently artificially colored regions of the film. (b) (i) A cross-section scanning-transmission-electron-microscopy (STEM) image of 40-nm-thick as-deposited WO₃ film on STO. (ii) A magnified view of the region marked with a black square in (i). (c) A schematic of the AP-SCVD growth of WO₃ with an enlarged schematic of the exothermic reaction between W(CO)₆ and O₂ releasing heat in the process and giving additional energy to the deposition process. Reproduced under the terms of the CC-BY license from Ref. [208]. Copyright 2024, The Authors.

W(CO)₆ precursor and oxygen, with the heat of reaction being comparable to the combustion of propane ($\sim 2200 \text{ kJ mol}^{-1}$). The exothermic heat is confined by the 800-μm spacing between the substrate and the reactor head, a situation unique to the AP-SALD reactor [Fig. 8(c)]. That is, in conventional ALD, there is no such confined region for localized heating. Thus, while the temperature of the substrate holder is low, the local heating on the surface in AP-SALD is then sufficient to enable epitaxial growth to occur. Consistent with this proposed explanation, Sun *et al.* have observed a decrease in nonuniform strain by around half when the flow rate of the inert carrier gas for the metal precursor has been halved, indicating higher film quality, due to an increase in local heating. Overall, open-atmosphere epitaxial growth is a very promising avenue for AP-SALD.

2. Perspectives for epitaxy

The realization of epitaxy by AP-SALD represents a promising advancement in thin-film growth. Future research should focus on how to achieve epitaxial films across many different compositions, beyond the first demonstration with WO₃. For example, achieving *in situ* epitaxy in ternary oxide perovskite is highly desirable. This is because of the enormous promise of epitaxial perovskites across a wide range of diverse applications in electronics and energy [211]. To date, this promise is unfulfilled, as conventional epitaxy requires vacuum-based physical vapor deposition (PVD) or chemical vapor deposition (CVD), above approximately 700°C . Thus, current approaches are energy intensive. PLD is the preferred PVD method, as it enables better stoichiometry control than other PVD or CVD methods. However, PLD is area limited and the lasers required are relatively expensive. If

AP-SALD could be used to achieve epitaxial ternary perovskite films at deposition temperatures of 400 °C, as has been demonstrated for WO_3 , this would be game changing, because a large number of electronics and energy applications would be attainable.

Unlike PVD, epitaxy via AP-SALD is achieved simultaneously with chemical reactions on the substrate surface. These reactions are sensitive to a variety of parameters, including the adsorption and desorption dynamics of the precursors, as well as ion migration across the surface. Therefore, the surface chemistry between the precursors and the substrate must be matched for nucleation to occur. In addition, a high-volatility precursor is required to have adequate vapor pressure above the substrate for the reaction to occur. The development of a broader range of precursors that meet these stringent requirements should be a research priority.

To achieve epitaxy by AP-SALD for WO_3 , localized heating in the confined space between the reactor gas manifold and substrate was required, as it compensates for the high temperature typically used in conventional epitaxial PVD and CVD methods. Choosing precursors that undergo exothermic reactions upon oxidation is therefore likely to be important. There is added complexity for ternary-oxide perovskites, in that precise control of the ratios of the two cation precursors and a degree of gas mixing are required to form a homogenous-composition film through its thickness. Simultaneously, the growth rates should be sufficiently low and carefully controlled to ensure epitaxy. Striking this fine balance would benefit from the development of accurate models for precursor mass transport and reactions involved for epitaxial film formation.

Scaling up epitaxy by AP-SALD to the wafer scale is another area that requires attention. Film-thickness uniformity across large areas remains a major technical bottleneck. Factors such as gas flow dynamics, reaction kinetics, and temperature gradients across the substrate must be optimized to ensure consistent film quality. Novel gas injectors should be designed to ensure the uniformity of the partial pressure of the precursor gases across the width of the manifold.

In summary, epitaxy by AP-SALD shows substantial potential as a versatile and scalable deposition method. A number of future directions of research should be addressed, including the limited availability of suitable precursors, achieving *in situ* epitaxy with multicomponent oxides, chemical compatibility of precursors and substrates, and scaling up to wafer-scale production. Addressing these topics will require strong interdisciplinary research efforts. With these efforts, AP-SALD could evolve into a highly efficient industrially viable method for epitaxial growth, opening up new opportunities in the electronics and energy sector.

C. Beyond metal oxides

The vast majority of research into AP-SALD has been on metal oxides, since these are widely used across many energy-device applications and are most compatible with growth in atmospheric conditions. But there are a small but growing number of reports demonstrating the ability to achieve nonoxide compounds by AP-SALD, namely, metals and nitrides.

1. Metals

Although AP-SALD takes places under atmospheric conditions, it has been possible to grow metal films. Currently, efforts in this area are nascent, with a limited set of reports, mostly focused on Ag and Cu [212–217]. The motivation for growing these metal films has been to achieve transparent electrodes, e.g., by sandwiching (5–15)-nm-thick Ag between two layers of MoO_x [217], or for growing metal interconnects for electronics [213]. Achieving metal films, rather than oxides, under atmospheric conditions, requires careful metal-precursor design and selection of growth conditions. In early efforts to grow Ag by AP-SALD, Roozeboom, Poodt, Kessels, and co-workers used a reducing $\text{H}_2\text{-N}_2$ plasma instead of an oxidant in their growth process, using $\text{Ag}(\text{fod})(\text{PEt}_3)$ [triethylphosphine(6,6,7,7,8,8,8-heptafluoro-2,2-dimethyl-3,5-octanedionate) silver(I)] as the precursor [216,217]. From EDX measurements, the F and C contents of the Ag films were below detection limits, indicating that these species from the ligands of the precursor were not significantly left in the film. The O:Ag ratio was 0.3, possibly due to surface oxidation, but the best film resistivity ($18 \mu\Omega \text{ cm}$ for 50-nm-thick films; 100 °C deposition temperature) was still an order of magnitude above that for bulk Ag. This was attributed to islandlike growth of Ag grains that had not completely coalesced [216]. Improved film coverage was obtained on Mo substrates that were pretreated with $\text{H}_2\text{-N}_2$ plasma before Ag deposition to remove the native MoO_x layer, thereby improving wetting by Ag nuclei [217]. Riedl, Devi, and co-workers have reduced the resistivity of AP-SALD Ag films down to $2.7 \mu\Omega \text{ cm}$ at 100 °C deposition temperature [214]. This has been achieved by using a new carbene-based Ag precursor [$\text{Ag}({}^{\text{t}}\text{BuNHC})(\text{hmds})$] [Fig. 9(a)], which enables an approximately $2.5 \times$ growth rate of Ag than $\text{Ag}(\text{fod})(\text{PEt}_3)$ due to improved volatility and reactivity [214,215]. Here again, a reducing H_2 plasma (this time with balance Ar) has been used in the co-reactant channels in place of the oxidant in the AP-SALD reactor gas manifold, while maintaining sizeable N_2 gas curtains [Fig. 9(b)]. Another important factor has been to increase the thickness of the films. 50-nm-thick AP-SALD Ag films grown with [$\text{Ag}({}^{\text{t}}\text{BuNHC})(\text{hmds})$] were just barely conducting due to the islandlike morphology of the Ag grains. Increasing the thickness to 71 nm (1200 ALD cycles; $0.059 \text{ nm per cycle}$) led to the best resistivity

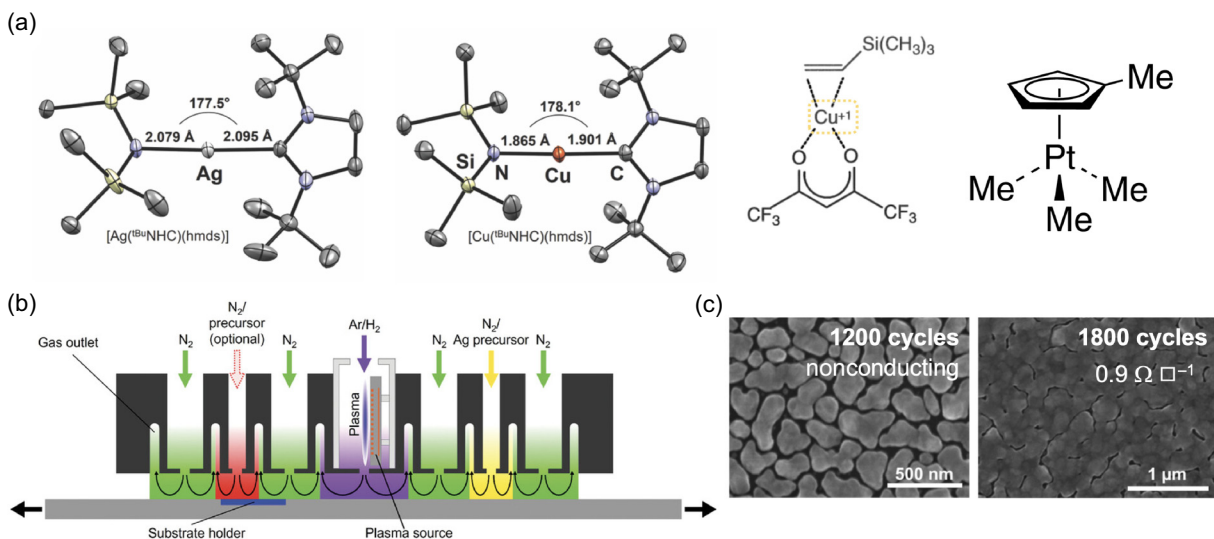
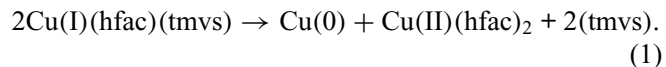


FIG. 9. The growth of nonoxide materials by spatial ALD. (a) The organometallic precursors used to grow Ag, Cu, and Pt. Left to right: 1,3-di-*tert*-butyl-imidazolin-2-ylidene silver(I) 1,1,1-trimethyl-*N*-(trimethylsilyl)silanaminide [$[Ag(^{t}BuNHC})(hmds)$], 1,3-di-*tert*-butyl-imidazolin-2-ylidene) copper(I) bis(trimethylsilyl)amide [$[Cu(^{t}BuNHC})(hmds)$], Cu(1,1,1,5,5-hexafluoroacetylacetone)(vinyltrimethylsilane) ($[Cu(hfac)(tmvs)]$, or Cupraselect®), trimethyl(methylcyclopentadienyl)platinum(IV) ($MeCpPtMe_3$). [$[Ag(^{t}BuNHC})(hmds)$] and [$[Cu(^{t}BuNHC})(hmds)$] reproduced with permission from Ref. [212]. Copyright 2020, Royal Society of Chemistry. [$[Cu(hfac)(tmvs)]$] reproduced with permission from Ref. [213]. Copyright 2023, Elsevier. (b) A schematic of an AP-SALD gas manifold reconfigured for Ag deposition using $[Ag(^{t}BuNHC})(hmds)$. (c) SEM images of AP-SALD Ag films deposited for 1200 (left) and 1800 (right) cycles. Increasing the thickness leads to percolating films, resulting in a change from nonconducting to conducting films, with a sheet resistance of $0.9 \Omega \square^{-1}$. Part (b) reproduced under the terms of the CC-BY license from Ref. [214]. Copyright 2022, The Authors. Part (c) reproduced with permission from Ref. [215]. Copyright 2018, John Wiley and Sons.

of $2.7 \mu\Omega \text{ cm}$ due to grain coalescence and the formation of conductive percolation paths [214].

Riedl, Devi, and co-workers have also modified their precursor to obtain $[Cu(^{t}BuNHC})(hmds)$ for the deposition of Cu films by AP-SALD, again using the same reactor layout, shown in Fig. 9(b) [212]. This carbene-stabilized precursor is shown in Fig. 9(a) and again benefits from suitable volatility, reactivity, and thermal stability. Compared to the Ag precursor, however, the N—Cu—C bonds are shorter and more stable, leading to lower reactivity, and therefore the growth per cycle ($0.023 \text{ nm per cycle}$) being less than half that of the Ag precursor [212]. Cu films with a resistivity of $29 \mu\Omega \text{ cm}$ were obtained after 6000 ALD cycles, compared to a bulk resistivity of $0.168 \mu\Omega \text{ cm}$. Scanning-electron-microscopy (SEM) images showed that pinholes remained in these films, despite there being conductive percolation paths [212]. Sekkat *et al.* have achieved Cu films with lower pinhole density and lower resistivity down to $3.7 \mu\Omega \text{ cm}$ using $[Cu(hfac)(tmvs)]$ as the precursor [Fig. 9(a)] [213]. In contrast to the other Ag and Cu precursors, $[Cu(hfac)(tmvs)]$ forms Cu through disproportionation, following [213]



This time, rather than using an H_2 -containing plasma, the SALD gas manifold had thick curtains of N_2 gas to prevent air ingress, ensuring that $[Cu(hfac)(tmvs)]$ disproportionated rather than forming Cu_2O or CuO . Cu films could be formed at temperatures as low as 160°C and it was at the lowest deposition temperature that the lowest resistivity was obtained. The increase in resistivity with the deposition temperature was attributed to grain coarsening and a reduction in conductive percolation paths [213].

Pt has also been grown in a fluidized-bed spatial ALD reactor [218]. In this case, the trimethyl(methylcyclopentadienyl)platinum(IV) ($MeCpPtMe_3$; Fig. 9(a)) metal precursor was reacted with oxygen from air to form Pt nanoparticles. $MeCpPtMe_3$ is a very widely used precursor in the ALD growth of Pt and the metal forms because the ligands are removed through combustion reactions with oxygen, the metal itself being very stable [219].

2. Nitrides

Beyond metals, Roozeboom and co-workers have demonstrated the growth of SiN_x by AP-SALD [220]. This has also been achieved using plasma-enhanced growth, this time using a N_2 plasma. The Si source used was bis(diethylamino)silane (BDEAS), and wide N_2 gas curtains were kept between the Si source and the N_2 plasma to ensure their spatial separation. This design successfully

enabled low O contents in the films, with values down to 4.7 at.% measured by XPS. However, O incorporation into the films increased with increasing deposition temperature, whereas the C contamination decreased due to increased ligand removal. Opposite trends in O and C contamination in the films were also observed in the effects of tuning the N₂ plasma exposure time, in which increasing plasma exposure times resulted in increased O content, while the C content decreased. Roozeboom and co-workers speculated that this was due to the increased O incorporation from the traces present in the N₂ gas and that any O₂ that diffuses into the reactor from the surrounding environment. At a deposition temperature of 200 °C, a growth per cycle of 0.19 nm per cycle was achieved (similar to plasma-enhanced ALD) but the deposition rate (1.52 nm min⁻¹) was at least an order of magnitude higher, but still below the highest values achievable from industry-dominant plasma-enhanced CVD [220]. This successful first demonstration of SiN_x by AP-SALD motivates further efforts at exploring nitrides by this method.

Furthermore, beyond these inorganic materials, a technique analogous to SALD, termed molecular-layer deposition, has been developed for organic thin-film growth [221]. In this technique, the metal precursor and oxidant are replaced by the two co-reactants for forming the organic material, such as trimesoyl chloride and *m*-phenylenediamine for growing polyimide films that are conformal to nanostructured surfaces, such as the fibers for membrane filters [221].

VI. CONCLUSIONS AND OUTLOOK

In conclusion, AP-SALD has proven to be a highly robust system for the fabrication of a wide range of oxide thin films, from amorphous to epitaxial, with properties spanning from insulators through to degenerate conductors. After over a decade of research, AP-SALD is now being used for a broad range of energy and electronics applications, with many instances of improvements over t-ALD or other state-of-the-art methods for growing thin films. For example, the rapid but soft nature of the deposition makes AP-SALD advantageous for depositing films onto thermally sensitive active layers, such as halide perovskite device stacks. At the same time, AP-SALD films maintain the pinhole-free nature of ALD films, as well as their conformality to high-aspect-ratio nanostructured substrates, moisture impermeability, and high mobility. This makes AP-SALD appealing for forming ultrathin layers that mechanically protect device stacks from sputter damage (important for tandem PV applications) or prevent the ingress of moisture, thus improving the ambient stability of PV devices. The high conformality of AP-SALD films is also important for battery applications to coat porous electrodes. At the same time, the properties of AP-SALD films are finely tunable through the composition, deposition

temperature, and oxidant used, enabling optimization of their performance in devices. It is anticipated that this field will push forward on the range of materials and properties achieved by AP-SALD and the applications in which these materials are used, as well as on the commercial use of AP-SALD. Below, perspectives on the future of AP-SALD in energy and electronics are discussed.

A. Perspective for energy applications

AP-SALD is highly appealing for growing overlayers onto perovskite device stacks for fabricating semitransparent solar cells for tandem PV applications. But the potential of AP-SALD goes beyond this. As discussed in Sec. V, AP-SALD can be used to grow TCMs and there is the possibility of directly depositing a TCM onto the perovskite device stack rather than using a protective layer and a sputter-deposited TCM. However, it will be important to achieve high figures of merit using low deposition temperatures (approximately 100 °C) and fabricate sufficiently thick TCMs with low sheet resistance within approximately 2 min to avoid thermally damaging the perovskite device. Realizing this could simplify the manufacture of perovskite top cells for tandem PVs. Furthermore, if AP-SALD can directly deposit oxide layers onto the halide perovskite thin film, this would obviate the need for an expensive organic charge-transport layer and open up opportunities for field-effect (through band bending at the interface) and chemical passivation at this interface. However, more work is needed to understand why depositing AP-SALD oxides onto perovskite films has yielded poorer devices than the inverse (depositing perovskite films onto AP-SALD oxides). Furthermore, there are opportunities to apply AP-SALD overlayers and buffer layers to improve the performance of broader classes of emerging materials for optoelectronics, including organic semiconductors, chalcogenide semiconductors, and emerging nanocrystal materials, not only for PVs, but also photoelectrochemical cells and LEDs using similar device architectures.

The versatility of AP-SALD extends well beyond PV applications, offering numerous opportunities for the fabrication of piezoelectric, triboelectric, and thermoelectric energy-harvesting technologies. It is well known in the literature that piezoelectric characteristics improve with increasing film thickness [148,222,223] and the rapid deposition achievable by AP-SALD makes it highly advantageous over conventional ALD for growing micron-thick piezoelectric films. The initial challenge will be to stabilize the noncentrosymmetric phase of piezoelectric materials. While lead-free piezoelectric oxides, such as ZnO, are stable in the wurtzite phase, materials such as ZrO₂ and HfO₂ exhibit inherent instability in the orthorhombic phase [224]. Additionally, Ga₂O₃ displays piezoelectric properties in the ϵ -polymorph phase [225], which requires optimized deposition conditions. The second challenge concerns the control of structural

and electrical properties. The enhancement of piezoelectric properties is closely linked to the tuning of the structural texture of the material [226,227]. This remains a significant challenge, especially in polycrystalline films. Additionally, controlling electrical properties often requires a doping process that reorganizes the electrical properties. Being an adaptable method, AP-SALD allows integration with plasma, UV techniques, environmental control, dopant incorporation, and combinatorial setups. This makes it a promising technique that can overcome these challenges and optimize the deposition process while maintaining improved piezoelectric qualities.

AP-SALD also has potential for applications in electrochemical energy storage beyond batteries. Fuel cells are particularly important, producing electricity from H₂ or other fuels. Although there are no SALD studies on fuel-cell applications, the surge in research in this field will certainly attract interest from the community to explore the fast SALD approach. Indeed, there are already works describing the deposition of ZrO₂ by SALD [48,62]. These can be used as starting point to deposit yttrium-stabilized zirconia (YSZ), a typical fuel-cell solid electrolyte. The purification and separation of gases, especially H₂, is of key importance as well in this context and specific SALD setups are to be developed for these applications. A recent work by Toldra-Reig *et al.* has presented a proof of concept of a cylindrical SALD reactor to coat ceramic tubular membranes [63].

The combination of AgNWs and SALD oxides can also be exploited in energy applications beyond TCMs. For example, AgNWs/TiO₂ nanocomposites have been used as transparent resistive-switching (RS) devices after an initial intentional partial degradation of the AgNW network [198], while AgNWs/Cu₂O electrodes have shown enhanced performance for the oxygen-evolution reaction (OER) during water electrolysis [228]. Finally, SALD coated AgNW networks are promising low-emissivity coatings [196].

Furthermore, greater efforts should be made to build upon recent demonstrations of growing metal films by AP-SALD. These metal films can be used as the electrodes in optoelectronic devices, which opens up the possibility of fully roll-to-roll processed devices made under ambient conditions (since the metal electrode is currently typically deposited by thermal evaporation under vacuum). Many metals (e.g., Pt or Cu) have higher surface energy [218]. This can be a disadvantage for metal electrodes, since grains will initially form isolated islands and the film needs to exceed a certain thickness to form conducting percolation paths. On the other hand, isolated metal clusters provide high surface-area-to-volume ratios, which could be advantageous for photocatalysis and/or electrocatalysis. Already, SparkNano are commercially exploring the potential of SALD to reduce the amount of Ir catalyst used in proton-exchange membranes for green hydrogen

production by controllably producing thin coatings of this metal [229].

B. Perspective for electronics

Future materials for low-loss electronics include ferroelectrics for ferroelectric field-effect transistors (FeFETs) and ferroelectric capacitors, plus a wide range of oxides for RS for nonvolatile memory, including HfO₂, TiO₂, WO₃ (popular CMOS-compatible materials), and many other oxides. 2D materials are also actively being investigated for 2DFETs [141,146,147] and RS memory [148–150]. All of the aforementioned materials have wide potential for showing artificial neural networks, i.e., for neuromorphic computing [151–153]. If these different functional materials could be made reliably, uniformly, with a high specification of performance requirements (e.g., a high on-off ratio, endurance, and retention, along with low currents), and in a CMOS-compatible fashion, many applications could emerge in across a wide range of areas, including IoT devices, flexible electronics, bioelectronics, and sensing. In this regard, compared to standard CVD and PVD methods, the advantages of AP-SALD are the ability to fabricate films under ambient conditions (vacuum-free), as well as to localize the heat from exothermic reactions, enabling lower growth temperatures, while maintaining high uniformity for large-area film growth.

In terms of binary oxides for RS, there are strong prospects of using AP-SALD for creating these materials in a uniform and reliable way, whether they be crystalline or amorphous. RS is observed in a wide range of binary oxides, such as TiO₂ [230], ZnO [231], NiO [232], Nb₂O₅ [233], WO₃ [234], Cu₂O [235], ZrO₂ [236], and HfO₂ [237]. All of these materials can be made by t-ALD and many such materials have been demonstrated by AP-SALD as well, such as ZnO [36] and ZrO₂ [48,77].

For all RS materials, an important factor for achieving uniform behavior is to control the conductive-filament formation (guiding their location and dimensions) and/or to use an interface switching process, although the latter approach has challenges of state retention. A combination of these two approaches in an amorphous doped HfO₂ thin-film system grown by PVD at 400 °C has shown to be very promising [155]. It should be possible to replicate this combined strategy with AP-SALD and further work is needed to explore this.

With the discovery of HfO₂ [156] and ZrO₂ ferroelectrics [157], and mixtures thereof (i.e., Hf_{1-x}Zr_xO_y [158]), there has been great excitement about the prospect of using these simple (pseudobinary) group-IV-oxide materials for the aforementioned low-loss electronics applications, e.g., in FeFETs. Typically, ALD is used to deposit an amorphous film of the group-IV oxide and rapid thermal annealing is used to crystallize the phase. To date, AP-SALD has not been used to grow

ferroelectric group-IV oxides. For HfO_2 and ZrO_2 , the standard ALD precursors for these films are tetrakis(dimethylamido)-hafnium (TDMA-Hf), tetrakis(ethylmethylamino)-hafnium (TEMA-Hf), and tetrakis(dimethylamido)zirconium (TDMA-Zr), respectively [158–161]. While there are other precursors in the halide and alkoxide form, TDMA and TEMA are preferred due to the higher reactivity and thermal stability [161].

The above-mentioned precursors tend to have low vapor pressures; thus heating would need to be applied to the containers to ensure precursor evaporation. For example, ALD-grown HfO_2 requires the TDMA-Hf and TEMA-Hf to be heated above 70 °C and 105 °C, respectively, to obtain saturation [162]. Therefore, the same precursors can be used by AP-SALD with heating to ensure that sufficient precursor is delivered to the reactor [53]. Another method of delivery for low-vapor-pressure precursor is through ultrasonic nebulization, where the liquid precursor is atomized and subsequently carried to the reactor with the carrier gas. For example, WO_3 thin film has been deposited with low-vapor-pressure precursor BTBMW through nebulization, since the precursor tends to decompose at elevated temperature [163].

Other ferroelectrics from (pseudo)binary oxide have also been reported recently, e.g., Mg-doped ZnO [164] or Bi_2O_3 [238], and so it would be interesting to explore these materials by AP-SALD. In fact, Mg-doped ZnO films have already been grown by AP-SALD (with wide-ranging Mg:Zn ratios) but these films have been used to optimize performance of solar cells (see Sec. III B and Table II) and the ferroelectric properties have not been explored. Bi_2O_3 films have not yet been explored by AP-SALD but have been grown successfully by ALD, e.g., using $\text{Bi}(\text{thd})_3$ (where thd is 2,2,6,6-tetramethyl-3,5-heptanedionato) and H_2O as precursors [238]. There is also strong potential to grow Bi_2O_3 by AP-SALD using these precursors.

A disadvantage of AP-SALD taking place under ambient conditions is that it is challenging to grow films without any O incorporated, and yet chalcogenide and nitride materials are highly promising materials for neuromorphic computing applications [239–241]. The recent successful demonstration of SiN_x growth by AP-SALD with <5 at.% O incorporated [220] is very promising and further efforts should be made to explore the growth of nitrides more broadly with this system. This could be attempted by using a N_2 plasma, as Roozeboom and co-workers have done [220] (or perhaps an NH_3 plasma), and by having sufficiently wide inert gas (N_2 or Ar) curtains around the channels in the gas manifold where reactions take place to minimize air ingress. However, this could be challenging to implement safely with chalcogenides, where there is the risk of H_2S formation when the sulfur source reacts with moisture in air. An alternative approach is to convert films postdeposition (as recently demonstrated with the sulfurization of ALD-grown Bi_2O_3 or MoO_3 [238], or

the formation of nitrides [242]). A challenge with this approach is that it can require high processing temperatures and long reaction times. Otherwise, one could build AP-SALD reactors within an oxygen-free environment (e.g., a glovebox filled with inert gas) and directly form chalcogenides or nitrides.

C. Final points

It is important to note that while the chemistries are in principle the same, the different processing conditions between conventional and spatial ALD can have an impact on the final properties of the materials deposited—even more so when comparing low-pressure ALD to atmospheric SALD. This could prevent the transfer of an ALD process into SALD, as shown in Sec. V A for the case of AP-SALD AZO, in which processing under atmospheric conditions leads to oxygen trapping at grain boundaries, which reduces mobilities [187]. In the case of Cu_2O discussed above, it has also been shown that the oxygen partial pressure can have a significant impact on the final concentration of defects—in particular, oxygen vacancies—dramatically affecting the transport properties of the films [191]. Therefore, the impact of the specific AP-SALD processing conditions on the final properties of the materials needs to be taken into account when developing an industrial process for a particular application.

Another challenge when transferring a process from conventional vacuum-based ALD to atmospheric-pressure SALD is the increased difficulty in handling low-vapor-pressure precursors in the latter. This is because operating at atmospheric pressure rather than vacuum would mean that higher precursor temperatures would be needed to ensure a high partial pressure of the precursor in the gas phase and this can compromise the stability of the precursors during the deposition process. This problem is accentuated by the fact that high deposition rates are targeted in SALD, which requires a high precursor partial pressure to completely saturate the substrate surface oscillating quickly underneath the gas manifold. However, there are now several reports on the use of solid low-volatility precursors for AP-SALD, e.g., to deposit WO_3 and Cu_2O [59,208]. In using low-volatility precursors, it is essential to avoid the deposition of the precursors in the pipes and gas manifold, which could otherwise cause blockages or cross-contamination. This challenge is common to both conventional ALD and AP-SALD and is typically avoided through external heating, e.g., with tapes or by enclosing in an oven.

On the other hand, SALD has the potential to exhibit lower environmental impact than ALD due to the localized heating typically used and the higher deposition rates associated with SALD, with both leading to a decrease in the amount of electrical energy used [243]. Indeed, a recent report by Niazi *et al.* shows that SALD is more

environmentally friendly than ALD (evaluated for the deposition of Al₂O₃ thin films) [244].

An increasing number of ALD companies are developing commercial SALD systems (e.g., Beneq, Leadmicro), with new companies appearing as well (e.g., NanoPrint Innovations Ltd., Nfinite Nanotechnology, SparkNano, and SALD B.V.). Historically, commercial systems (e.g., Levitech and SoLayTec) have focused on well-established, simple binary oxides for the PV industry. Translating the more complex materials developed in the laboratory will require the gap between the low-cost highly customizable laboratory-scale systems versus more expensive commercial systems to be bridged. Doing so could enhance the performance and reduce the cost of manufacturing of emerging devices for clean energy production, energy storage, or nonvolatile memory storage. This review has highlighted several applications in which SALD can provide these potential advantages but little work has been done to date, including on energy harvesters, self-powered devices, and low-loss electronics, among others. Significant opportunities for pioneering research and new startup companies exist in these fields.

ACKNOWLEDGMENTS

R.L.Z.H. thanks UK Research and Innovation for support through a Frontier Grant (Grant No. EP/X029900/1), awarded through the 2021 European Research Council (ERC) Starting Grant scheme, as well as the Engineering and Physical Sciences Research Council for financial support (Grant No. EP/V014498/2). R.L.Z.H. also thanks the Royal Academy of Engineering and the Science and Technology Facilities Council for support through a Senior Research Fellowship (Grant No. RCSRF/2324-18-68). K.P.M. acknowledges a University of Waterloo Endowed Chair in Nanotechnology and the NSERC Discovery Program (Grant No. RGPIN-2023-03548). D.M.-R. acknowledges funding from the Agence nationale de la recherche (ANR, Grant No. ANR-21-CE08-0047). Z.S. and J.L.M.-D. acknowledge support from the Royal Academy of Engineering Chair in Emerging Technologies scheme (Grant No. CIET1819_24) and the ERC Advanced Grant (ADG) EU-H2020-ERC-ADG (Grant No. 882929, “Efficient and Robust Oxide Switching,” EROS).

R.L.Z.H., Z.S., and J.L.M.-D. are, respectively, the Chief Technology Officer, Chief Executive Officer, and Chief Security Officer of NanoPrint Innovations Ltd.

K.P.M. is a co-founder of Nfinite Nanotechnology Inc.

[1] Materials for the energy transition roadmap (available at: <https://www.royce.ac.uk/materials-for-the-energy-transition/>) (accessed February 2, 2024).

- [2] Photovoltaics blooms and spreads, *Nat. Energy* **3**, 437 (2018).
- [3] R. Usiskin, Y. Lu, J. Popovic, M. Law, P. Balaya, Y. S. Hu, and J. Maier, Fundamentals, status and promise of sodium-based batteries, *Nat. Rev. Mater.* **6**, 1020 (2021).
- [4] P. S. Grant, D. Greenwood, K. Pardikar, R. Smith, T. Entwistle, L. A. Middlemiss, G. Murray, S. A. Cussen, M. J. Lain, and M. J. Capener, Roadmap on Li-ion battery manufacturing, *J. Phys. Energy* **4**, 042006 (2022).
- [5] Henry Royce Institute, Materials for the Energy Transition Roadmaps: Materials for Low-Carbon Methods for Generation of Hydrogen and Other Related Energy Carriers and Chemical Feedstocks (2020) (available at: <https://www.royce.ac.uk/materials-for-low-carbon-production-of-hydrogen/>) (accessed February 2, 2024).
- [6] V. Andrei, G. M. Ucoski, C. Pornrungroj, C. Uswachoke, Q. Wang, D. S. Achilleos, H. Kasap, K. P. Sokol, R. A. Jagt, H. Lu, T. Lawson, A. Wagner, S. D. Pike, D. S. Wright, R. L. Z. Hoye, J. L. MacManus-Driscoll, H. J. Joyce, R. H. Friend, and E. Reisner, Floating perovskite-BiVO₄ devices for scalable solar fuel production, *Nature* **608**, 518 (2022).
- [7] I. E. L. Stephens, K. Chan, A. Bagger, S. W. Boettcher, J. Bonin, E. Boutin, A. K. Buckley, R. Buonasanti, E. R. Cave, X. Chang, *et al.*, 2022 roadmap on low temperature electrochemical CO₂ reduction, *J. Phys. Energy* **4**, 042003 (2022).
- [8] Henry Royce Institute, Materials for the Energy Transition Roadmap: Materials for Photovoltaic Systems (2020) (available at: www.royce.ac.uk/content/uploads/2020/09/M4ET-Materials-for-Photovoltaic-Systems-roadmap.pdf) (accessed February 2, 2024).
- [9] M. Chen, M. P. Nijboer, A. Y. Kovalgin, A. Nijmeijer, F. Roozeboom, and M. W. J. Luiten-Olieman, Atmospheric-pressure atomic layer deposition: Recent applications and new emerging applications in high-porosity/3D materials, *Dalton Trans.* **52**, 10254 (2023).
- [10] IRDS, International Roadmap for Devices and Systems 2023 Edition: More Than Moore (2023) (available at: <https://irds.ieee.org/editions/2023>) (accessed May 5, 2024).
- [11] D. Muñoz-Rojas, T. Maindron, A. Esteve, F. Piallat, J. C. S. Kools, and J. M. Decams, Speeding up the unique assets of atomic layer deposition, *Mater. Today Chem.* **12**, 96 (2019).
- [12] K. P. Musselman, C. F. Uzoma, and M. S. Miller, Nanomanufacturing: High-throughput, cost-effective deposition of atomic scale thin films via atmospheric pressure spatial atomic layer deposition, *Chem. Mater.* **28**, 8443 (2016).
- [13] D. Muñoz-Rojas, V. H. Nguyen, C. Masse de la Huerta, S. Aghazadehchors, C. Jiménez, and D. Bellet, Spatial atomic layer deposition (SALD), an emerging tool for energy materials. Application to new-generation photovoltaic devices and transparent conductive materials, *C. R. Phys.* **18**, 391 (2017).
- [14] B. O’Donnell, The weekend read: Atomic layer deposition storms market for PERC, PV Magazine (2019) (available at: <https://www.pv-magazine.com/2019/06/29/the-weekend-read-atomic-layer-deposition-storms-market-for-perc/>) (accessed April 7, 2024).

- [15] G. Coletti, W. Sinke, and J. Bultman, International Technology Roadmap for Photovoltaics (ITRPV) 2013 Results, 5th Edition (2014) (available at: https://www.semi.org/sites/semi.org/files/docs/ITRPV_2014_Roadmap_Revision1_140324.pdf) (accessed April 10, 2024).
- [16] D. H. Levy, D. Freeman, S. F. Nelson, P. J. Cowdery-Corvan, and L. M. Irving, Stable ZnO thin film transistors by fast open air atomic layer deposition, *Appl. Phys. Lett.* **92**, 192101 (2008).
- [17] P. Poodt, D. C. Cameron, E. Dickey, S. M. George, V. Kuznetsov, G. N. Parsons, F. Roozeboom, G. Sundaram, and A. Vermeer, Spatial atomic layer deposition: A route towards further industrialization of atomic layer deposition, *J. Vac. Sci. Technol., A* **30**, 010802 (2012).
- [18] A. Illiberi, B. Cobb, A. Sharma, T. Grehl, H. Brongersma, F. Roozeboom, G. Gelinck, and P. Poodt, Spatial atmospheric atomic layer deposition of $In_xGa_yZn_zO$ for thin film transistors, *ACS Appl. Mater. Interfaces* **7**, 3671 (2015).
- [19] C. R. Ellinger and S. F. Nelson, Selective area spatial atomic layer deposition of ZnO, Al₂O₃, and aluminum-doped ZnO using poly(vinyl pyrrolidone), *Chem. Mater.* **26**, 1514 (2014).
- [20] K. P. Musselman, D. Muñoz-Rojas, R. L. Z. Hoye, H. Sun, S. L. Sahonta, E. Croft, M. L. Böhm, C. Ducati, and J. L. MacManus-Driscoll, Rapid open-air deposition of uniform, nanoscale, functional coatings on nanorod arrays, *Nanoscale Horiz.* **2**, 110 (2017).
- [21] R. L. Z. Hoye and J. L. MacManus-Driscoll, in *Micro and Nano Technologies*, edited by D. Ginley and T. Fix (Elsevier, 2019), pp. 245–277.
- [22] C. Barbos, D. Blanc-Pelissier, A. Fave, E. Blanquet, A. Crisci, E. Fourmond, D. Albertini, A. Sabac, K. Ayadi, P. Girard, and M. Lemitti, Characterization of Al₂O₃ thin films prepared by thermal ALD, *Energy Procedia* **77**, 558 (2015).
- [23] P. Poodt, A. Lankhorst, F. Roozeboom, K. Spee, D. Maas, and A. Vermeer, High-speed spatial atomic-layer deposition of aluminum oxide layers for solar cell passivation, *Adv. Mater.* **22**, 3564 (2010).
- [24] V. Kuznetsov, E. Granneman, P. Vermont, and K. Vanormelingen, High throughput ALD of Al₂O₃ layers for surface passivation of silicon solar cells, *ECS Trans.* **33**, 441 (2010).
- [25] F. Werner, W. Stals, R. Görtzen, B. Veith, R. Brendel, and J. Schmidt, High-rate atomic layer deposition of Al₂O₃ for the surface passivation of Si solar cells, *Energy Procedia* **8**, 301 (2011).
- [26] D. H. Levy, S. F. Nelson, and D. Freeman, Oxide electronics by spatial atomic layer deposition, *IEEE/OSA J. Disp. Technol.* **5**, 484 (2009).
- [27] I. Katsouras, C. Frijters, P. Poodt, G. Gelinck, and A. J. Kronemeijer, Large-area spatial atomic layer deposition of amorphous oxide semiconductors at atmospheric pressure, *J. Soc. Inf. Disp.* **27**, 304 (2019).
- [28] K. S. Yoo, D. G. Kim, S. Lee, W. B. Lee, and J. S. Park, Atmospheric pressure spatial ALD of Al₂O₃ thin films for flexible PEALD IGZO TFT application, *Ceram. Int.* **48**, 18803 (2022).
- [29] P. Poodt, V. Tiba, F. Werner, J. Schmidt, A. Vermeer, and F. Roozeboom, Ultrafast atomic layer deposition of alumina layers for solar cell passivation, *J. Electrochem. Soc.* **158**, H937 (2011).
- [30] A. Illiberi, C. Frijters, E. Balder, P. Poodt, and F. Roozeboom, Spatial atmospheric ALD of functional layers for CIGS solar cells, *ECS Trans.* **69**, 31 (2015).
- [31] L. Hoffmann, D. Theirich, T. Hasselmann, A. Räupke, D. Schlamm, and T. Riedl, Gas permeation barriers deposited by atmospheric pressure plasma enhanced atomic layer deposition, *J. Vac. Sci. Technol., A* **34**, 01A114 (2016).
- [32] L. Hoffmann, D. Theirich, S. Pack, F. Kocak, D. Schlamm, T. Hasselmann, H. Fahl, A. Raupke, H. Gargouri, and T. Riedl, Gas diffusion barriers prepared by spatial atmospheric pressure plasma enhanced ALD, *ACS Appl. Mater. Interfaces* **9**, 4171 (2017).
- [33] M. B. M. Mousa, C. J. Oldham, and G. N. Parsons, Precise nanoscale surface modification and coating of macroscale objects: Open-environment in loco atomic layer deposition on an automobile, *ACS Appl. Mater. Interfaces* **7**, 19523 (2015).
- [34] A. Illiberi, R. Scherpenborg, Y. Wu, F. Roozeboom, and P. Poodt, Spatial atmospheric atomic layer deposition of Al_xZn_{1-x}O, *ACS Appl. Mater. Interfaces* **5**, 13124 (2013).
- [35] T. Törndahl, C. Platzer-Björkman, J. Kessler, and M. Edoff, Atomic layer deposition of Zn_{1-x}Mg_xO buffer layers for Cu(In, Ga)Se₂ solar cells, *Prog. Photovoltaics* **15**, 225 (2007).
- [36] A. Illiberi, F. Roozeboom, and P. Poodt, Spatial atomic layer deposition of zinc oxide thin films, *ACS Appl. Mater. Interfaces* **4**, 268 (2012).
- [37] R. L. Z. Hoye, D. Muñoz-Rojas, K. P. Musselman, Y. Vaynzof, and J. L. MacManus-Driscoll, Synthesis and modeling of uniform complex metal oxides by close-proximity atmospheric pressure chemical vapor deposition, *ACS Appl. Mater. Interfaces* **7**, 10684 (2015).
- [38] T. Chenvidhya, K. Kirtikara, D. Chenvidhya, R. Songprakorp, and W. Seekaew, in *The 6th World Conference on Photovoltaic Energy Conversion 2014 (WCPEC-6)* (2014).
- [39] S. F. Nelson, D. H. Levy, L. W. Tutt, and M. Burberry, Cycle time effects on growth and transistor characteristics of spatial atomic layer deposition of zinc oxide, *J. Vac. Sci. Technol., A* **30**, 01A154 (2012).
- [40] C. H. Frijters, P. Poodt, and A. Illiberi, Atmospheric spatial atomic layer deposition of Zn(O, S) buffer layer for Cu(In, Ga)Se₂ solar cells, *Sol. Energy Mater. Sol. Cells* **155**, 356 (2016).
- [41] M. Najafi, V. Zardetto, D. Zhang, D. Koushik, M. S. Dörenkämper, M. Creatore, R. Andriessen, P. Poodt, and S. Veenstra, Highly efficient and stable semi-transparent *p-i-n* planar perovskite solar cells by atmospheric pressure spatial atomic layer deposited ZnO, *Sol. RRL* **2**, 1800147 (2018).
- [42] A. Illiberi, C. Frijters, M. Ruth, D. Bremaud, P. Poodt, F. Roozeboom, and P. J. Bolt, Atmospheric spatial atomic layer deposition of ZnOS buffer layers for flexible Cu(In, Ga)Se₂ solar cells, *J. Vac. Sci. Technol., A* **36**, 051511 (2018).

- [43] A. Illiberi, R. Scherpenborg, F. Roozeboom, and P. Poodt, Atmospheric spatial atomic layer deposition of In-doped ZnO, *ECS J. Solid State Sci. Technol.* **3**, P111 (2014).
- [44] A. Illiberi, I. Katsouras, S. Gazibegovic, B. Cobb, E. Nekovic, W. van Boekel, C. Frijters, J. Maas, F. Roozeboom, Y. Creyghton, P. Poodt, and G. Gelinck, Atmospheric plasma-enhanced spatial-ALD of InZnO for high mobility thin film transistors, *J. Vac. Sci. Technol., A* **36**, 04F401 (2018).
- [45] M. Ritala, M. Leskelä, E. Nykänen, P. Soininen, and L. Niinistö, Growth of titanium dioxide thin films by atomic layer epitaxy, *Thin Solid Films* **225**, 288 (1993).
- [46] M. Aghaee, P. S. Maydannik, P. Johansson, J. Kuusipalo, M. Creatore, T. Homola, and D. C. Cameron, Low temperature temporal and spatial atomic layer deposition of TiO₂ films, *J. Vac. Sci. Technol., A* **33**, 41512 (2015).
- [47] M. Aghaee, J. Verheyen, A. A. E. Stevens, W. M. M. Kessels, and M. Creatore, TiO₂ thin film patterns prepared by chemical vapor deposition and atomic layer deposition using an atmospheric pressure microplasma printer, *Plasma Processes Polym.* **16**, 1900127 (2019).
- [48] L. Midani, W. Ben-Yahia, V. Salles, and C. Marichy, Nanofabrication via maskless localized atomic layer deposition of patterned nanoscale metal oxide films, *ACS Appl. Nano Mater.* **4**, 11980 (2021).
- [49] I. Kudrata, M. K. S. Barr, S. Tymek, D. Döhler, B. Hudec, P. Brüner, G. Vanko, M. Precner, T. Yokosawa, E. Spiecker, M. Plakhotnyuk, K. Fröhlich, and J. Bachmann, Additive manufacturing in atomic layer processing mode, *Small Methods* **6**, 2101546 (2022).
- [50] B. B. Burton, D. N. Goldstein, and S. M. George, Atomic layer deposition of MgO using bis(ethylcyclopentadienyl) magnesium and H₂O, *J. Phys. Chem. C* **113**, 1939 (2009).
- [51] A. Sekkat, D. T. Papanastasiou, M. A. Ghani, H. Roussel, M. Weber, L. Rapenne, C. Jiménez, D. Muñoz-Rojas, and D. Bellet, Highly transparent and stable flexible electrodes based on MgO/AgNW nanocomposites for transparent heating applications, *Adv. Mater. Technol.* **8**, 2301143 (2023).
- [52] B. Karasulu, F. Roozeboom, and A. Mameli, High-throughput area-selective spatial atomic layer deposition of SiO₂ with interleaved small molecule inhibitors and integrated back-etch correction for low defectivity, *Adv. Mater.* **35**, 2301204 (2023).
- [53] Spatial ALD: Beneq C2R™, <https://beneq.com/c2r/> (accessed October 10, 2024).
- [54] V. H. Nguyen, M. Akbari, A. Sekkat, H. T. T. Ta, J. Resende, C. Jiménez, K. P. Musselman, and D. Muñoz-Rojas, Atmospheric atomic layer deposition of SnO₂ thin films with tin(II) acetylacetone and water, *Dalton Trans.* **51**, 9278 (2022).
- [55] M. G. Chae, S. H. Han, B. K. Park, T. M. Chung, and J. H. Han, Atomic-layer-deposited SnO film using novel Sn(dmamb)₂ precursor for *p*-channel thin film transistor, *Appl. Surf. Sci.* **547**, 148758 (2021).
- [56] A. Mameli, J. D. Parish, T. Dogan, G. Gelinck, M. W. Snook, A. J. Straiton, A. L. Johnson, and A. J. Krone-mijer, High-throughput atomic layer deposition of *p*-type SnO thin film transistors using tin(II)bis(tert-amyloxide), *Adv. Mater. Interfaces* **9**, 2101278 (2022).
- [57] L. Hoffmann, K. O. Brinkmann, J. Malerczyk, D. Rogalla, T. Becker, D. Theirich, I. Shutsko, P. Görrn, and T. Riedl, Spatial atmospheric pressure atomic layer deposition of tin oxide as an impermeable electron extraction layer for perovskite solar cells with enhanced thermal stability, *ACS Appl. Mater. Interfaces* **10**, 6006 (2018).
- [58] Lukas Hoffmann, Detlef Theirich, Daniel Schlamm, Tim Hasselmann, Sven Pack, Kai Oliver Brinkmann, Detlef Rogalla, Sven Peters, André Räupke, Hassan Gargouri, and Thomas Riedl, Atmospheric pressure plasma enhanced spatial atomic layer deposition of SnO_x as conductive gas diffusion barrier, *J. Vac. Sci. Technol., A* **36**, 01A112 (2018).
- [59] A. Sekkat, V. H. Nguyen, C. A. Masse de La Huerta, L. Rapenne, D. Bellet, A. Kaminski-Cachopo, G. Chichignoud, and D. Muñoz-Rojas, Open-air printing of Cu₂O thin films with high hole mobility for semitransparent solar harvesters, *Commun. Mater.* **2**, 78 (2021).
- [60] Robert A. Jagt, Tahmida N. Huq, Sam A. Hill, Maung Thway, Tianyuan Liu, Mari Napari, Bart Roose, Krzysztof Galkowski, Weiwei Li, Serena Fen Lin, Samuel D. Stranks, Judith L. MacManus-Driscoll, and Robert L. Z. Hoyer, Rapid vapor-phase deposition of high-mobility *p*-type buffer layers on perovskite photovoltaics for efficient semitransparent devices, *ACS Energy Lett.* **5**, 2456 (2020).
- [61] D. Muñoz-Rojas, M. Jordan, C. Yeoh, A. T. Marin, A. Kursumovic, L. A. Dunlop, D. C. Iza, A. Chen, H. Wang, and J. L. MacManus Driscoll, Growth of $\sim 5 \text{ cm}^2 \text{ V}^{-1} \text{ s}^{-1}$ mobility, *p*-type copper(I) oxide (Cu₂O) films by fast atmospheric atomic layer deposition (AALD) at 225 °C and below, *AIP Adv.* **2**, 42179 (2012).
- [62] M. A. Mione, I. Katsouras, Y. Creyghton, W. van Boekel, J. Maas, G. Gelinck, F. Roozeboom, and A. Illiberi, Atmospheric pressure plasma enhanced spatial ALD of ZrO₂ for low-temperature, large-area applications, *ECS J. Solid State Sci. Technol.* **6**, N243 (2017).
- [63] F. Toldra-Reig, C. Lausecker, M. Weber, M. Bechelany, and D. Muñoz-Rojas, Custom 3D printed spatial atomic layer deposition manifold for the coating of tubular membranes, *ACS Sustainable Chem. Eng.* **10**, 14112 (2022).
- [64] D. Muñoz-Rojas and J. MacManus-Driscoll, Spatial atmospheric atomic layer deposition: A new laboratory and industrial tool for low-cost photovoltaics, *Mater. Horiz.* **1**, 314 (2014).
- [65] R. L. Z. Hoyer, D. Muñoz-Rojas, S. F. Nelson, A. Illiberi, P. Poodt, F. Roozeboom, and J. L. MacManus-Driscoll, Research update: Atmospheric pressure spatial atomic layer deposition of ZnO thin films: Reactors, doping, and devices, *APL Mater.* **3**, 040701 (2015).
- [66] R. D. Ranninga, R. A. Jagt, S. Béchu, T. N. Huq, W. Li, M. Nikolka, Y.-H. Lin, M. Sun, Z. Li, W. Li, M. Bouttemy, M. Frégnaux, H. J. Snaith, P. Schulz, J. L. MacManus-Driscoll, and R. L. Z. Hoyer, Strong performance enhancement in lead-halide perovskite solar cells through rapid, atmospheric deposition of *n*-type buffer layer oxides, *Nano Energy* **75**, 104946 (2020).

- [67] Fraunhofer Institute for Solar Energy, Photovoltaics Report (2024). <https://www.ise.fraunhofer.de/en/publications/studies/photovoltaics-report.html> (accessed October 3, 2024).
- [68] J. C. Blakesley, R. S. Bonilla, M. Freitag, A. M. Ganose, N. Gasparini, P. Kaienburg, G. Koutsourakis, J. D. Major, J. Nelson, N. K. Noel, B. Roose, *et al.*, Roadmap on established and emerging photovoltaics for sustainable energy conversion, *J. Phys. Energy* **6**, 041501 (2024).
- [69] J. Benick, B. Hoex, M. C. M. van de Sanden, W. M. M. Kessels, O. Schultz, and S. W. Glunz, High efficiency *n*-type Si solar cells on Al₂O₃-passivated boron emitters, *Appl. Phys. Lett.* **92**, 253504 (2008).
- [70] J. Kim, S. Lee, S. Chowdhury, and J. Yi, A brief review of passivation materials and process for high efficiency PERC solar cell, *Trans. Electr. Electron. Mater.* **23**, 1 (2022).
- [71] G. Dingemans, N. M. Terlinden, D. Pierreux, H. B. Profijt, M. C. M. Van De Sanden, and W. M. M. Kessels, Influence of the oxidant on the chemical and field-effect passivation of Si by ALD Al₂O₃, *Electrochem. Solid-State Lett.* **14**, H1 (2011).
- [72] P. Saint-Cast, Y. H. Heo, E. Billot, P. Olwal, M. Hofmann, J. Rentsch, S. W. Glunz, and R. Preu, Variation of the layer thickness to study the electrical property of PECVD Al₂O₃/c-Si interface, *Energy Procedia* **8**, 642 (2011).
- [73] J. Benick, A. Richter, T.-T. A. Li, N. E. Grant, K. R. McIntosh, Y. Ren, K. J. Weber, M. Hermle, and S. W. Glunz, in *2010 35th IEEE Photovoltaic Specialists Conference* (June 20–25, 2010).
- [74] F. Werner, B. Veith, D. Zielke, L. Kühnemund, C. Tegenkamp, M. Seibt, R. Brendel, and J. Schmidt, Electronic and chemical properties of the c-Si/Al₂O₃ interface, *J. Appl. Phys.* **109**, 113701 (2011).
- [75] F. Werner, B. Veith, V. Tiba, P. Poodt, F. Roozeboom, R. Brendel, and J. Schmidt, Very low surface recombination velocities on *p*- and *n*-type c-Si by ultrafast spatial atomic layer deposition of aluminum oxide, *Appl. Phys. Lett.* **97**, 162103 (2010).
- [76] G. Dingemans and W. M. M. Kessels, Status and prospects of Al₂O₃-based surface passivation schemes for silicon solar cells, *J. Vac. Sci. Technol., A* **30**, 040802 (2012).
- [77] Y. Creyghton, A. Illiberi, A. Mione, W. van Boekel, N. Debernardi, M. Seitz, F. van den Bruele, P. Poodt, and F. Roozeboom, Plasma-enhanced atmospheric-pressure spatial ALD of Al₂O₃ and ZrO₂, *ECS Trans.* **75**, 11 (2016).
- [78] B. Hoex, J. Schmidt, P. Pohl, M. C. M. van de Sanden, and W. M. M. Kessels, Silicon surface passivation by atomic layer deposited Al₂O₃, *J. Appl. Phys.* **104**, 44903 (2008).
- [79] J. Schmidt, A. Merkle, R. Brendel, B. Hoex, M. C. M. van de Sanden, and W. M. M. Kessels, Surface passivation of high-efficiency silicon solar cells by atomic-layer-deposited Al₂O₃, *Prog. Photovoltaics* **16**, 461 (2008).
- [80] G. Dingemans, R. Seguin, P. Engelhart, M. C. M. van de Sanden, and W. M. M. Kessels, Silicon surface passivation by ultrathin Al₂O₃ films synthesized by thermal and plasma atomic layer deposition, *Phys. Status Solidi RRL* **4**, 10 (2010).
- [81] M. Z. Rahman and S. I. Khan, Advances in surface passivation of c-Si solar cells, *Mater. Renew. Sustain. Energy* **1**, 734 (2012).
- [82] M. A. Hossain, K. T. Khoo, X. Cui, G. K. Poduval, T. Zhang, X. Li, W. M. Li, and B. Hoex, Atomic layer deposition enabling higher efficiency solar cells: A review, *Nano Mater. Sci.* **2**, 204 (2020).
- [83] R. S. Bonilla, B. Hoex, P. Hamer, and P. R. Wilshaw, Dielectric surface passivation for silicon solar cells: A review, *Phys. Status Solidi A* **214**, 39 (2017).
- [84] M. A. Mione, V. Vandalon, W. M. M. Kessels, and F. Roozeboom, Temperature study of atmospheric-pressure plasma-enhanced spatial ALD of Al₂O₃ using infrared and optical emission spectroscopy, *J. Vac. Sci. Technol., A* **40**, 062407 (2022).
- [85] B. Macco, M. L. van de Poll, B. W. H. van de Loo, T. M. P. Broekema, S. B. Basuvalingam, C. A. A. van Helvoirt, W. J. H. Berghuis, R. J. Theeuwes, N. Phung, and W. M. M. Kessels, Temporal and spatial atomic layer deposition of Al-doped zinc oxide as a passivating conductive contact for silicon solar cells, *Sol. Energy Mater. Sol. Cells* **245**, 111869 (2022).
- [86] G. Gregory, C. Luderer, H. Ali, T. S. Sakthivel, T. Jurca, M. Bivour, S. Seal, and K. O. Davis, Spatial atomic layer deposition of molybdenum oxide for industrial solar cells, *Adv. Mater. Interfaces* **7**, 2000895 (2020).
- [87] J. Meyer, S. Hamwi, M. Kröger, W. Kowalsky, T. Riedl, and A. Kahn, Transition metal oxides for organic electronics: Energetics, device physics and applications, *Adv. Mater.* **24**, 5408 (2012).
- [88] B. Vermang, V. Fjällström, X. Gao, and M. Edoff, Improved rear surface passivation of Cu(In, Ga)Se₂ solar cells: A combination of an Al₂O₃ rear surface passivation layer and nanosized local rear point contacts, *IEEE J. Photovoltaics* **4**, 486 (2014).
- [89] I. T. S. Heikkinen, P. Repo, V. Vähäniemi, T. Pasanen, V. Malinen, and H. Savin, Efficient surface passivation of black silicon using spatial atomic layer deposition, *Energy Procedia* **124**, 282 (2017).
- [90] Benedict O'Donnell, *The Weekend Read: Atomic Layer Deposition Storms Market for PERC*, <https://www.pv-magazine.com/2019/06/29/the-weekend-read-atomic-layer-deposition-storms-market-for-perc/>
- [91] R. L. Z. Hoye, B. Ehrler, M. L. Böhm, D. Muñoz - Rojas, R. M. Altamimi, A. Y. Alyamani, Y. Vaynzof, A. Sadhanala, G. Ercolano, N. C. Greenham, R. H. Friend, J. L. MacManus-Driscoll, and K. P. Musselman, Improved open-circuit voltage in ZnO-PbSe quantum dot solar cells by understanding and reducing losses arising from the ZnO Conduction Band Tail, *Adv. Energy Mater.* **4**, 1301544 (2014).
- [92] V. Andrei, R. A. Jagt, M. Rahaman, L. Lari, V. K. Lazarov, J. L. MacManus-Driscoll, R. L. Z. Hoye, and E. Reisner, Long-term solar water and CO₂ splitting with photoelectrochemical BiOI-BiVO₄ tandems, *Nat. Mater.* **21**, 864 (2022).
- [93] B. Zhao, L. C. Lee, L. Yang, A. J. Pearson, H. Lu, X.-J. She, L. Cui, K. H. L. Zhang, R. L. Z. Hoye, A. Karani, P. Xu, A. Sadhanala, N. C. Greenham, R. H. Friend, J. L. MacManus-Driscoll, and D. Di, In situ atmospheric

- deposition of ultrasmooth nickel oxide for efficient perovskite solar cells, *ACS Appl. Mater. Interfaces* **10**, 41849 (2018).
- [94] D. Muñoz-Rojas, H. Sun, D. C. Iza, J. Weickert, L. Chen, H. Wang, L. Schmidt-Mende, and J. L. MacManus-Driscoll, High-speed atmospheric atomic layer deposition of ultra thin amorphous TiO₂ blocking layers at 100 °C for inverted bulk heterojunction solar cells, *Prog. Photovoltaics* **21**, 393 (2013).
- [95] C. J. Brabec, in *Semiconductor Aspects of Organic Bulk Heterojunction Solar Cells BT - Organic Photovoltaics: Concepts and Realization*, edited by C. J. Brabec, V. Dyakonov, J. Parisi, and N. S. Sariciftci (Springer-Verlag, Berlin, 2003), pp. 159–248.
- [96] J. Hou, O. Inganäs, R. H. Friend, and F. Gao, Organic solar cells based on non-fullerene acceptors, *Nat. Mater.* **17**, 119 (2018).
- [97] D. Theirich, R. Müller, K. Zilberberg, S. Trost, A. Behrendt, and T. Riedl, Atmospheric pressure plasma ALD of titanium oxide, *Chem. Vap. Deposition* **19**, 167 (2013).
- [98] R. L. Z. Hoye, D. Muñoz-Rojas, D. C. Iza, K. P. Musselman, and J. L. MacManus-Driscoll, High performance inverted bulk heterojunction solar cells by incorporation of dense, thin ZnO layers made using atmospheric atomic layer deposition, *Sol. Energy Mater. Sol. Cells* **116**, 197 (2013).
- [99] K. O. Brinkmann, T. Gahlmann, and T. Riedl, Atomic layer deposition of functional layers in planar perovskite solar cells, *Sol. RRL* **4**, 1900332 (2020).
- [100] H. Jo, J. K. Kim, J. Kim, T.-Y. Seong, H. J. Son, J.-H. Jeong, and H. Yu, Unprecedentedly large photocurrents in colloidal PbS quantum-dot solar cells enabled by atomic layer deposition of zinc oxide electron buffer layer, *ACS Appl. Energy Mater.* **4**, 13776 (2021).
- [101] K.-M. Lee, S. H. Chang, K.-H. Wang, C.-M. Chang, H.-M. Cheng, C.-C. Kei, Z.-L. Tseng, and C.-G. Wu, Thickness effects of ZnO thin film on the performance of tri-iodide perovskite absorber based photovoltaics, *Sol. Energy* **120**, 117 (2015).
- [102] B. Ehrler, K. P. Musselman, M. L. Böhm, F. S. F. Morgenstern, Y. Vaynzof, B. J. Walker, J. L. MacManus-Driscoll, and N. C. Greenham, Preventing interfacial recombination in colloidal quantum dot solar cells by doping the metal oxide, *ACS Nano* **7**, 4210 (2013).
- [103] K. P. Musselman, S. Albert-Seifried, R. L. Z. Hoye, A. Sadhanala, D. Muñoz-Rojas, J. L. MacManus-Driscoll, and R. H. Friend, Improved exciton dissociation at semiconducting polymer:ZnO donor:acceptor interfaces via nitrogen doping of ZnO, *Adv. Funct. Mater.* **24**, 3562 (2014).
- [104] Y. Kuang, V. Zardetto, R. van Gils, S. Karwal, D. Koushik, M. A. Verheijen, L. E. Black, C. Weijtens, S. Veenstra, R. Andriessen, W. M. M. Kessels, and M. Creatore, Low-temperature plasma-assisted atomic-layer-deposited SnO₂ as an electron transport layer in planar perovskite solar cells, *ACS Appl. Mater. Interfaces* **10**, 30367 (2018).
- [105] V. Zardetto, F. di Giacomo, H. Lifka, M. A. Verheijen, C. H. L. Weijtens, L. E. Black, S. Veenstra, W. M. M. Kessels, R. Andriessen, and M. Creatore, Surface fluorination of ALD TiO₂ electron transport layer for efficient planar perovskite solar cells, *Adv. Mater. Interfaces* **5**, 1701456 (2018).
- [106] C. L. Armstrong, M. B. Price, D. Muñoz-Rojas, N. J. K. L. Davis, M. Abdi-Jalebi, R. H. Friend, N. C. Greenham, J. L. MacManus-Driscoll, M. L. Böhm, and K. P. Musselman, Influence of an inorganic interlayer on exciton separation in hybrid solar cells, *ACS Nano* **9**, 11863 (2015).
- [107] S. Seo, S. Jeong, C. Bae, N.-G. Park, and H. Shin, Perovskite solar cells with inorganic electron- and hole-transport layers exhibiting long-term (\approx 500 h) stability at 85 °C under continuous 1 sun illumination in ambient air, *Adv. Mater.* **30**, 1801010 (2018).
- [108] V. S. Nguyen, A. Sekkat, D. Bellet, G. Chichignoud, A. Kaminski-Cachopo, D. Muñoz-Rojas, and W. Favre, Open-air, low-temperature deposition of phase pure Cu₂O thin films as efficient hole-transporting layers for silicon heterojunction solar cells, *J. Mater. Chem. A* **9**, 15968 (2021).
- [109] J. Kaur, O. Bethge, R. A. Wibowo, N. Bansal, M. Bauch, R. Hamid, E. Bertagnolli, and T. Dimopoulos, All-oxide solar cells based on electrodeposited Cu₂O absorber and atomic layer deposited ZnMgO on precious-metal-free electrode, *Sol. Energy Mater. Sol. Cells* **161**, 449 (2017).
- [110] Y. S. Lee, D. Chua, R. E. Brandt, S. C. Siah, J. V. Li, J. P. Mailoa, S. W. Lee, R. G. Gordon, and T. Buonassisi, Atomic layer deposited gallium oxide buffer layer enables 1.2 V open-circuit voltage in cuprous oxide solar cells, *Adv. Mater.* **26**, 4704 (2014).
- [111] Y. Ievskaya, R. L. Z. Hoye, A. Sadhanala, K. P. Musselman, and J. L. MacManus-Driscoll, Fabrication of ZnO/Cu₂O heterojunctions in atmospheric conditions: Improved interface quality and solar cell performance, *Sol. Energy Mater. Sol. Cells* **135**, 43 (2015).
- [112] R. L. Z. Hoye, S. Heffernan, Y. Ievskaya, A. Sadhanala, A. Flewitt, R. H. Friend, J. L. MacManus-Driscoll, and K. P. Musselman, Engineering Schottky contacts in open-air fabricated heterojunction solar cells to enable high performance and Ohmic charge transport, *ACS Appl. Mater. Interfaces* **6**, 22192 (2014).
- [113] R. L. Z. Hoye, L. C. Lee, R. C. Kurchin, T. N. Huq, K. H. L. Zhang, M. Sponseller, L. Nienhaus, R. E. Brandt, J. Jean, J. A. Polizzotti, A. Kursumović, M. G. Bawendi, V. Bulović, V. Stevanović, T. Buonassisi, and J. L. MacManus-Driscoll, Strongly enhanced photovoltaic performance and defect physics of air-stable bismuth oxyiodide (BiOI), *Adv. Mater.* **29**, 1702176 (2017).
- [114] A. T. Marin, D. Muñoz-Rojas, D. C. Iza, T. Gershon, K. P. Musselman, and J. L. MacManus-Driscoll, Novel atmospheric growth technique to improve both light absorption and charge collection in ZnO/Cu₂O thin film solar cells, *Adv. Funct. Mater.* **23**, 3413 (2013).
- [115] L. Dunlop, A. Kursumovic, and J. L. MacManus-Driscoll, Reproducible growth of *p*-type ZnO : N using a modified atomic layer deposition process combined with dark annealing, *Appl. Phys. Lett.* **93**, 172111 (2008).
- [116] S. Seo, I. J. Park, M. Kim, S. Lee, C. Bae, H. S. Jung, N. G. Park, J. Y. Kim, and H. Shin, An ultra-thin, undoped NiO hole transporting layer of highly efficient (16.4%)

- organic-inorganic hybrid perovskite solar cells, *Nanoscale* **8**, 11403 (2016).
- [117] J. J. Yoo, G. Seo, M. R. Chua, T. G. Park, Y. Lu, F. Rotermund, Y.-K. Kim, C. S. Moon, N. J. Jeon, J.-P. Correa-Baena, V. Bulović, S. S. Shin, M. G. Bawendi, and J. Seo, Efficient perovskite solar cells via improved carrier management, *Nature* **590**, 587 (2021).
- [118] K. A. Bush, A. F. Palmstrom, J. Y. Zhengshan, M. Boccard, R. Cheacharoen, J. P. Mailoa, D. P. McMeekin, R. L. Z. Hoye, C. D. Bailie, T. Leijtens, *et al.*, 23.6%-efficient monolithic perovskite/silicon tandem solar cells with improved stability, *Nat. Energy* **2**, 17009 (2017).
- [119] A. F. Palmstrom, J. A. Raiford, R. Prasanna, K. A. Bush, M. Sponseller, R. Cheacharoen, M. C. Minichetti, D. S. Bergsman, T. Leijtens, H.-P. Wang, *et al.*, Interfacial effects of tin oxide atomic layer deposition in metal halide perovskite photovoltaics, *Adv. Energy Mater.* **8**, 1800591 (2018).
- [120] D. Choudhury, G. Rajaraman, and S. K. Sarkar, Self limiting atomic layer deposition of Al_2O_3 on perovskite surfaces: A reality? *Nanoscale* **8**, 7459 (2016).
- [121] I. S. Kim, D. H. Cao, D. B. Buchholz, J. D. Emery, O. K. Farha, J. T. Hupp, M. G. Kanatzidis, and A. B. F. Martinson, Liquid water- and heat-resistant hybrid perovskite photovoltaics via an inverted ALD oxide electron extraction layer design, *Nano Lett.* **16**, 7786 (2016).
- [122] J. Zhou, L. Tan, Y. Liu, H. Li, X. Liu, M. Li, S. Wang, Y. Zhang, C. Jiang, R. Hua, W. Tress, S. Meloni, and C. Yi, Highly efficient and stable perovskite solar cells via a multifunctional hole transporting material, *Joule* **8**, 1691 (2024).
- [123] Best Research-Cell Efficiency Chart, <https://www.nrel.gov/pv/cell-efficiency.html> (accessed January 16, 2025).
- [124] N. Mallik, J. Hajhemati, M. Frégniaux, D. Coutancier, A. Toby, S.-T. Zhang, C. Hartmann, E. Hüsam, A. Saleh, T. Vincent, *et al.*, Interface defect formation for atomic layer deposition of SnO_2 on metal halide perovskites, *Nano Energy* **126**, 109582 (2024).
- [125] A. Hultqvist, T. J. Jacobsson, S. Svanström, M. Edoff, U. B. Cappel, H. Rensmo, E. M. J. Johansson, G. Boschloo, and T. Törndahl, SnO_x atomic layer deposition on bare perovskite—an investigation of initial growth dynamics, interface chemistry, and solar cell performance, *ACS Appl. Energy Mater.* **4**, 510 (2021).
- [126] N. M. Mangan, R. E. Brandt, V. Steinmann, R. Jaramillo, C. Yang, J. R. Poindexter, R. Chakraborty, H. H. park, X. Zhao, R. G. Gordon, and T. Buonassisi, Framework to predict optimal buffer layer pairing for thin film solar cell absorbers: A case study for tin sulfide/zinc oxysulfide, *J. Appl. Phys.* **118**, 115102 (2015).
- [127] R. L. Z. Hoye, R. E. Brandt, Y. Ievskaya, S. Heffernan, K. P. Musselman, T. Buonassisi, and J. L. MacManus-Driscoll, Perspective: Maintaining surface-phase purity is key to efficient open air fabricated cuprous oxide solar cells, *APL Mater.* **3**, 20901 (2015).
- [128] S. W. Lee, Y. S. Lee, J. Heo, S. C. Siah, D. Chua, R. E. Brandt, S. B. Kim, J. P. Mailoa, T. Buonassisi, and R. G. Gordon, Improved Cu_2O -based solar cells using atomic layer deposition to control the Cu oxidation state at the *p-n* junction, *Adv. Energy Mater.* **4**, 1301916 (2014).
- [129] R. A. Jagt, T. N. Huq, K. M. Börsig, D. Sauven, L. C. Lee, J. L. MacManus-Driscoll, and R. L. Z. Hoye, Controlling the preferred orientation of layered BiOI solar absorbers, *J. Mater. Chem. C* **8**, 10791 (2020).
- [130] Tahmida N. Huq, Lana C. Lee, Lissa Eyre, Weiwei Li, Robert A. Jagt, Chaewon Kim, Sarah Fearn, Vincenzo Pecunia, Felix Deschler, Judith L. MacManus-Driscoll, and Robert L. Z. Hoye, Electronic structure and optoelectronic properties of bismuth oxyiodide robust against percent-level iodine-, oxygen-, and bismuth-related surface defects, *Adv. Funct. Mater.* **30**, 1909983 (2020).
- [131] H. Asgarimoghaddam, Q. Chen, F. Ye, A. Shahin, O. A. C. Marchione, B. Song, and K. P. Musselman, Spatial atomic layer deposition of nitrogen-doped alumina thin films for high-performance perovskite solar cell encapsulation, *Nano Energy* **127**, 109782 (2024).
- [132] A. Behrendt, C. Friedenberger, T. Gahlmann, S. Trost, T. Becker, K. Zilberberg, A. Polywka, P. Görrn, and T. Riedl, Highly robust transparent and conductive gas diffusion barriers based on tin oxide, *Adv. Mater.* **27**, 5961 (2015).
- [133] C.-T. Chou, P.-W. Yu, M.-H. Tseng, C.-C. Hsu, J.-J. Shyue, C.-C. Wang, and F.-Y. Tsai, Transparent conductive gas-permeation barriers on plastics by atomic layer deposition, *Adv. Mater.* **25**, 1750 (2013).
- [134] P. F. Garcia, R. S. McLean, M. H. Reilly, M. D. Groner, and S. M. George, Ca test of Al_2O_3 gas diffusion barriers grown by atomic layer deposition on polymers, *Appl. Phys. Lett.* **89**, 31915 (2006).
- [135] J. Meyer, H. Schmidt, W. Kowalsky, T. Riedl, and A. Kahn, The origin of low water vapor transmission rates through $\text{Al}_2\text{O}_3/\text{ZrO}_2$ nanolaminate gas-diffusion barriers grown by atomic layer deposition, *Appl. Phys. Lett.* **96**, 243308 (2010).
- [136] J. Meyer, P. Görrn, F. Bertram, S. Hamwi, T. Winkler, H.-H. Johannes, T. Weimann, P. Hinze, T. Riedl, and W. Kowalsky, $\text{Al}_2\text{O}_3/\text{ZrO}_2$ nanolaminates as ultrahigh gas-diffusion barriers—a strategy for reliable encapsulation of organic electronics, *Adv. Mater.* **21**, 1845 (2009).
- [137] M. H. Tseng, H. H. Yu, K. Y. Chou, J. H. Jou, K. L. Lin, C. C. Wang, and F. Y. Tsai, Low-temperature gas-barrier films by atomic layer deposition for encapsulating organic light-emitting diodes, *Nanotechnology* **27**, 295706 (2016).
- [138] H. Choi, S. Shin, H. Jeon, Y. Choi, J. Kim, S. Kim, S. C. Chung, and K. Oh, Fast spatial atomic layer deposition of Al_2O_3 at low temperature (<100 °C) as a gas permeation barrier for flexible organic light-emitting diode displays, *J. Vac. Sci. Technol., A* **34**, 01A121 (2015).
- [139] S. J. Kim, S. H. Yong, Y. J. Choi, H. Hwangbo, W.-Y. Yang, and H. Chae, Flexible Al_2O_3 /plasma polymer multilayer moisture barrier films deposited by a spatial atomic layer deposition process, *J. Vac. Sci. Technol., A* **38**, 22418 (2020).
- [140] H. Asgarimoghaddam, Q. Chen, F. Ye, A. Shahin, B. Song, and K. P. Musselman, Zinc aluminum oxide encapsulation layers for perovskite solar cells deposited using spatial atomic layer deposition, *Small Methods* **8**, 2300995 (2024).
- [141] H. Asgarimoghaddam, S. S. Khamgaonkar, A. Mathur, V. Maheshwari, and K. P. Musselman, Enhancing internal

- and external stability of perovskite solar cells through polystyrene modification of the perovskite and rapid open-air deposition of ZnO/AlO_x nanolaminate encapsulation, *Sol. RRL* **8**, 2400111 (2024).
- [142] H. Asgarimoghaddam, Q. Chen, F. Ye, A. Shahin, B. Song, and K. P. Musselman, Effect of different oxygen precursors on alumina deposited using a spatial atomic layer deposition system for thin-film encapsulation of perovskite solar cells, *Nanotechnology* **35**, 95401 (2024).
- [143] D. Koushik, W. J. H. Verhees, Y. Kuang, S. Veenstra, D. Zhang, M. A. Verheijen, M. Creatore, and R. E. I. Schropp, High-efficiency humidity-stable planar perovskite solar cells based on atomic layer architecture, *Energy Environ. Sci.* **10**, 91 (2017).
- [144] H. Park, S. Shin, H. Choi, N. Lee, Y. Choi, K. Kim, and H. Jeon, Thin-film encapsulation of Al_2O_3 multidensity layer structure prepared by spatial atomic layer deposition, *J. Vac. Sci. Technol., A* **38**, 062403 (2020).
- [145] S. H. Yong, S. J. Kim, J. S. Park, S. M. Cho, H. J. Ahn, and H. Chae, Flexible carbon-rich Al_2O_3 interlayers for moisture barrier films by a spatially-resolved atomic layer deposition process, *J. Korean Phys. Soc.* **73**, 40 (2018).
- [146] V. Pecunia, S. R. P. Silva, J. D. Phillips, E. Artegiani, A. Romeo, H. Shim, J. Park, J. H. Kim, J. S. Yun, G. C. Welch, *et al.*, Roadmap on energy harvesting materials, *J. Phys. Mater.* **6**, 42501 (2023).
- [147] Y. Peng, T. N. Huq, J. Mei, L. Portilla, R. A. Jagt, L. G. Occhipinti, J. L. MacManus-Driscoll, R. L. Z. Hoye, and V. Pecunia, Lead-free perovskite-inspired absorbers for indoor photovoltaics, *Adv. Energy Mater.* **11**, 2002761 (2021).
- [148] Y. Li, R. Goei, A. Jiamin Ong, Y. Zou, A. Shpatz Dayan, S. Rahmany, L. Etgar, and A. Iing Yoong Tok, Atomic layer deposition of piezoelectric materials: A timely review, *Mater. Today Energy* **39**, 101457 (2024).
- [149] J. Xu, Y. Zou, A. Nashalian, and J. Chen, Leverage surface chemistry for high-performance triboelectric nanogenerators, *Front. Chem.* **8**, 577327 (2020).
- [150] M. Tayyab, Z. Zhu, B. Wu, N. M. Abbasi, Y. Joseph, and D. Gao, Enhanced surface charge density of nanogenerators by small molecules: A review, *Energy Technol.* **11**, 2200879 (2023).
- [151] G. Marin, T. Tynell, and M. Karppinen, Flexible thermoelectric modules based on ALD-grown ZnO on different substrates, *J. Vac. Sci. Technol., A* **37**, 20906 (2019).
- [152] G. Marin, R. Funahashi, and M. Karppinen, Textile-integrated ZnO -based thermoelectric device using atomic layer deposition, *Adv. Eng. Mater.* **22**, 2000535 (2020).
- [153] A. H. Alshehri, K. Mistry, V. H. Nguyen, K. H. Ibrahim, D. Muñoz-Rojas, M. Yavuz, and K. P. Musselman, Quantum-tunneling metal-insulator-metal diodes made by rapid atmospheric pressure chemical vapor deposition, *Adv. Funct. Mater.* **29**, 1805533 (2019).
- [154] A. H. Alshehri, J. Y. Loke, V. Huong Nguyen, A. Jones, H. Asgarimoghaddam, L.-V. Delumeau, A. Shahin, K. H. Ibrahim, K. Mistry, M. Yavuz, D. Muñoz-Rojas, and K. P. Musselman, Nanoscale film thickness gradients printed in open air by spatially varying chemical vapor deposition, *Adv. Funct. Mater.* **31**, 1 (2021).
- [155] A. H. Alshehri, H. Asgarimoghaddam, L. V. Delumeau, V. H. Nguyen, A. Ali, M. Aljaghtham, A. Alamry, M. Yavuz, and K. P. Musselman, Combinatorial optimization of metal-insulator-insulator-metal (MIIM) diodes with thickness-gradient films via spatial atomic layer deposition, *Adv. Electron. Mater.* **10**, 2400093 (2024).
- [156] K. Mistry, V. Huong Nguyen, M. Arabi, K. H. Ibrahim, H. Asgarimoghaddam, M. Yavuz, D. Muñoz-Rojas, E. Abdel-Rahman, and K. P. Musselman, Highly sensitive self-actuated zinc oxide resonant microcantilever humidity sensor, *Nano Lett.* **22**, 3196 (2022).
- [157] C. Perumal Veeramalai, S. Feng, X. Zhang, S. V. N. Pammi, V. Pecunia, and C. Li, Lead-halide perovskites for next-generation self-powered photodetectors: a comprehensive review, *Photonics Res.* **9**, 968 (2021).
- [158] Y. Kim, S. Lee, J.-G. Song, K. Y. Ko, W. J. Woo, S. W. Lee, M. Park, H. Lee, Z. Lee, H. Choi, *et al.*, 2D transition metal dichalcogenide heterostructures for *p*- and *n*-type photovoltaic self-powered gas sensor, *Adv. Funct. Mater.* **30**, 2003360 (2020).
- [159] M. Akbari, H. Mouharrar, C. Crivello, M. Defoort, E. Abdel-Rahman, S. Basrour, K. Musselman, and D. Muñoz-Rojas, Gas phase growth of metal-organic frameworks on microcantilevers for highly sensitive detection of volatile organic compounds, *APL Mater.* **12**, 061119 (2024).
- [160] C. A. M. de la Huerta, V. H. Nguyen, A. Sekkat, C. Crivello, F. Toldra-Reig, P. B. Veiga, S. Quessada, C. Jimenez, and D. Muñoz-Rojas, Gas-phase 3D printing of functional materials, *Adv. Mater. Technol.* **5**, 2000657 (2020).
- [161] M. Grätzel, Photoelectrochemical cells, *Nature* **414**, 338 (2001).
- [162] V. Andrei, R. L. Z. Hoye, M. Crespo-Quesada, M. Bajada, S. Ahmad, M. De Volder, R. Friend, and E. Reisner, Scalable triple cation mixed halide perovskite– $BiVO_4$ tandems for bias-free water splitting, *Adv. Energy Mater.* **8**, 1801403 (2018).
- [163] L. Santonacci, in *Atomic Layer Deposition in Energy Conversion Applications*, edited by Julien Bachmann (Wiley-VCH Verlag GmbH & Co. KGaA, Weinheim, Germany, 2017), pp. 225–257.
- [164] Z. Chen, Y. Zhong, Z. Ma, and M. Si, Optimization design of surface optical characteristics of space solar cells based on transfer matrix method, *Jpn. J. Appl. Phys.* **63**, 35501 (2024).
- [165] A. Dey, J. Ye, A. De, E. Debroye, S. K. Ha, E. Bladt, A. S. Kshirsagar, Z. Wang, J. Yin, Y. Wang, *et al.*, State of the art and prospects for halide perovskite nanocrystals, *ACS Nano* **15**, 10775 (2021).
- [166] R. L. Z. Hoye, K. P. Musselman, M. R. Chua, A. Sadhanala, R. D. Ranasing, J. L. MacManus-Driscoll, R. H. Friend, and D. Credgington, Bright and efficient blue polymer light emitting diodes with reduced operating voltages processed entirely at low-temperature, *J. Mater. Chem. C* **3**, 9327 (2015).
- [167] H. Myja, Z. Yang, I. A. Goldthorpe, A. J. B. Jones, K. P. Musselman, A. Grundmann, H. Kalisch, A. Vescan, M. Heuken, T. Kümmell, and G. Bacher, Silver nanowire

- electrodes for transparent light emitting devices based on WS₂ monolayers, *Nanotechnology* **34**, 285201 (2023).
- [168] A. Pearse, T. Schmitt, E. Sahadeo, D. M. Stewart, A. Kozen, K. Gerasopoulos, A. A. Talin, S. B. Lee, G. W. Rubloff, and K. E. Gregorczyk, Three-dimensional solid-state lithium-ion batteries fabricated by conformal vapor-phase chemistry, *ACS Nano* **12**, 4286 (2018).
- [169] K. Sharma, D. Routkevitch, N. Varaksa, and S. M. George, Spatial atomic layer deposition on flexible porous substrates: ZnO on anodic aluminum oxide films and Al₂O₃ on Li ion battery electrodes, *J. Vac. Sci. Technol., A* **34**, 01A146 (2015).
- [170] A. S. Yersak, K. Sharma, J. M. Wallas, A. A. Dameron, X. Li, Y. Yang, K. E. Hurst, C. Ban, R. C. Tenent, and S. M. George, Spatial atomic layer deposition for coating flexible porous Li-ion battery electrodes, *J. Vac. Sci. Technol., A* **36**, 01A123 (2017).
- [171] S. Moitzheim, J. E. Balder, R. Ritasalo, S. Ek, P. Poodt, S. Unnikrishnan, S. De Gendt, and P. M. Vereecken, Toward 3D thin-film batteries: Optimal current-collector design and scalable fabrication of TiO₂ thin-film electrodes, *ACS Appl. Energy Mater.* **2**, 1774 (2019).
- [172] M. Li, P. Song, M. Hou, W. Feng, D. Zhao, and J. Zhang, Atomic-level functionalized carbon-based materials for effective electrosynthesis of hydrogen peroxide: A review, *Chem. Eng. J.* **479**, 147608 (2024).
- [173] C.-T. Hsieh, C.-H. Chao, W.-J. Ke, Y.-F. Lin, H.-W. Liu, Y. A. Gandomi, S. Gu, C.-Y. Su, J.-K. Chang, J. Li, C.-C. Fu, B. C. Mallick, and R.-S. Juang, Roll-to-roll atomic layer deposition of titania nanocoating on thermally stabilizing lithium nickel cobalt manganese oxide cathodes for lithium ion batteries, *ACS Appl. Energy Mater.* **3**, 10619 (2020).
- [174] A. Panda, J. Patra, C.-T. Hsieh, Y.-C. Huang, Y. A. Gandomi, C.-C. Fu, M.-H. Lin, R.-S. Juang, and J.-K. Chang, Improving high-temperature performance of lithium-rich cathode by roll-to-roll atomic layer deposition of titania nanocoating for lithium-ion batteries, *J. Energy Storage* **44**, 103348 (2021).
- [175] C.-T. Hsieh, B. C. Mallick, Y. A. Gandomi, Y.-C. Huang, C.-C. Fu, R.-S. Juang, and J.-K. Chang, Improvement on high-temperature electrochemical performance of lithium-ion pouch cells by spatial atomic layer deposition, *Electrochim. Acta* **423**, 140605 (2022).
- [176] J.-W. Lee, A. M. Soomro, M. Waqas, M. A. U. Khalid, and K. H. Choi, A highly efficient surface modified separator fabricated with atmospheric atomic layer deposition for high temperature lithium ion batteries, *Int. J. Energy Res.* **44**, 7035 (2020).
- [177] S. Moitzheim, J. E. Balder, P. Poodt, S. Unnikrishnan, S. De Gendt, and P. M. Vereecken, Chlorine doping of amorphous TiO₂ for increased capacity and faster Li⁺-ion storage, *Chem. Mater.* **29**, 10007 (2017).
- [178] Optimized Batteries via Spatial Atomic Layer Deposition, <https://www.spark-nano.com/spatial-ald/batteries/> (accessed December 12, 2024).
- [179] Spatial ALD in Battery Technology, <https://spatialald.com/markets/battery-technology/> (accessed December 12, 2024).
- [180] Enabling Safer and High Performing Batteries with ALD, <https://beneq.com/markets/batteries/> (accessed December 12, 2024).
- [181] Roll-to-Roll (R2R) System for Ultra-High-Volume, <https://www.spark-nano.com/products/omega-series/> (accessed December 12, 2024).
- [182] A. W. Weimer, From a laboratory curiosity to a commercial powder processing plant – A personal perspective, *Powder Technol.* **418**, 118279 (2023).
- [183] A. Anand, M. M. Islam, R. Meitzner, U. S. Schubert, and H. Hoppe, Introduction of a novel figure of merit for the assessment of transparent conductive electrodes in photovoltaics: Exact and approximate form, *Adv. Energy Mater.* **11**, 2100875 (2021).
- [184] V. H. Nguyen, D. Bellet, B. Masenelli, and D. Muñoz-Rojas, Increasing the electron mobility of ZnO-based transparent conductive films deposited by open-air methods for enhanced sensing performance, *ACS Appl. Nano Mater.* **1**, 6922 (2018).
- [185] A. Illiberi, F. Grob, C. Frijters, P. Poodt, R. Ramachandra, H. Winands, M. Simor, and P. J. Bolt, High rate (~7 nm/s), atmospheric pressure deposition of ZnO front electrode for Cu(In,Ga)Se₂ thin-film solar cells with efficiency beyond 15%, *Prog. Photovoltaics* **21**, 1559 (2013).
- [186] V. H. Nguyen, J. Resende, C. Jiménez, J.-L. Deschanvres, P. Carroy, D. Muñoz, D. Bellet, and D. Muñoz-Rojas, Deposition of ZnO based thin films by atmospheric pressure spatial atomic layer deposition for application in solar cells, *J. Renew. Sustain. Energy* **9**, 021203 (2017).
- [187] V. H. Nguyen, U. Gottlieb, A. Valla, D. Muñoz, D. Bellet, and D. Muñoz-Rojas, Electron tunneling through grain boundaries in transparent conductive oxides and implications for electrical conductivity: The case of ZnO : Al thin films, *Mater. Horiz.* **5**, 715 (2018).
- [188] Chia-Hsun Hsu, X. Geng, P. Huang, Wan-Yu Wu, Ming-Jie Zhao, Xiao-Ying Zhang, Qi-Hui Huang, Zhanmin Su, Zi-Rong Chen, Shui-Yang Lien, and W. Zhu, High doping efficiency Al-doped ZnO films prepared by co-injection spatial atomic layer deposition, *J. Alloys Compd.* **884**, 161025 (2021).
- [189] D. B. Fullager, G. D. Boreman, C. D. Ellinger, and T. Hofmann, Broadband optical properties of aluminium zinc oxide thin films prepared by spatial atomic layer deposition, *Thin Solid Films* **653**, 267 (2018).
- [190] C.-H. Hsu, X.-P. Geng, W.-Y. Wu, M.-J. Zhao, P.-H. Huang, X.-Y. Zhang, Z.-B. Su, Z.-R. Chen, and S.-Y. Lien, Effect of oxygen annealing temperature on properties of spatial atomic layer deposited aluminum-doped zinc oxide films, *Mater. Sci. Semicond. Process.* **133**, 105929 (2021).
- [191] A. Sekkat, M. O. Liedke, V. H. Nguyen, M. Butterling, F. Baiutti, J. de Dios Sirvent Veru, M. Weber, L. Rapenne, D. Bellet, G. Chichignoud, A. Kaminski-Cachopo, E. Hirschmann, A. Wagner, and D. Muñoz-Rojas, Chemical deposition of Cu₂O films with ultra-low resistivity: correlation with the defect landscape, *Nat. Commun.* **13**, 5322 (2022).
- [192] L. Bardet, H. Roussel, S. Saroglia, M. Akbari, D. Muñoz-Rojas, C. Jiménez, A. Denneulin, and D. Bellet, Exploring the degradation of silver nanowire networks under thermal

- stress by coupling in situ X-ray diffraction and electrical resistance measurements, *Nanoscale* **16**, 564 (2024).
- [193] K. Zilberberg, F. Gasse, R. Pagui, A. Polywka, A. Behrendt, S. Trost, R. Heiderhoff, P. Görnn, and T. Riedl, Highly robust Indium-free transparent conductive electrodes based on composites of silver nanowires and conductive metal oxides, *Adv. Funct. Mater.* **24**, 1671 (2014).
- [194] A. Khan, V. H. Nguyen, D. Muñoz-Rojas, S. Aghazadehchors, C. Jiménez, N. D. Nguyen, and D. Bellet, Stability enhancement of silver nanowire networks with conformal ZnO coatings deposited by atmospheric pressure spatial atomic layer deposition, *ACS Appl. Mater. Interfaces* **10**, 19208 (2018).
- [195] D. T. Papanastasiou, A. Mantoux, A. Crisci, H. Ribeiro, A. Sekkat, H. Roussel, M. Weber, L. Rapenne, C. Jiménez, M. Fivel, D. Bellet, E. Blanquet, and D. Muñoz-Rojas, Silver nanowire networks coated with a few nanometer thick aluminum nitride films for ultra-transparent and robust heating applications, *ACS Appl. Nano Mater.* **7**, 12312 (2024).
- [196] S. Hanauer, C. Celle, C. Crivello, H. Szambolics, D. Muñoz-Rojas, D. Bellet, and J.-P. Simonato, Transparent and mechanically resistant silver-nanowire-based low-emissivity coatings, *ACS Appl. Mater. Interfaces* **13**, 21971 (2021).
- [197] V. H. Nguyen, J. Resende, D. T. Papanastasiou, N. Fontanals, C. Jiménez, D. Muñoz-Rojas, and D. Bellet, Low-cost fabrication of flexible transparent electrodes based on Al doped ZnO and silver nanowire nanocomposites: impact of the network density, *Nanoscale* **11**, 12097 (2019).
- [198] J. Resende, A. Sekkat, V. H. Nguyen, T. Chatin, C. Jiménez, M. Burriel, D. Bellet, and D. Muñoz-Rojas, Planar and transparent memristive devices based on titanium oxide coated silver nanowire networks with tunable switching voltage, *Small* **17**, 2007344 (2021).
- [199] L. Bardet, D. T. Papanastasiou, C. Crivello, M. Akbari, J. Resende, A. Sekkat, C. Sanchez-Velasquez, L. Rapenne, C. Jiménez, D. Muñoz-Rojas, A. Denneulin, and D. Bellet, Silver nanowire networks: Ways to enhance their physical properties and stability, *Nanomaterials* **11**, 2785 (2021).
- [200] S. Aghazadehchors, V. H. Nguyen, D. Muñoz-Rojas, C. Jiménez, L. Rapenne, N. D. Nguyen, and D. Bellet, Versatility of bilayer metal oxide coatings on silver nanowire networks for enhanced stability with minimal transparency loss, *Nanoscale* **11**, 19969 (2019).
- [201] C. Celle, A. Cabos, T. Fontecave, B. Laguitton, A. Benayad, L. Guettaz, N. Pélissier, V. H. Nguyen, D. Bellet, D. Muñoz-Rojas, and J.-P. Simonato, Oxidation of copper nanowire based transparent electrodes in ambient conditions and their stabilization by encapsulation: application to transparent film heaters, *Nanotechnology* **29**, 85701 (2018).
- [202] E. H. Linfield, K. Zeissler, O. Cespedes, N. Athanasopoulou, and A. Ghani, *Materials for the Energy Transition Roadmap: Materials for Low Loss Electronics* (Henry Royce Institute, Manchester, 2020). <https://www.royce.ac.uk/content/uploads/2020/09/M4ET-Low-Loss-Electronics-roadmap.pdf> (accessed January 16, 2025).
- [203] S. A. Chambers, Epitaxial growth and properties of thin film oxides, *Surf. Sci. Rep.* **39**, 105 (2000).
- [204] S. Yang, B. H. Lin, W.-R. Liu, J.-H. Lin, C.-S. Chang, C.-H. Hsu, and W. F. Hsieh, Structural characteristics and annealing effect of ZnO epitaxial films grown by atomic layer deposition, *Cryst. Growth Des.* **9**, 5184 (2009).
- [205] K. B. Klepper, O. Nilsen, and H. Fjellvåg, Epitaxial growth of cobalt oxide by atomic layer deposition, *J. Cryst. Growth* **307**, 457 (2007).
- [206] M. Coll, J. Gazquez, A. Palau, M. Varela, X. Obradors, and T. Puig, Low temperature epitaxial oxide ultrathin films and nanostructures by atomic layer deposition, *Chem. Mater.* **24**, 3732 (2012).
- [207] H. H. Sønsteby, E. Skaar, ØS Fjellvåg, J. E. Bratvold, H. Fjellvåg, and O. Nilsen, A foundation for complex oxide electronics -low temperature perovskite epitaxy, *Nat. Commun.* **11**, 2872 (2020).
- [208] Z. Sun, Z. Yuan, M. Xiao, S. M. Fairclough, A. Jan, G. Di Martino, C. Ducati, N. Strkalj, and J. L. MacManus-Driscoll, Low-temperature epitaxy of perovskite WO_3 thin films under atmospheric conditions, *Small Struct.* **5**, 2400089 (2024).
- [209] S. Ning, S. C. Huberman, Z. Ding, H.-H. Nahm, Y.-H. Kim, H.-S. Kim, G. Chen, and C. A. Ross, Anomalous defect dependence of thermal conductivity in epitaxial WO_3 thin films, *Adv. Mater.* **31**, 1903738 (2019).
- [210] X. Leng, J. Pereiro, J. Strle, A. T. Bollinger, and I. Božović, Epitaxial growth of high quality WO_3 thin films, *APL Mater.* **3**, 96102 (2015).
- [211] M. Coll, J. Fontcuberta, M. Althammer, M. Bibes, H. Boschker, A. Calleja, G. Cheng, M. Cuoco, R. Dittmann, B. Dkhil, *et al.*, Towards oxide electronics: A roadmap, *Appl. Surf. Sci.* **482**, 1 (2019).
- [212] N. Boysen, B. Misimi, A. Muriqi, J.-L. Wree, T. Hasselmann, D. Rogalla, T. Haeger, D. Theirich, M. Nolan, T. Riedl, and A. Devi, A carbene stabilized precursor for the spatial atomic layer deposition of copper thin films, *Chem. Commun.* **56**, 13752 (2020).
- [213] A. Sekkat, M. Weber, J. López-Sánchez, H. Rabat, D. Hong, J. Rubio-Zuazo, D. Bellet, G. Chichignoud, A. Kaminski-Cachopo, and D. Muñoz-Rojas, Selective spatial atomic layer deposition of Cu, Cu_2O , and CuO thin films in the open air: Reality or fiction? *Mater. Today Chem.* **29**, 101431 (2023).
- [214] T. Hasselmann, B. Misimi, N. Boysen, D. Zanders, J.-L. Wree, D. Rogalla, T. Haeger, F. Zimmermann, K. O. Brinkmann, S. Schädler, *et al.*, Silver thin-film electrodes grown by low-temperature plasma-enhanced spatial atomic layer deposition at atmospheric pressure, *Adv. Mater. Technol.* **8**, 2200796 (2023).
- [215] N. Boysen, T. Hasselmann, S. Karle, D. Rogalla, D. Theirich, M. Winter, T. Riedl, and A. Devi, An N-heterocyclic carbene based silver precursor for plasma enhanced spatial atomic layer deposition of silver thin films at atmospheric pressure, *Angew. Chem., Int. Ed.* **130**, 16458 (2018).
- [216] F. J. van den Bruele, M. Smets, A. Illiberi, Y. Creyghton, P. Buskens, F. Roozeboom, and P. Poodt, Atmospheric pressure plasma enhanced spatial ALD of silver, *J. Vac. Sci. Technol.*, **A 33**, 01A131 (2015).

- [217] A. Mameli, F. van den Bruele, C. K. Ande, M. A. Verheijen, W. M. M. Kessels, F. Roozeboom, and On the Growth, Percolation and wetting of silver thin films grown by atmospheric-plasma enhanced spatial atomic layer deposition, *ECS Trans.* **75**, 129 (2016).
- [218] J. R. van Ommen, D. Kooijman, M. de Niet, M. Talebi, and A. Goulas, Continuous production of nanostructured particles using spatial atomic layer deposition, *J. Vac. Sci. Technol., A* **33**, 021513 (2015).
- [219] V. Vandalon, A. Mackus, and W. Kessels, Surface chemistry during atomic layer deposition of Pt studied with vibrational sum-frequency generation, *J. Phys. Chem. C* **126**, 2463 (2022).
- [220] J. Shen, F. Roozeboom, and A. Mameli, Atmospheric-pressure plasma-enhanced spatial atomic layer deposition of silicon nitride at low temperature, *At. Layer Deposition* **1**, 1 (2023).
- [221] D. J. Higgs, J. W. DuMont, K. Sharma, and S. M. George, Spatial molecular layer deposition of polyamide thin films on flexible polymer substrates using a rotating cylinder reactor, *J. Vac. Sci. Technol., A* **36**, 01A117 (2018).
- [222] J. Pérez de la Cruz, E. Joanni, P. M. Vilarinho, and A. L. Khoklin, Thickness effect on the dielectric, ferroelectric, and piezoelectric properties of ferroelectric lead zirconate titanate thin films, *J. Appl. Phys.* **108**, 114106 (2010).
- [223] L. Kou, W. Guo, and C. Li, Piezoelectricity of ZnO and its nanostructures, in *2008 Symposium on Piezoelectricity, Acoustic Waves, and Device Applications* (IEEE, Nanjing, China, 2008), pp. 354–359.
- [224] T. Song, H. Tan, N. Dix, R. Moalla, J. Lyu, G. Saint-Girons, R. Bachelet, F. Sánchez, and I. Fina, Stabilization of the ferroelectric phase in epitaxial $\text{Hf}_{1-x}\text{Zr}_x\text{O}_2$ enabling coexistence of ferroelectric and enhanced piezoelectric properties, *ACS Appl. Electron. Mater.* **3**, 2106 (2021).
- [225] J. Wang, H. Guo, C.-Z. Zhu, Q. Cai, G.-F. Yang, and J.-J. Xue, ε - Ga_2O_3 : A promising candidate for high-electron-mobility transistors, *IEEE Electron Device Lett.* **41**, 1052 (2020).
- [226] Y. Kajikawa, Texture development of non-epitaxial polycrystalline ZnO films, *J. Cryst. Growth* **289**, 387 (2006).
- [227] S. Jeon, S. Bang, S. Lee, S. Kwon, W. Jeong, H. Jeon, H. J. Chang, and H.-H. Park, Structural and electrical properties of ZnO thin films deposited by atomic layer deposition at low temperatures, *J. Electrochem. Soc.* **155**, H738 (2008).
- [228] S. Battiato, A. Sekkat, C. S. Velasquez, A. L. Pellegrino, D. Bellet, A. Terrasi, S. Mirabella, and D. Muñoz-Rojas, Nanocomposites based on Cu_2O coated silver nanowire networks for high-performance oxygen evolution reaction, *Nanoscale Adv.* **6**, 4426 (2024).
- [229] Nanotechnology with the Potential for Global Impact, <https://www.spark-nano.com/articles/interview-hydrogen-standard/> (accessed December 12, 2024).
- [230] A. K. Jena, M. C. Sahu, K. U. Mohanan, S. K. Mallik, S. Sahoo, G. K. Pradhan, and S. Sahoo, Bipolar resistive switching in TiO_2 artificial synapse mimicking Pavlov's associative learning, *ACS Appl. Mater. Interfaces* **15**, 3574 (2023).
- [231] C.-L. Lin, C.-C. Tang, S.-C. Wu, S.-R. Yang, Y.-H. Lai, and S.-C. Wu, in *The 4th IEEE International NanoElectronics Conference* (2011), pp. 1–2.
- [232] Y. Li, P. Fang, X. Fan, and Y. Pei, NiO-based memristor with three resistive switching modes, *Semicond. Sci. Technol.* **35**, 055004 (2020).
- [233] J. Aziz, H. Kim, S. Rehman, K. D. Kadam, H. Patil, S. Aftab, M. F. Khan, and D. Kim, Discrete memristive levels and logic gate applications of Nb_2O_5 devices, *J. Alloys Compd.* **879**, 160385 (2021).
- [234] W.-C. Chien, M.-H. Lee, F.-M. Lee, Y.-Y. Lin, H.-L. Lung, K.-Y. Hsieh, and C.-Y. Lu, in *2011 International Electron Devices Meeting* (2011).
- [235] S. Rehman, J.-H. Hur, and D. Kim, Resistive switching in solution-processed copper oxide (Cu_xO) by stoichiometry tuning, *J. Phys. Chem. C* **122**, 11076 (2018).
- [236] P. Parreira, G. W. Paterson, S. McVittie, and D. A. MacLaren, Stability, bistability and instability of amorphous ZrO_2 resistive memory devices, *J. Phys. D: Appl. Phys.* **49**, 095111 (2016).
- [237] S. Brivio, S. Spiga, and D. Ielmini, HfO_2 -based resistive switching memory devices for neuromorphic computing, *Neuromorphic Comput. Eng.* **2**, 042001 (2022).
- [238] H. F. Liu, K. K. A. Antwi, Y. D. Wang, L. T. Ong, S. J. Chua, and D. Z. Chi, Atomic layer deposition of crystalline Bi_2O_3 thin films and their conversion into Bi_2S_3 by thermal vapor sulfurization, *RSC Adv.* **4**, 58724 (2014).
- [239] K. C. Kwon, J. H. Baek, K. Hong, S. Y. Kim, and H. W. Jang, Memristive devices based on two-dimensional transition metal chalcogenides for neuromorphic computing, *Nano-Micro Lett.* **14**, 58 (2022).
- [240] S. G. Sarwat, T. Moraitis, C. D. Wright, and H. Bhaskaran, Chalcogenide optomemristors for multi-factor neuromorphic computation, *Nat. Commun.* **13**, 2247 (2022).
- [241] M.-Y. Tsai, C.-T. Huang, C.-Y. Lin, M.-P. Lee, F.-S. Yang, M. Li, Y.-M. Chang, K. Watanabe, T. Taniguchi, C.-H. Ho, *et al.*, A reconfigurable transistor and memory based on a two-dimensional heterostructure and photoinduced trapping, *Nat. Electron.* **6**, 755 (2023).
- [242] J. Cai, X. Han, X. Wang, and X. Meng, Atomic layer deposition of two-dimensional layered materials: processes, growth mechanisms, and characteristics, *Matter* **2**, 587 (2020).
- [243] M. Weber, N. Boysen, O. Graniel, A. Sekkat, C. Dussarrat, P. Wiff, A. Devi, and D. Muñoz-Rojas, Assessing the environmental impact of atomic layer deposition (ALD) processes and pathways to lower it, *ACS Mater. Au* **3**, 274 (2023).
- [244] M. F. K. Niazi, D. Muñoz-Rojas, D. Evrard, and M. Weber, Comparative study of the environmental impact of depositing Al_2O_3 by atomic layer deposition and spatial atomic layer deposition, *ACS Sustainable Chem. Eng.* **11**, 15072 (2023).